

**Andreas Knoblach**

Robust Performance Analysis for  
Gust Loads Computation



# **Robust Performance Analysis for Gust Loads Computation**

Vom Promotionsausschuss der  
Technischen Universität Hamburg-Harburg  
zur Erlangung des akademischen Grades  
Doktor-Ingenieur (Dr.-Ing.)  
genehmigte Dissertation

von  
Andreas Joachim Knoblach

aus  
Augsburg

2015

Prüfungskomitee:

Prof. Dr. Herbert Werner

Dr. ir. Gertjan Looye

Prof. Dr.-Ing. Uwe Weltin (Vorsitzender)

Tag der mündlichen Prüfung: 14. Juli 2015

Copyright © 2015 Andreas Knoblach. All rights reserved. No part of this thesis may be reproduced or transmitted in any form or by any means, electronic or mechanical, including photocopying, recording or by any information storage retrieval system, without the written permission of the author.

# Acknowledgments

The present thesis is the result of my five years of research at the Institute for System Dynamics and Control of the German Aerospace Center (DLR) at Oberpfaffenhofen, Germany.

My thanks go to Prof. Dr. Herbert Werner – head of the Institute of Control Systems at the Hamburg University of Technology – for promoting my thesis. I thank him for our fruitful scientific discourse and for regular invitations to exciting Ph.D. workshops at his institute. I am also grateful to dr. ir. Gertjan Looye for co-examining my work and to Prof. Dr.-Ing. Uwe Weltin for assuming the head of my examining committee.

I am indebted to Dr.-Ing. Johann Bals – director of the Institute for System Dynamics and Control – and dr. ir. Gertjan Looye – head of the Department Aircraft Systems Dynamics – for their constant support and for giving me absolute freedom in my research. The initial impulse for my thesis came from dr. ir. Gertjan Looye and Thiemo Kier. I thank both for their valuable input on all questions about aeroelasticity and gust loads and for many inspiring discussions of my analysis results.

During the early stage of my research, Dr.-Ing. Florian Saupe and Dr.-Ing. Harald Pfifer provided invaluable support on all aspects of robust control theory. I am grateful to both for their help. One highlight of my research time was visiting the Aerospace Engineering and Mechanics Department at the University of Minnesota. I am thankful to Dr.-Ing. Johann Bals for making this possible and to Prof. Gary Balas for opening his doors to me. This visit gave me the opportunity to collaborate with Prof. Peter Seiler and with Dr.-Ing. Harald Pfifer. I want to thank them for everything they taught me about integral quadratic constraints. I am also indebted to my colleagues (in alphabetical order) Mehran Assanimoghaddam, Andreas Klöckner, Manuel Pusch, and Julian Theis for their precise reviews of my thesis and their constructive feedback, which greatly helped to improve my work. I also want to acknowledge all of my DLR colleagues for the great working atmosphere and the lot of fun we had not only during work but also in our common free time.

Finally, I am thankful to my family; especially to my parents for their unconditional support in everything I do.

Munich, July 2015

Andreas Knoblach



# Abstract

In the design process of modern aircraft, a comprehensive analysis regarding flutter stability and structural loads is imperative. Numerous points in the flight envelope, different aircraft and loading configurations as well as many types of maneuvers and external disturbances have to be considered. This leads quickly to millions of simulation cases. Consequently, the analysis is complex and time consuming. To solve this problem, the present thesis proposes a new approach based on the robust performance analysis framework.

Parameter dependences and uncertainties of gust loads models are naturally captured by linear parameter varying (LPV) and uncertain linear time invariant (LTI) models. The performance of these models is then evaluated using the worst case energy-to-peak gain. This performance metric is chosen because the maximum peaks of the model outputs are most important in gust loads analysis. Assuming that the gusts can be described by unit energy, this metric represents hence a bound for maximum gust loads.

For the considered model types, an upper bound of the worst case energy-to-peak gain can be computed by solving a convex optimization problem with infinite dimensional linear matrix inequality constraints. Three techniques for dealing with such constraints are reviewed and assessed in a benchmark. Further, the inclusion of nonlinearities in the analysis by integral quadratic constraints (IQCs) is treated. The focus is put on the analysis of saturated LPV systems by local IQCs.

According to the certification specifications for large aeroplanes, a set of “one-minus-cosine” gusts must be considered for determining maximum gust loads. In order to use the worst case energy-to-peak gain for doing this, a weighting filter is designed s.t. all relevant gusts can be created with unit energy. Consequently, the norm of the weighted gust loads model represents a guaranteed upper bound for “one-minus-cosine” gust loads. In a comprehensive case study using models of industrial complexity, LTI norm bounds are compared with conventional simulation results. This study shows that the norm bound is not overly conservative and that it serves as an excellent indicator for critical flight conditions. Based on these results, the analysis is extended to LPV and uncertain gust loads models. Finally, the design and the worst case analysis of a saturated gust load alleviation system are presented.

All results show the effectiveness of this new approach, which allows to efficiently identify critical flight points without the risk of missing a critical parameter combination. Due to computational efficiency this approach is especially convenient for multidisciplinary design optimizations.



# Contents

<b>Acknowledgments</b>	<b>iii</b>
<b>Abstract</b>	<b>v</b>
<b>List of Abbreviations</b>	<b>xi</b>
<b>List of Symbols</b>	<b>xiii</b>
<b>1 Introduction</b>	<b>1</b>
1.1 Motivation . . . . .	2
1.2 Contributions . . . . .	4
1.3 Outline . . . . .	5
<b>2 Gust Loads Analysis of Flexible Aircraft</b>	<b>7</b>
2.1 Aeroelastic Models for Gust Loads . . . . .	7
2.1.1 Structural Dynamic Model . . . . .	8
2.1.2 Aerodynamic Model . . . . .	10
2.1.3 Model Integration in the Frequency Domain . . . . .	14
2.1.4 Model Integration in the Time Domain . . . . .	14
2.2 Computation of Maximum Gust Loads . . . . .	17
2.2.1 The “One-Minus-Cosine” Gust Scenario . . . . .	17
2.2.2 Number of Load Cases . . . . .	20
2.2.3 Covering the Flight Envelope . . . . .	21
2.2.4 Techniques for an Efficient Estimation of Maximum Gust Loads . . . . .	23
<b>3 Robust Performance Analysis</b>	<b>25</b>
3.1 Preliminaries . . . . .	25
3.1.1 Signal Norms . . . . .	25
3.1.2 LTI Systems . . . . .	26
3.1.3 Semidefinite Programs and Linear Matrix Inequalities . . . . .	26
3.2 Parametric Uncertain and LPV Models . . . . .	27
3.2.1 Linear Parameter Varying Models . . . . .	28
3.2.2 Linear Fractional Representation of LPV Models . . . . .	28
3.3 Analysis of LTI and LPV Systems . . . . .	30
3.3.1 Stability . . . . .	30

3.3.2	Worst Case Energy-to-Energy Gain . . . . .	32
3.3.3	Worst Case Energy-to-Peak Gain . . . . .	32
3.4	Techniques for Dealing with Infinite Dimensional LMIs . . . . .	38
3.4.1	Construction of Lyapunov Matrix Functions . . . . .	38
3.4.2	Approximation Based on Gridding the Parameter Space . . . . .	39
3.4.3	Relaxation Based on Multi Convexity . . . . .	41
3.4.4	Relaxation Based on the Full Block S-Procedure . . . . .	42
3.5	A Benchmark of Techniques for Infinite Dimensional LMIs . . . . .	46
3.5.1	Model of the Aeroelastic System . . . . .	46
3.5.2	Numerical and Implementational Aspects . . . . .	48
3.5.3	Assessment of the Multi Convexity Approach . . . . .	48
3.5.4	Assessment of Multipliers for the Full Block S-Procedure . . . . .	49
3.5.5	Assessment of the Gridding Approach . . . . .	51
3.5.6	Assessment of Different Lyapunov Basis Functions . . . . .	53
3.5.7	Conclusions . . . . .	54
<b>4</b>	<b>Analysis of Uncertain LPV Systems using IQCs</b>	<b>55</b>
4.1	Integral Quadratic Constraints . . . . .	55
4.1.1	Definition and Properties . . . . .	55
4.1.2	IQCs for Saturation . . . . .	58
4.2	Analysis of Uncertain LPV Systems . . . . .	60
4.2.1	Uncertain LPV System . . . . .	60
4.2.2	Worst Case Energy-to-Energy Gain . . . . .	61
4.2.3	Worst Case Energy-to-Peak Gain . . . . .	62
4.2.4	Analysis of Saturated Systems using Local IQCs . . . . .	65
4.3	Analysis of an Aeroelastic System . . . . .	67
4.3.1	Aeroservoelastic System . . . . .	67
4.3.2	Comparison of IQCs . . . . .	70
4.3.3	Convergence of Local IQCs . . . . .	71
4.3.4	Influence of the Parameter Rate Bounds . . . . .	73
4.3.5	Conclusions . . . . .	73
<b>5</b>	<b>LTI Performance Analysis for Gust Loads Computation</b>	<b>75</b>
5.1	Weighting Filter . . . . .	75
5.1.1	Design of the Weighting Filter . . . . .	76
5.1.2	Evaluation of the Weighting Filter . . . . .	78
5.2	Determination of Worst Case Gust Loads . . . . .	80
5.2.1	Implementational Aspects . . . . .	81
5.2.2	Analysis of the Wing Loads . . . . .	81
5.2.3	Worst Case Gusts for the Wing Loads . . . . .	85
5.2.4	Inclusion of Trim Loads . . . . .	86
5.2.5	Analysis of the Tail Loads . . . . .	88
5.3	Determination of Lower Bounds for Maximum Peak Loads . . . . .	90

5.4	Evaluation and Conclusions . . . . .	92
<b>6</b>	<b>Robust Analysis and Control of Gust Loads Models</b>	<b>95</b>
6.1	LPV Analysis regarding the Flight Envelope . . . . .	95
6.1.1	LPV Model Order Reduction . . . . .	96
6.1.2	LPV Analysis – Results and Conclusions . . . . .	99
6.2	Influence of the Damping Ratio . . . . .	101
6.3	Design of a Gust Load Alleviation System . . . . .	104
6.3.1	Scenario and Aircraft Model . . . . .	104
6.3.2	Controller Structure and Tuning . . . . .	105
6.3.3	Results and Conclusions . . . . .	109
6.4	Analysis of a Saturated Gust Load Alleviation System . . . . .	110
<b>7</b>	<b>Summary and Outlook</b>	<b>113</b>
7.1	Summary . . . . .	113
7.2	Outlook . . . . .	114
<b>A</b>	<b>Convex Optimization</b>	<b>115</b>
A.1	Convex Sets and Functions . . . . .	115
A.2	Bounds for Convex Functions with Polytopic Parameter Spaces . .	116
A.3	Schur Complement . . . . .	117
<b>B</b>	<b>State Space Matrices of Aeroelastic System for the Benchmarks</b>	<b>119</b>
B.1	State Space Matrices for the Benchmark in Section 3.5 . . . . .	119
B.2	State Space Matrices for the IQC Example in Section 4.3 . . . . .	119
	<b>Bibliography</b>	<b>121</b>
	<b>Index</b>	<b>127</b>
	<b>List of Publications</b>	<b>129</b>
	<b>Curriculum Vitae</b>	<b>131</b>



# List of Abbreviations

Abbreviation	Description	Page
AIC	Aerodynamic influence coefficient	11
CFD	Computational fluid dynamics	
DLM	Doublet lattice method	11
DOF	Degree of freedom	
EASA	European Aviation Safety Agency	
EFCS	Electronic flight control system	7
EOM	Equations of motion	8
FE	Finite element	8
FFT	Fast Fourier transform	
FRF	Frequency response function	26
HTP	Horizontal tail plane	
IQC	Integral quadratic constraint	56
LFR	Linear fractional representation	29
LFT	Linear fractional transformation	29
LiDAR	Light detection and ranging	
LMI	Linear matrix inequality	27
LPV	Linear parameter varying	28
LTl	Linear time invariant	26
RFA	Rational function approximation	14
RMS	Root mean square	
SDP	Semidefinite program	27
SISO	Single-input single-output	
SVD	Singular value decomposition	
VLM	Vortex lattice method	10
VTP	Vertical tail plane	



# List of Symbols

## Fundamental Notation

Symbol	Description	Page
$a$	Scalar	
$\mathbf{a}$	Vector	
$\mathbf{A}$	Matrix	
$\bar{a}$	Complex conjugate of $a$	
$\mathbf{A}^T$	Transposed of $\mathbf{A}$	
$\mathbf{A}^*$	Complex conjugate transposed of $\mathbf{A}$	
$\mathbf{A}^{-1}$	Inverse of $\mathbf{A}$	
$\mathbf{I}$	Identity matrix	
$\mathbf{I}_n$	Identity matrix of size $n \times n$	
$\mathbf{0}$	Zero matrix	
$e$	Euler's number	
$j$	Imaginary unit	

## Vector and Function Spaces

Symbol	Description	Page
$\mathcal{A}$	Space of admissible parameter trajectories	28
$\mathbb{C}$	Set of complex numbers	
$\mathbb{C}^{n \times m}$	Set of $n \times m$ matrices with elements in $\mathbb{C}$	
$\mathbb{H}^n$	Set of Hermitian matrices in $\mathbb{C}^{n \times n}$	
$\mathcal{L}_2$	Space of Lebesgue integrable vector functions	25
$\mathcal{L}_{2e}$	Extended $\mathcal{L}_2$ space	26
$\mathcal{L}_\infty$	Space of bounded vector functions	26
$\mathcal{P}$	Parameter space	28
$\mathbb{R}$	Set of real numbers	
$\mathbb{R}_+$	Set of nonnegative real numbers	
$\mathbb{R}^{n \times m}$	Set of $n \times m$ matrices with elements in $\mathbb{R}$	
$\mathbb{S}^n$	Set of symmetric matrices in $\mathbb{R}^{n \times n}$	

**Control Theory**

Symbol	Description	Page
$A$	State matrix	26
$B$	Input matrix	26
$C$	Output matrix	26
$D$	Feed-through matrix	26
$d$	Disturbance input vector	26
$e$	Performance output vector	26
$v$	Input vector of $\Delta$	29
$w$	Output vector of $\Delta$	29
$x$	State vector	26
$z$	Output vector s.t. to an IQC	56
$P$	Plant	
$P_{d \rightarrow e}$	Path from $d$ to $e$ of $P$	
$P_\rho$	LPV plant	28
$\rho$	Parameter vector	28
$\Delta$	Uncertain or nonlinear operator	29
$\mathcal{F}_u(M, \Delta)$	Upper LFT	29
$V$	Lyapunov function	31
$W_c$	Controllability Gramian matrix	34
$W$	Weighting filter	
$X(p)$	Parameter dependent Lyapunov matrix	31
$\partial X(p, q)$	Derivative of Lyapunov matrix	31
$s$	Laplace variable	
$\omega$	Frequency	
$\Pi$	Multiplier for the Full Block S-Procedure	43
$\Pi$	Multiplier of an IQC in the frequency domain	56
$(\Psi, M)$	Multiplier of an IQC in the time domain	56

**Operators and Shortforms**

Symbol	Description	Page
$\text{conv}(\cdot)$	Convex hull of its argument	115
$\text{diag}(\cdot)$	Block diagonal concatenation of its arguments or diagonal entries of one argument	30, 34
$\text{eig}(\cdot)$	Eigen values of its argument	
$\text{Im}(\cdot)$	Imaginary part of its argument	
$\text{ker}(\cdot)$	Kernel (or null space) of its argument	
$\text{Re}(\cdot)$	Real part of its argument	

Symbol	Description	Page
$\text{sat}(\cdot)$	Saturation nonlinearity	58
$\text{sgn}(\cdot)$	Sign of its argument	
$\text{trace}(\cdot)$	Trace of its argument	
$\text{vert}(\cdot)$	Vertices of the convex hull of its argument	115
$ \cdot $	Absolute value	
$\ \cdot\ $	Norm	
$\ \cdot\ _p$	$p$ vector norm	
$\ \cdot\ _{\mathcal{L}_2}$	$\mathcal{L}_2$ signal norm	25
$\ \cdot\ _{\mathcal{L}_\infty}$	$\mathcal{L}_\infty$ signal norm	26
$\ \cdot\ _{\mathcal{L}_2 \rightarrow \mathcal{L}_2}$	Induced $\mathcal{L}_2 \rightarrow \mathcal{L}_2$ system norm	32, 61
$\ \cdot\ _{\mathcal{L}_2 \rightarrow \mathcal{L}_\infty}$	Induced $\mathcal{L}_2 \rightarrow \mathcal{L}_\infty$ system norm	32, 63

## Aeroelasticity

Symbol	Description	Page
$_{gg}M, {}_{hh}M$	Structural/modal mass matrix	8
$_{gg}K, {}_{hh}K$	Structural/modal stiffness matrix	8
$_{hh}B$	Modal damping matrix	9
$_{gh}\Phi$	Modal matrix	9
$_{g}u, {}_{h}u$	Structural/modal displacements	8
$_{g}P, {}_{h}P$	Structural/modal loads	8
${}_cP$	Cut loads	10
${}_cP_{\text{sh}}$	Cut shear forces (in N)	18
${}_cP_{\text{tor}}$	Cut torsional moment (in N m)	18
${}_cP_{\text{ben}}$	Cut bending moment (in N m)	18
${}_jw$	Downwash at collocation points	10
$\Delta_j p$	Pressure coefficient	11
$_{jj}Q$	AIC matrix	11, 13
${}_x u$	Control surface deflections	13
${}_G w$	Normalized gust velocity	13, 18
$H$	Gust length (in m)	18
$h$	Altitude (in m)	
$Ma$	Mach number	11
$p_\infty$	Dynamic pressure (in N/m <sup>2</sup> )	11
$\rho$	Air density (in kg/m <sup>3</sup> )	
$U_\infty$	True flight speed (in m/s)	
$\bar{\omega}$	Reduced frequency	12



# 1 Introduction

Recent developments in the aircraft industry are primarily driven by the need for fuel reduction in order to stay competitive. The enormous progress in doing this is illustrated in Figure 1.1 for different aircraft categories (IEA 2009). For example, the latest Airbus aircraft – the Airbus A350-900 (see Figure 1.2) – is promoted to achieve a 25 % reduction in fuel consumption compared to predecessors. Another example is the renewal of the Airbus A320. Its fuel consumption is now reduced by 20 % with respect to the original version. A similar situation can be found at Airbus' main rival Boeing. The reasons for this development are an intensified price competition, the increasing kerosene costs, and stricter environmental protection regulations.

As stated in IEA 2009, this reduction of fuel consumption was achieved by three major aspects. First, big progress in propulsion technology resulted in more efficient engines featured by a higher bypass ratio. Second, latest computational fluid dynamics (CFD) algorithms allow an optimization of the aircraft's aerodynamics which results in drag reduction. Third, the usage of lightweight construction, new

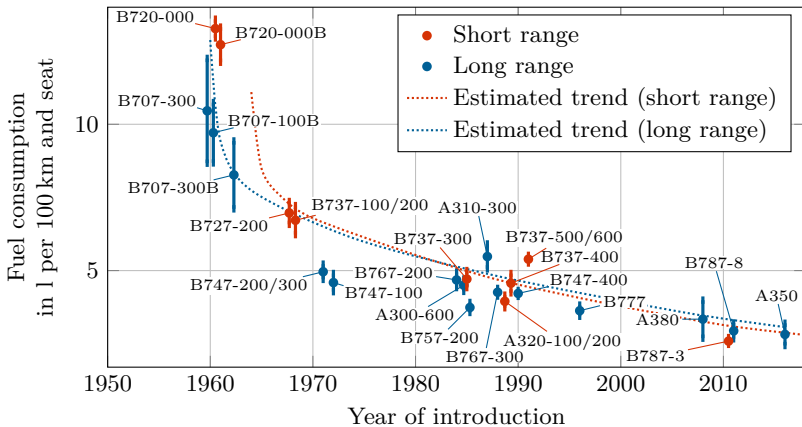


**Figure 1.1:** Evolution of fuel consumption for different aircraft categories. The error bar for each aircraft reflects varying configurations. (Figure adapted from IEA 2009.)



**Figure 1.2:** Airbus A350.<sup>1</sup>

materials, and computer aided optimization of the aircraft structure lead to a reduction of the aircraft weight. While the aerodynamic optimization leads to wings with high spans and high aspect ratios, the structural optimization results in more flexible wings than in conventional designs. This means that latest aircraft feature long and flexible wings which lead to an increased interaction of aerodynamics, structural dynamics and flight dynamics. This interaction can result in higher structural loads or even cause flutter. Consequently, the structural design plays a key role towards more economical aircraft and a compromise between weight reduction and safety must be found. For finding this compromise, the careful identification of worst case gust loads is imperative.

## 1.1 Motivation

During the operation of an aircraft, various loads act on the aircraft which must be borne by its structure. These loads are caused by maneuvers and external disturbances. Especially for large and flexible aircraft, external disturbances in terms of gusts and turbulence play an important role in sizing the structure. The challenge in the analysis of these gust loads lies in the feedback interconnection of the aerodynamic and structural model. Since the aerodynamic flow changes rapidly during gust encounters, complex models for the unsteady aerodynamics must be considered. This leads to models with several thousand states and outputs. The required analysis can be even more complicated if an electronic flight control system (EFCS) is part of the loop.

<sup>1</sup>Figure 1.2 is taken from <http://www.airbus.com/galleries/photo-gallery/dg/idp/48675-a350-xwb-route-proving-front-shot> (on July 20, 2015) with permission of Airbus S.A.S. and BOCKFILM GmbH (© S. Pam).

In order to ensure the safe operation of an aircraft, the certification authorities state precise regulations how this aeroelastic analysis has to be performed (EASA CS-25; FAA FAR-25). In principle, three aspects have to be considered. During the flutter analysis, the stability of the aeroelastic interconnection is examined. Next, the expected maximum loads acting on the structure during maneuvers are computed. Finally, the response of the aircraft on turbulence and gusts are examined. The regulations require the consideration of two types of excitation: “one-minus-cosine” gusts and continuous turbulence. In the first case, an aircraft model is excited with a discrete “one-minus-cosine” gust profile and the model outputs, e.g., the wing root bending moment or the vertical acceleration, are computed. Next, the trim loads are superimposed and the procedure is repeated for several gust lengths. Moreover, the complete process has to be performed for lots of flight points such that the entire design envelope (defined by velocity, altitude, loading etc.) is covered. Finally, the maximum and minimum peak of every output for all these simulations define the limit loads due to discrete gusts. The other type of excitation – namely continuous turbulence – considers the stochastic nature of turbulence. Here, the von Kármán wind turbulence model describes the aircraft excitation and the results are evaluated by stochastic means. The limit loads are derived from the root mean square (RMS) value of the model response.

Because of the huge parameter space representing the aircraft envelope and many uncertainties, millions of cases have to be considered during the flutter and loads analysis. The conventional analysis is hence extremely time consuming. Consequently, it is unattractive during the aircraft pre-design and optimization stage. To reduce the numerical burden during a multidisciplinary design optimization, it is common practice to consider only an agreed set of worst case conditions. However, especially in combination with an EFCS, this set might not contain the actual worst case. Consequently, there is a need for robust and reliable algorithms for the identification of these scenarios.

Since the early eighties, a mathematical framework has been developed for the analysis of uncertain systems. This framework includes the structured singular value analysis ( $\mu$  analysis) which allows the robust stability analysis of systems with structured uncertainties. Because the parameter dependences and uncertainties of aeroelastic models are naturally captured by this model type, the  $\mu$  analysis allows to efficiently compute guaranteed worst case flutter bounds (Lind and Brenner, 1999; Borglund, 2004). The robust analysis framework has hence proved useful for flutter analysis.

Another methodology of this framework is the robust performance analysis. This method evaluates the performance of linear parameter varying (LPV) and uncertain linear time invariant (LTI) systems by input-output norms which can be efficiently computed. The most common norm is the worst case energy-to-energy gain (also known as  $\mathcal{H}_\infty$  norm). However, for gust loads analysis the worst case energy-to-peak gain is more promising. The reason is that this metric represents

a guaranteed bound on the peaks of the model outputs due to any disturbance with unit energy. Assuming that the gusts can be described by unit energy, the worst case energy-to-peak gain represents hence a guaranteed upper bound for the maximum peak loads which is the most interesting quantity in gust loads analysis. It is further possible to include nonlinearities such as saturation into the analysis by latest results within the integral quadratic constraint (IQC) framework. Consequently, the robust performance analysis framework has great potential to improve the gust loads analysis process.

## 1.2 Contributions

The main goal of this thesis is to investigate to which extent the robust performance analysis framework can be used for gust loads analysis. This requires a careful review of existing robust performance analysis methods. Because most of the existing methods focus on the worst case energy-to-energy gain, it is necessary to adapt existing methods for the worst case energy-to-peak gain. After elaborating the required theory, the gust loads analysis problem has to be expressed in a way which is suitable for robust performance analysis. In this thesis, the following notable contributions are made in order to achieve the aims of this work.

- To compute worst case gains, a convex optimization problem with infinite dimensional linear matrix inequality (LMI) constraints has to be solved. Several methods to tackle these constraints are described in the literature but there is a lack of a neutral comparison of them. To fill this gap, three methods are reviewed and assessed in a benchmark. This contribution is partially published in [Knobloch et al. \(2013\)](#).
- An iterative procedure for the low conservative, worst case analysis of saturated LPV systems is proposed. The procedure is based on the analysis of uncertain LPV systems using IQCs ([Pfifer and Seiler, 2014a](#)) and on the notion of local IQCs ([Summers and Packard, 2010](#)). However, both works focus on the worst case energy-to-energy gain while this thesis treats the energy-to-peak gain. The effectiveness of the proposed procedure is demonstrated using a simple aeroservoelastic system. Preliminary results on this contribution are recently published in [Knobloch, Pfifer, and Seiler \(2015\)](#).
- The most important contribution of this thesis is the improvement, in terms of efficiency and reliability, of the gust loads analysis process by means of the robust performance analysis framework. It is shown that the worst case energy-to-peak gain allows for computing not overly conservative but guaranteed upper bounds for “one-minus-cosine” gust loads. This worst case analysis can be extreme efficiently performed and lasts less than 6 % of the time for alternatively required simulations. Additionally, worst case

gusts are computed and physically interpreted. In [Knobloch \(2013b\)](#) and [Knobloch \(2013a\)](#), preliminary, comparable results using a simpler model with only two outputs are published.

Based on the worst case analysis results, critical flight points are identified next. Simulation results for these flight points are then used for computing lower bounds for the worst case loads.

- The effectiveness and versatile possibilities of the developed analysis process are demonstrated at several examples:
  - The considered gust loads models are naturally represented by LPV models w.r.t. the flight envelope. An LPV performance analysis allows hence to compute guaranteed bounds for gust loads by only one analysis. Additionally, this analysis covers the transitions from one flight point to another.
  - The proposed process allows to consider uncertainties in the analysis. As an example, the damping ratio – one of the most uncertain parameters in gust loads models – is considered. The analysis result allows to identify critical parameter combinations without the risk of missing a critical parameter value.
  - The proposed analysis method can be effectively used for multidisciplinary design optimizations. The effectiveness is demonstrated by tuning a gust load alleviation system.
  - Gust load alleviation systems are subject to saturation and sensor uncertainties. The above mentioned IQC based analysis procedure for saturated LPV systems can be used to examine the effects of these perturbations. This worst case analysis is used to prove robust stability and performance of the previously designed gust load alleviation system.

## 1.3 Outline

The structure of this thesis is illustrated in [Figure 1.3](#).

In [Chapter 2](#), the basics of aeroelastic modeling and gust loads analysis are established. The fundamental concepts of the structural dynamic and aerodynamic model are presented and their feedback interconnection is explained. Afterwards, the precise regulations for the gust loads analysis are discussed.

[Chapter 3](#) introduces the theoretical fundamentals of robust performance analysis. First, LPV models and their linear fractional representations (LFRs) are introduced. Afterwards, the performance analysis of this system class is discussed where the emphasis is put on the worst case energy-to-peak gain. The analysis algorithm requires to solve a semidefinite program (SDP) with infinite dimensional LMI

constraints. Three techniques to deal with such constraints are reviewed and assessed in a benchmark at the example of a two degrees-of-freedom (DOF) aeroelastic system.

Including nonlinearities into the performance analysis using IQCs is treated in [Chapter 4](#). The focus lies on the analysis of saturated LPV systems. Next to a description of saturation with standard time and frequency domain IQCs, an iterative procedure using local IQCs is proposed. The benefits of this procedure are demonstrated at the example of a simple aeroelastic system combined with a saturated gust load alleviation system.

In [Chapter 5](#), the connection between the energy-to-peak gain and “one-minus-cosine” gust loads is elaborated using an aircraft model of industrial complexity. First, a weighting filter to represent the required gusts with unit energy is designed and optimized. Afterwards, upper bounds for the gust peak loads are computed using the energy-to-peak gain. These results are compared to conventional simulation results and worst case excitations are determined. Based on the performance analysis results, critical flight points are identified which are then used to determine lower bounds for the peak loads.

The versatile possibilities of the robust performance analysis framework for gust loads computation are finally demonstrated in [Chapter 6](#). First, an LPV analysis w.r.t. the entire flight envelope and the analysis of a model with modal uncertainties is presented. Afterwards, it is shown how the energy-to-peak gain can be used to optimize a gust load alleviation controller. Robust stability and performance of this controller w.r.t. saturation and sensor uncertainties is finally proved using IQCs.

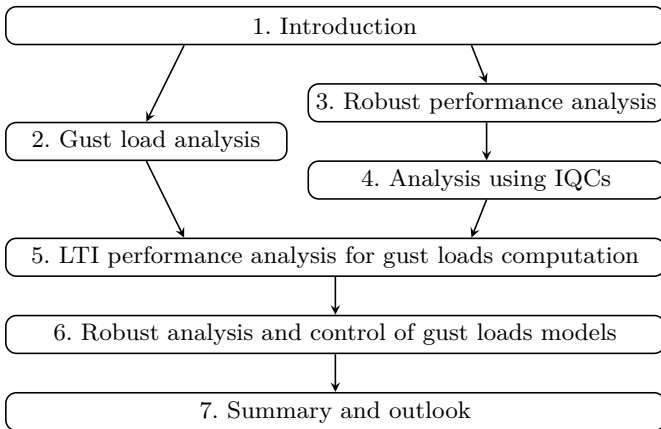


**Figure 1.3:** Structure of this thesis.

## 2 Gust Loads Analysis of Flexible Aircraft

The background of gust loads analysis is presented in this chapter. In [Section 2.1](#), the aeroelastic model used in this thesis is introduced. Its structural dynamic and aerodynamic model are explained first. Afterwards, their feedback interconnection in the frequency domain and in the time domain is treated. Following this, the gust loads analysis procedure is described in [Section 2.2](#). The focus is put on the determination of maximum “one-minus-cosine” gust loads.

### 2.1 Aeroelastic Models for Gust Loads

An aeroelastic system is characterized by the feedback interconnection of the aerodynamics and the structural dynamics (cf. [Figure 2.1](#)). The equations of motion (EOM) are driven by the aerodynamic forces whereas the structural deformation alters the aerodynamic flow. If additionally an electronic flight control system (EFCS) is part of the loop, it is called an aeroservoelastic system. There are three major issues in aeroservoelasticity:

**Flutter:** Is the aeroservoelastic system stable?

**Maneuver loads:** What are the maximum structural loads due to maneuvers?

**Gust loads:** What are the maximum structural loads due to gusts and turbulence?

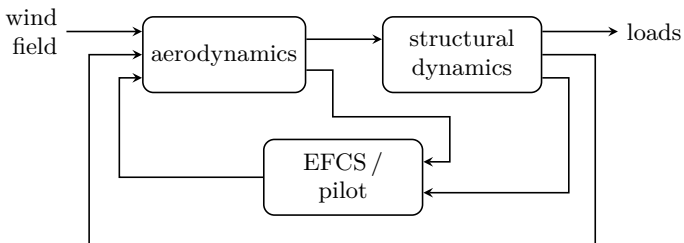


**Figure 2.1:** Basic aeroservoelastic interconnection: Feedback interconnection of the structural dynamics, the aerodynamics, and the EFCS/pilot.

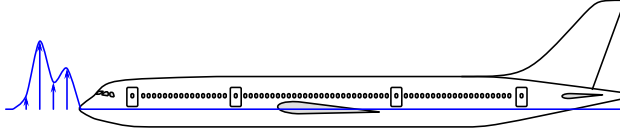


**Figure 2.2:** Gust encounter of an aircraft.

During the certification process of a new aircraft, all three points have to be considered. To that end, the European Aviation Safety Agency (EASA) states precise requirements and acceptable means for compliance (EASA CS-25)<sup>1</sup>. As already mentioned in the introduction, this thesis deals with gust loads.

The modeling process described in this thesis reflects the requirements for the certification of new aircraft based on EASA CS-25. Consequently, the same model types are also used in the industry. Following the certification regulations, the wind field is assumed to be one-dimensional and the gust velocity is acting either vertically or laterally to the flight direction. Hence, the gust acts first at the aircraft nose and last at the aircraft tail as illustrated in Figure 2.2. An overview of gust loads models is presented below. For details, it is referred to the common literature e.g., Bisplinghoff, Ashley, and Halfman (1955), Hoblit (1988), Rodden and Johnson (2004) and Kier (2011). The modeling is demonstrated using the Digital-X project model (Kroll and Rossow, 2012), which serves as an example in this thesis.

### 2.1.1 Structural Dynamic Model

The structural dynamics of an aircraft are described by a finite element (FE) model. This means that the continuum of the structure is discretized into finite elements. The nodes of the FE model are placed along the loads reference axis of the fuselage, the wing, the horizontal tail plane (HTP) and the vertical tail plane (VTP), see Figure 2.3. Every node has up to three translational and three rotational DOF.<sup>2</sup> The resulting DOF are referred to as  $g$ -set and are collected in the vector  ${}_g\mathbf{u}$ . A typical size of the  $g$ -set is 1500 DOF. Finally, the FE model leads to the following frequency domain equations of motion (EOM):

$$-\omega^2 {}_{gg}\mathbf{M} {}_g\mathbf{u} + {}_{gg}\mathbf{K} {}_g\mathbf{u} = {}_g\mathbf{P}_{\text{ext}}. \quad (2.1)$$

In (2.1),  ${}_{gg}\mathbf{M}$  is the mass matrix and  ${}_{gg}\mathbf{K}$  the stiffness matrix. The external nodal forces are denoted  ${}_g\mathbf{P}_{\text{ext}}$  and  $\omega$  is the frequency. See Rodden and Johnson (2004) for details.

<sup>1</sup>The EASA CS-25 is identical to the US counterpart FAA FAR-25.

<sup>2</sup>This FE model can be obtained by applying a Guyan reduction on a more complex FE model, which includes the complete aircraft structure (see Guyan, 1965). Alternatively, a model using beam elements can be directly defined.

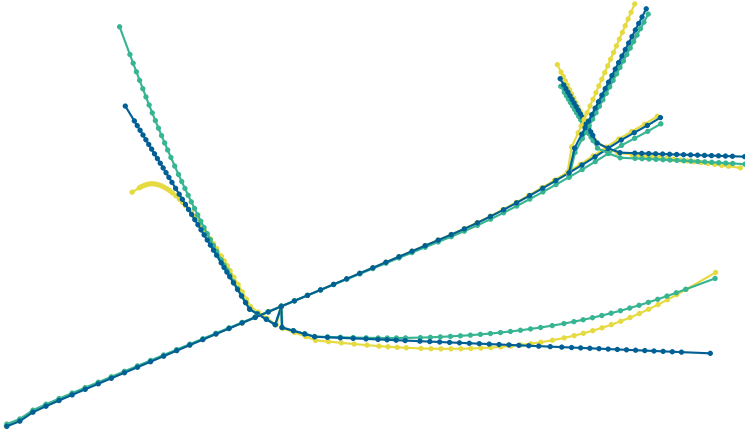


**Figure 2.3:** Structural dynamic model: FE model along the loads reference axis. The undeformed grid ( $\text{---}\bullet\text{---}$ ) and the first two eigenmodes ( $\text{---}\bullet\text{---}$ ) and ( $\text{---}\bullet\text{---}$ ) are depicted.

In order to reduce the problem size, a modal analysis is performed next. To that end, the eigenvalue problem

$${}_{gg}\mathbf{K}\boldsymbol{\Phi} = \omega^2 {}_{gg}\mathbf{M}\boldsymbol{\Phi} \quad (2.2)$$

is solved. The low frequency mode shapes (typically 50 to 100) are collected in the modal matrix  ${}_{gh}\boldsymbol{\Phi}$  which allows to define the modal (or generalized) DOF ( $h$ -set)

$${}_g\mathbf{u} \approx {}_{gh}\boldsymbol{\Phi} {}_h\mathbf{u} . \quad (2.3)$$

The generalized EOM are given as

$$-\omega^2 \underbrace{{}_{gh}\boldsymbol{\Phi}^T {}_{gg}\mathbf{M} {}_{gh}\boldsymbol{\Phi}}_{= {}_{hh}\mathbf{M}} {}_h\mathbf{u} + j\omega {}_{hh}\mathbf{B} {}_h\mathbf{u} + \underbrace{{}_{gh}\boldsymbol{\Phi}^T {}_{gg}\mathbf{K} {}_{gh}\boldsymbol{\Phi}}_{= {}_{hh}\mathbf{K}} {}_h\mathbf{u} = {}_{gh}\boldsymbol{\Phi}^T {}_g\mathbf{P}_{\text{ext}} \quad (2.4)$$

or equivalently in the time domain as

$${}_{hh}\mathbf{M} {}_h\ddot{\mathbf{u}} + {}_{hh}\mathbf{B} {}_h\dot{\mathbf{u}} + {}_{hh}\mathbf{K} {}_h\mathbf{u} = {}_{gh}\boldsymbol{\Phi}^T {}_g\mathbf{P}_{\text{ext}} . \quad (2.5)$$

The diagonal matrices  ${}_{hh}\mathbf{K}$  and  ${}_{hh}\mathbf{M}$  are referred to as modal stiffness and modal mass matrix respectively. A modal damping matrix  ${}_{hh}\mathbf{B}$  is already added to the EOM. Modal damping means that every eigenmode is damped individually. The damping matrix is hence also a diagonal matrix whose elements are defined as

$${}_{hh}\mathbf{B}_{ii} = \zeta_i \omega_i = \zeta_i \sqrt{{}_{hh}\mathbf{K}_{ii} / {}_{hh}\mathbf{M}_{ii}} \quad (2.6)$$

where  $\zeta_i$  and  $\omega_i$  are the damping ratio and eigenfrequency of the  $i^{\text{th}}$  mode. Here, the notation  $_{hh}\mathbf{B}_{ii}$  means the  $i^{\text{th}}$  diagonal entry of the damping matrix. See [Rodden and Johnson \(2004\)](#) for details. It should be noted that the modal matrix  $_{gh}\Phi$  can be partitioned into rigid body and flexible modes. This allows to replace the linear rigid body EOM by its nonlinear counterpart (see [Waszak and Schmidt, 1988](#); [Kier, 2011](#)).

The nodal loads are recovered using the force summation method:

$$_g\mathbf{P} = _g\mathbf{P}_{\text{ext}} - _g\mathbf{P}_{\text{iner}}, \quad (2.7)$$

where the inertial forces are computes as

$$_g\mathbf{P}_{\text{iner}} = -\omega^2_{gg}\mathbf{M}_{gh}\Phi_h\mathbf{u}. \quad (2.8)$$

However, for the structural design, the shear forces, the torsional moment, and the bending moments are required. These loads are also referred to as cut loads ( $c$ -set) and denoted as  $_c\mathbf{P}$ . They can be computed by a simple matrix multiplication

$$_c\mathbf{P} = _{cg}\mathbf{T}_g\mathbf{P}. \quad (2.9)$$

In principle,  $_{cg}\mathbf{T}$  sums up the forces and applies the lever arms to obtain the cut forces and moments. The relevant model outputs – also referred to as interesting quantities – are the nodal accelerations  $_g\ddot{\mathbf{u}}$  and the cut loads  $_c\mathbf{P}$ . See [Bisplinghoff, Ashley, and Halfman \(1955\)](#), [Rodden and Johnson \(2004\)](#) and [Kier \(2011\)](#) for details.

The Digital-X structure model is depicted in [Figure 2.3](#). It consists of 188 nodes, which corresponds to 1128 DOF. For the modal model, 50 modes are used. The first and the second mode shape are additionally depicted in [Figure 2.3](#). The  $c$ -set has 1188 DOF.

### 2.1.2 Aerodynamic Model

The steady aerodynamic model is based on the vortex lattice method (VLM) which uses concepts of potential flow. This means that the velocity field is the gradient of a scalar valued potential function. The lifting surfaces of the aircraft are discretized by trapezoidal shaped aerodynamic boxes – also called panels. A horse shoe vortex is placed at the  $1/4$  chord of every panel, see [Figure 2.4a](#). The circulation strengths of all vortices are chosen such that the boundary conditions are fulfilled. This means that there is no flow through the solid surfaces and that there is no flow around the trailing edge. To that end, the orthogonal component of the flow at the  $3/4$  chord of every panel  $_j\mathbf{v}$  ( $j$ -set, see [Figure 2.4b](#)) is considered and normalized with the flight speed  $U_\infty$ . This leads to the downwash

$$_j\mathbf{w} = \frac{_j\mathbf{v}}{U_\infty}, \quad (2.10)$$

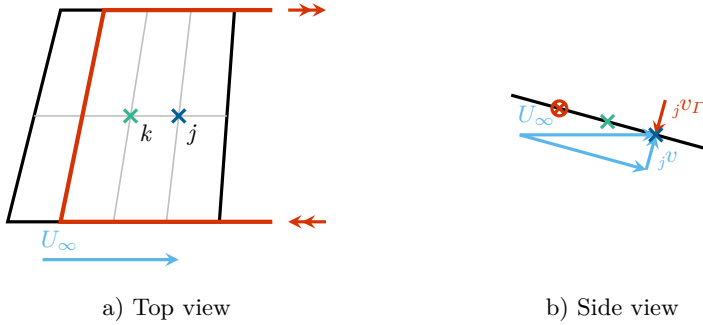


**Figure 2.4:** Aerodynamic box for the VLM: The horse shoe vortex is placed on the 1/4 chord point and extended to infinity. The 3/4 chord point (✕) is the collocation point ( $j$ -set). The vortex strength is chosen such that  $jv_r$  compensates  $jv$  and thus the boundary condition is fulfilled. The box reference point ( $k$ -set) is ✕.

which can be understood as the local angle of attack (using the small-angle approximation). The VLM results eventually in the so-called aerodynamic influence coefficient (AIC) matrix  $_{jj}\mathbf{Q}$ , which maps the downwash to the pressure coefficients

$$\Delta \mathbf{c}_p = _{jj}\mathbf{Q} _j\mathbf{w} . \quad (2.11)$$

Next, the dynamic pressure is computed from the air density  $\rho$  and  $U_\infty$  as

$$p_\infty = \frac{1}{2}\rho U_\infty^2 . \quad (2.12)$$

This enables to compute the pressure distribution by

$$\Delta \mathbf{p} = p_\infty _{jj}\mathbf{Q} _j\mathbf{w} . \quad (2.13)$$

It should be noted that – contrary to this notation – the pressure acts on the 1/4 chord and not on the  $j$ -set. Further, the AIC matrix depends on the Mach number<sup>3</sup>. Details can be found in [Hedman \(1966\)](#) and [Rodden and Johnson \(2004\)](#). The VLM grid (with 1856 panels) of the Digital-X model and the pressure distribution for a constant angle of attack are illustrated in [Figure 2.5](#).

The VLM is only valid for a steady flow. Since the aerodynamic boundary condition changes rapidly during a gust encounter, using the VLM would introduce severe modeling errors. To avoid this, unsteady aerodynamic effects are involved using the doublet lattice method (DLM) which is the unsteady counterpart of the VLM. In principle, the horse shoe vortices are replaced by pulsating doublet lines. Eventually, this leads to a harmonic solution in the frequency domain:

$$\Delta \mathbf{c}_p(j\bar{\omega}) = _{jj}\mathbf{Q}(j\bar{\omega}) _j\mathbf{w}(j\bar{\omega}) . \quad (2.14)$$

<sup>3</sup>The Mach number  $Ma$  is defined as  $Ma = U_\infty/a$  where  $a$  is the speed of sound.

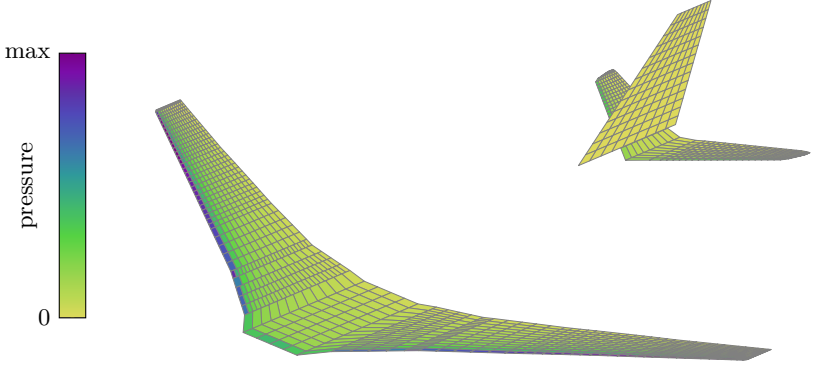


**Figure 2.5:** Aerodynamic model: pressure distribution for a constant angle of attack.

The constant AIC matrix is hence replaced by a transfer function matrix. In (2.14),

$$\bar{\omega} = \frac{c_{\text{ref}}/2}{U_{\infty}} \omega \quad (2.15)$$

is the reduced frequency and  $c_{\text{ref}}$  is the reference chord length. Note that the DLM provides no analytical function  ${}_{jj}\mathbf{Q}(\bar{j}\omega)$  but constant matrices for discrete values of  $\bar{\omega}$ . Since the DLM is numerically expensive, the AIC matrix is usually computed only for a couple of reduced frequencies. Further frequency points are obtained by interpolation. It should be mentioned that the DLM converges to the VLM solution if  $\bar{\omega}$  tends to zero. See Albano and Rodden (1969) and Rodden and Johnson (2004) for details.

At this point, it is noted that atmospheric parameters are determined using the international standard atmosphere. This means, the air density  $\rho$ , the speed of sound  $a$ , etc. are functions of the altitude  $h$ . Further parameters such as the Mach number  $Ma$  and the dynamic pressure  $p_{\infty}$  can be determined using the flight speed  $U_{\infty}$ .

In order to complete the aeroelastic interconnection, structural or modal deflections have to be transformed to the aerodynamic grid. Analogously, the pressure distribution must be transformed to loads acting on the structure. This is achieved by the transformation

$${}_g\mathbf{P}_{\text{eig}}(\bar{j}\omega) = p_{\infty} \underbrace{{}_{kg}\mathbf{T}^{\text{T}} \quad {}_{kj}\mathbf{S} \quad {}_{jj}\mathbf{Q}(\bar{j}\omega) \quad ({}_{jk}\mathbf{D}_{\text{x}} + \bar{j}\bar{\omega} \quad {}_{jk}\mathbf{D}_{\text{t}})}_{{}_{gh}\mathbf{Q}(\bar{j}\omega)} \quad {}_{kg}\mathbf{T} \quad {}_{gh}\mathbf{\Phi} \quad {}_h\mathbf{u}(\bar{j}\omega). \quad (2.16)$$

The single steps of the transformations are explained proceeding from right to left. First, the modal matrix  ${}_{gh}\mathbf{\Phi}$  is used to compute the structural deformation. The

spline matrix  ${}_{kg}\mathbf{T}$  transforms the structural deformations to the aerodynamic panel reference points. This is achieved by a surface interpolation based on radial basis functions. Note that the rotational DOF are explicitly considered in this step. The differentiation matrices  ${}_{jk}\mathbf{D}_x$  and  ${}_{jk}\mathbf{D}_t$  allow to compute the downwash which is induced from deflections and velocities of the panel reference points. The surface matrix  ${}_{kj}\mathbf{S}$  maps the panel pressure acting on the 1/4 chord to forces and moments w.r.t. the panel midpoint. In order to transform the aerodynamic forces onto the structural grid, the transposed spline matrix  ${}_{kg}\mathbf{T}^T$  is reused, which can easily be motivated by the concept of virtual work. The resulting transfer matrix  ${}_{gh}\mathbf{Q}$  is referred to as generalized AIC matrix.<sup>4</sup> Note that all transformations except of the modal matrix are pure geometrical mappings. See [Rodden and Johnson \(2004\)](#) and [Kier \(2011\)](#) for details.

In a similar fashion, the AIC matrices for the control surface deflection  ${}_x\mathbf{u}$  can be defined which leads to

$${}_g\mathbf{P}_{cs}(\mathrm{j}\bar{\omega}) = p_\infty {}_{gx}\mathbf{Q}(\mathrm{j}\bar{\omega}) {}_x\mathbf{u}(\mathrm{j}\bar{\omega}). \quad (2.17)$$

To that end,  ${}_{kg}\mathbf{T} {}_{gh}\mathbf{\Phi}$  in (2.16) is replaced by the control surface matrix  ${}_{kx}\mathbf{\Phi}$ . This matrix contains the relation between control surface deflections and the panel movement.

Concerning the gust input, recall that the wind field is assumed to be one dimensional and the gust velocity is acting either vertically or laterally to the flight direction. Consequently, the normalized gust velocity at the aircraft nose  ${}_Gw$  acts time delayed at different 3/4 chord points. Additionally, only the normal component of the gust to the panel must be used. For one panel, this leads to the downwash

$${}_jw(\mathrm{j}\bar{\omega}) = \underbrace{{}_n\mathbf{n}_{\text{panel}} {}_n\mathbf{n}_{\text{gust}}^T \mathrm{e}^{-(2x_{\text{panel}}/c_{\text{ref}})\cdot\mathrm{j}\bar{\omega}}}_{jGT} {}_Gw(\mathrm{j}\bar{\omega}), \quad (2.18)$$

where  $\mathbf{n}_{\text{panel}}$  and  $\mathbf{n}_{\text{gust}}$  are the panel normal and the gust direction respectively. The distance between the aircraft nose and the 3/4 chord point is  $x_{\text{panel}}$ . The time delay is transferred into the reduced frequency domain in order to combine the delay with the AIC matrix. If all panels are considered, all  $jGT$  are collected in a column vector. The combination of this vector with the  ${}_{jj}\mathbf{Q}$  and the transformation to the structural grid as in (2.16) leads to the following mapping between the gust input and the nodal forces:

$${}_g\mathbf{P}_{\text{gust}}(\mathrm{j}\bar{\omega}) = p_\infty {}_{gG}\mathbf{Q}(\mathrm{j}\bar{\omega}) {}_Gw(\mathrm{j}\bar{\omega}). \quad (2.19)$$

Summarizing, the aerodynamic forces are

$${}_g\mathbf{P}_{\text{aero}} = {}_g\mathbf{P}_{\text{eig}} + {}_g\mathbf{P}_{\text{cs}} + {}_g\mathbf{P}_{\text{gust}} = p_\infty \begin{bmatrix} {}_{gh}\mathbf{Q} & {}_{gx}\mathbf{Q} & {}_{gG}\mathbf{Q} \end{bmatrix} \begin{bmatrix} {}_h^u \\ {}_x^u \\ {}_G^w \end{bmatrix}. \quad (2.20)$$

---

<sup>4</sup>Note that  ${}_{gh}\mathbf{Q}$  is only half generalized, because only the deflections but not the forces are generalized.

Note that the three transfer matrices  ${}_{gh}\mathbf{Q}$ ,  ${}_{gx}\mathbf{Q}$ , and  ${}_{gG}\mathbf{Q}$  depend on the flight speed and on the Mach number.

### 2.1.3 Model Integration in the Frequency Domain

Since the elements of the AIC transfer matrix are no rational functions but given as tabulated data for discrete frequencies, a state space representation of an aeroelastic model cannot be directly derived. Consequently, gust loads computation is usually performed in the frequency domain by means of the fast Fourier transform (FFT) framework (see Bisplinghoff, Ashley, and Halfman, 1955; Rodden and Johnson, 2004). Substituting the aerodynamic forces (2.20) into (2.5) leads to

$$\begin{aligned} (-\omega^2 {}_{hh}\mathbf{M} + j\omega {}_{gg}\mathbf{B} + {}_{hh}\mathbf{K}) {}_h\mathbf{u} = \\ p_\infty {}_{gh}\mathbf{\Phi}^T ({}_{gh}\mathbf{Q}(j\bar{\omega}) {}_h\mathbf{u} + {}_{gx}\mathbf{Q}(j\bar{\omega}) {}_x\mathbf{u} + {}_{gj}\mathbf{Q}(j\bar{\omega}) {}_j\mathbf{w}_{\text{gust}}) , \end{aligned} \quad (2.21)$$

which results in

$$\begin{aligned} {}_h\mathbf{u} = p_\infty \left( -\omega^2 {}_{hh}\mathbf{M} + j\omega {}_{gg}\mathbf{B} + {}_{hh}\mathbf{K} - p_\infty {}_{gh}\mathbf{\Phi} {}_{gh}\mathbf{Q}(j\bar{\omega}) \right)^{-1} \cdot \\ {}_{gh}\mathbf{\Phi}^T ({}_{gx}\mathbf{Q}(j\bar{\omega}) {}_x\mathbf{u} + {}_{gj}\mathbf{Q}(j\bar{\omega}) {}_j\mathbf{w}_{\text{gust}}) . \end{aligned} \quad (2.22)$$

From (2.22), the nodal and cut loads can be determined using (2.7) and (2.9).

The resulting frequency response functions (FRFs) from the lateral and the vertical gust input to the vertical acceleration, the wing root bending moment, and the VTP root bending moment are depicted in Figure 2.6.

### 2.1.4 Model Integration in the Time Domain

Although the frequency domain model is convenient for many problems, a time domain representation is required in some cases, e.g., for controller design or in combination with nonlinearities. To that end, Roger (1977) propose to perform a rational function approximation (RFA), e.g., to approximate  ${}_{gh}\mathbf{Q}$  by

$${}_{gh}\mathbf{Q}(j\bar{\omega}) \approx {}_{gh}\bar{\mathbf{Q}}(j\bar{\omega}) = {}_{gh}\bar{\mathbf{Q}}_0 + {}_{gh}\bar{\mathbf{Q}}_1 j\bar{\omega} - {}_{gh}\bar{\mathbf{Q}}_2 \bar{\omega}^2 + \sum_{i=1}^{n_p} {}_{gh}\bar{\mathbf{Q}}_{p_i} \frac{j\bar{\omega}}{j\bar{\omega} + p_i} , \quad (2.23)$$

where  $p_i$  are the manually chosen poles of the approximation. Because the coefficients  ${}_{gh}\bar{\mathbf{Q}}_0$ ,  ${}_{gh}\bar{\mathbf{Q}}_1$ ,  ${}_{gh}\bar{\mathbf{Q}}_2$ , and  ${}_{gh}\bar{\mathbf{Q}}_{p_i}$  appear linearly in (2.23), they can be determined by linear least squares techniques. Replacing  $j\bar{\omega}$  with the reduced Laplace variable

$$\bar{s} = \frac{c_{\text{ref}}/2}{U_\infty} s \quad (2.24)$$

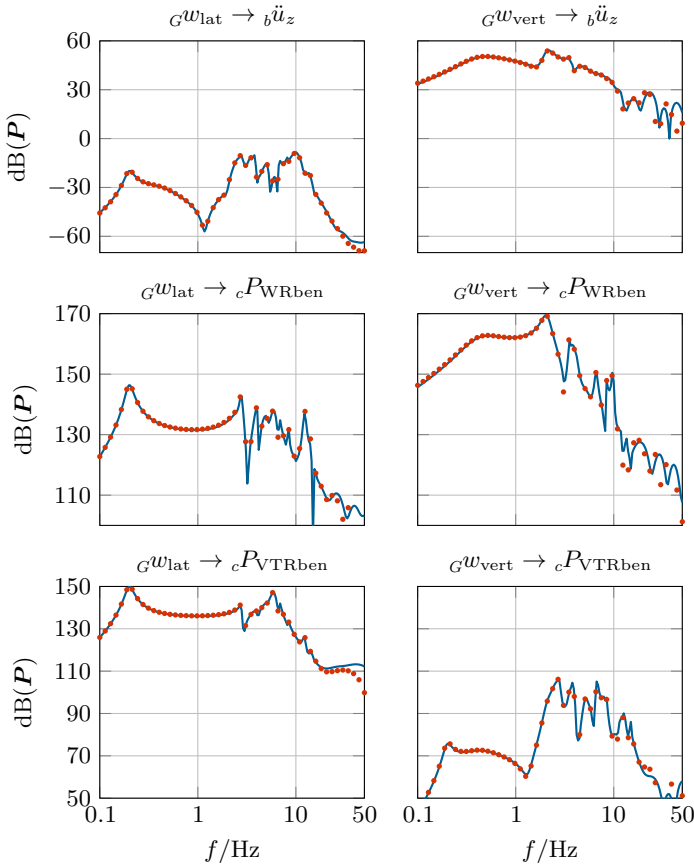


**Figure 2.6:** FRFs of the gust loads model: The FRF from the lateral and the vertical gust and to the vertical acceleration ( ${}_b\ddot{u}_z$ ), the wing root bending moment ( ${}_cP_{\text{WRben}}$ ), and the VTP root bending moment ( ${}_cP_{\text{VTRben}}$ ) are depicted. The Mach number is  $Ma = 0.86$  and the altitude is  $h = 9.075$  km. An excellent agreement between the frequency domain model ( $\bullet$ ) and the state space model ( $\text{—}$ ) can be seen.

results in a rational transfer matrix  $_{gh}\bar{\mathbf{Q}}(\bar{s})$  which can be expressed in a state space representation. The additional states are called lag states. The transfer matrix  $_{gh}\bar{\mathbf{Q}}(\bar{s})$  is not proper<sup>5</sup> but derivatives of  $_{gh}\mathbf{u}$  are available from the structural model. See Kier (2011) for details.

Analogously,  $_{gx}\mathbf{Q}$  can be approximated for the control surfaces deflection input. Because the first and the second time derivatives are in general not available,  $_{gx}\bar{\mathbf{Q}}_1$  and  $_{gx}\bar{\mathbf{Q}}_2$  are often omitted for the RFA. Alternatively, their differentiating behavior can be approximated using high-frequency low-pass filters.

The approximation of the gust input is a bit more complex. The reason is that the time delay causes a high phase shift which cannot be accurately approximated with (2.23). As a remedy, Karpel, Moulin, and Chen (2003) proposed to divide the gust model into several zones (here 25 per gust direction), each having its own reference point, see Figure 2.7. Recall that the time delay is modeled in the reduced frequency. The very small time delay between the 3/4 chord point and the preceding reference point

$$e^{-(2\Delta x_{\text{RFA}}/c_{\text{ref}})\bar{\omega}} \quad (2.25)$$

is captured by the RFA. To include the delays between the single gust zones, Padé approximations of the dead times are cumulatively applied:

$$e^{-(2\Delta x_{\text{zone}}/c_{\text{ref}})\bar{\omega}} \approx \frac{c_{\text{ref}} - x_{\text{zone}}\bar{\omega}}{c_{\text{ref}} + x_{\text{zone}}\bar{\omega}}. \quad (2.26)$$

Based on physical considerations, the term  $_{gG}\bar{\mathbf{Q}}_2$  is dropped (Kier, 2011). The term  $_{gG}\bar{\mathbf{Q}}_1$  is approximated using high-frequency low-pass filters.

At this point, all transfer matrices are expressed by rational functions which allows to assemble the complete model in a state space representation. In case of the considered Digital-X model, the resulting model has 1036 states. The states from the structural dynamics are three rotational rigid body positions<sup>6</sup>, five rigid body velocities<sup>7</sup>, 50 modal deflections and 50 modal velocities. The aerodynamics contribute with 880 lag states and 48 states for the Padé approximations. The inputs are the lateral and the vertical gust downwash as well as four control surface deflections (horizontal stabilizer, aileron, elevator and rudder). The outputs are the nodal accelerations (1128 DOF) and the cut loads (1188 DOF).

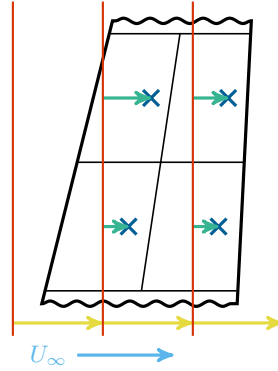
As an example, a Bode diagram from the lateral and the vertical gust input to the vertical acceleration, the wing root bending moment, and the VTP root bending moment is depicted in Figure 2.6. An excellent agreement to the frequency domain model can be recognized.

<sup>5</sup>A rational transfer function is proper if the number of zeros is less or equal to the number of poles.

<sup>6</sup>The translational rigid body positions do not affect the model.

<sup>7</sup>The velocity in flight direction is considered to be constant.

**Figure 2.7:** Gust zones for Padé approximation: An excerpt of the wing consisting of two times two panels is depicted. The 3/4 chord point of every panel is shown by  $\times$  and the reference point of every gust zone is —. The time delay between the single gust zones  $\Delta x_{\text{zone}}/U_{\infty}$  ( $\rightarrow$ ) is cumulatively approximated using Padé filters. The small time delay between the 3/4 chord point and the preceding reference point  $\Delta x_{\text{RFA}}/U_{\infty}$  ( $\rightarrow$ ) is captured by the RFA.



## 2.2 Computation of Maximum Gust Loads

According to [EASA CS-25](#), two types of disturbances have to be considered: discrete “one-minus-cosine” gusts and continuous turbulence. The first case represents an idealization of a single extreme turbulence event which allows to compute deterministic limit loads. The other type of excitation, continuous turbulence, considers the stochastic nature of turbulence. Here, the von Kármán wind turbulence spectrum is applied to white noise in order to create aircraft excitations. The simulation results are evaluated by stochastic means and the most important quantities are the RMS values of the interesting quantities. This thesis treats “one-minus-cosine” gusts.

### 2.2.1 The “One-Minus-Cosine” Gust Scenario

The gust loads are composed of two parts: trim loads and dynamic loads. The static loads result from the trimmed horizontal flight and are consequently also called trim loads. The dynamic loads are caused by the gust excitation and are referred to as incremental loads. Because of the linear model, both components can be simply superimposed, i.e.,

$${}_c\mathbf{P} = {}_c\mathbf{P}_{\text{trim}} + {}_c\mathbf{P}_{\text{incremental}}. \quad (2.27)$$

In order to trim the aircraft, trim conditions for the model states have to be specified. Usually, the vertical acceleration is constrained by the acceleration of gravity and other accelerations and velocities are set to zero. This allows to compute the structural deformation as well as the angle of attack and the control surface deflections. The resulting structural forces are the trim loads.

To determine the incremental loads, the aircraft is excited by “one-minus-cosine” gusts. This gust shape is defined by

$$Gw(t) = \begin{cases} \frac{U_{ds}}{2U_{\infty}} \left( 1 - \cos \left( \pi \frac{U_{\infty} t}{H} \right) \right) & \text{if } 0 \leq U_{\infty} t \leq 2H \\ 0 & \text{otherwise,} \end{cases} \quad (2.28)$$

where  $H$  is the gust length and  $U_{ds}$  is the gust design speed. According to EASA CS-25, 20 gust lengths between 9 m and 107 m (30 ft and 350 ft) have to be considered. The gust design speed is

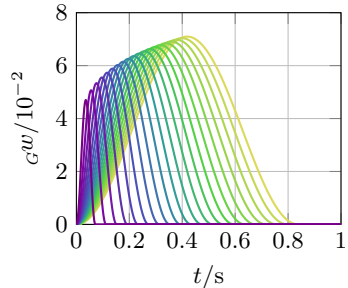
$$U_{ds} = U_{ref} \cdot F_g \cdot \left( \frac{H}{107 \text{ m}} \right)^{1/6}. \quad (2.29)$$

The reference gust velocity  $U_{ref}$  and the flight profile alleviation factor  $F_g$  depend on many aircraft parameters (e.g., the maximum operating altitude and the maximum takeoff weight) as well as on the considered flight point (see EASA CS-25). In Figure 2.8, “one-minus-cosine” gusts are depicted for several gust lengths. Simulation results are depicted for the vertical acceleration, the wing root bending moment and the VTP root bending moment in Figure 2.9. The maximum absolute incremental loads are referred to as peak loads.

Obviously, the lateral gust does not affect the wing loads. Similarly, the VTP is not impacted by the vertical gust. This allows to focus on specific interesting quantities depending on the gust direction. For the lateral gust, the relevant outputs are the VTP shear force, torsional moment, and bending moment along the VTP loads reference axis. In case of a vertical gust, the interesting quantities are the wing and the HTP shear force, torsional moment, and bending moment. These three quantities are also referred to as shear  ${}_cP_{sh}$ , torsional  ${}_cP_{tor}$ , and bending  ${}_cP_{ben}$  in the remainder of this thesis.

The eventually interesting numbers are the maximum upper and minimum lower loads of all interesting quantities. They are computed by superimposing the trim

**Figure 2.8:** “One-minus-cosine” gust excitation: Different gust lengths between 9 m and 107 m are depicted. The flight point is specified by  $Ma = 0.86$  and  $h = 9.075$  km.



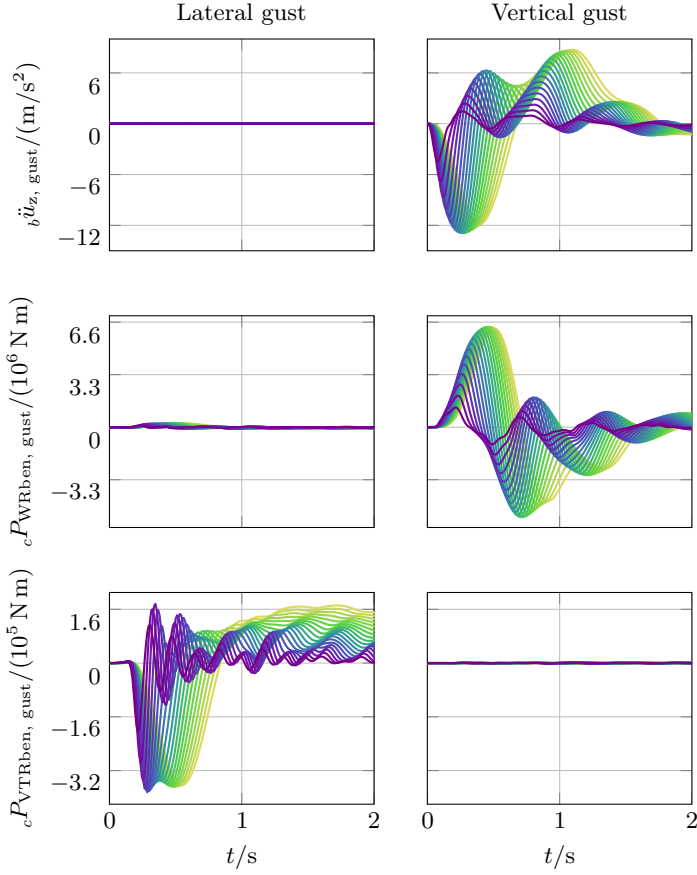


**Figure 2.9:** Simulation results for lateral and vertical gusts: The vertical acceleration ( ${}_b\ddot{u}_z$ ), the wing root bending moment ( ${}_cP_{\text{WRben}}$ ), and the VTP root bending moment ( ${}_cP_{\text{VTRben}}$ ) are depicted. The Mach number is  $Ma = 0.86$  and the altitude is  $h = 9.075 \text{ km}$ .

loads and the peak loads, e.g.,

$${}_c\mathbf{P}_{\text{upper}} = {}_c\mathbf{P}_{\text{trim}} + \max_t |{}_c\mathbf{P}_{\text{gust}}| \quad (2.30)$$

and

$${}_c\mathbf{P}_{\text{lower}} = {}_c\mathbf{P}_{\text{trim}} - \max_t |{}_c\mathbf{P}_{\text{gust}}|. \quad (2.31)$$

The reason for the “+” and the “−” sign is that the gust can also act from the opposing direction. Taking the maximum/minimum of all upper/lower loads results in the limit loads. In order to size the structure, a safety factor of 1.5 is finally added to the limit loads. The resulting bounds for the upper and lower loads in the considered example are compiled in [Table 2.1](#)

**Table 2.1:** Bounds of the upper and lower loads for the considered example.

	$\frac{{}_v\ddot{b}_z}{m/s^2}$	$\frac{{}_cP_{\text{WRben}}}{10^6 \text{ N m}}$	$\frac{{}_cP_{\text{VTRben}}}{10^5 \text{ N m}}$
Trim loads	−9.81	5.40	0.00
Peak loads (lateral gust)	0.00	0.21	3.15
Peak loads (vertical gust)	11.22	5.80	0.00
Upper limit loads	1.42	11.20	3.15
Lower limit loads	−21.03	−0.40	−3.15

## 2.2.2 Number of Load Cases

The discrete gust scenario described above must be investigated for multiple load cases such that the entire design envelope of the aircraft is covered:

**Flight points:** The gust loads are affected by the considered flight condition which is specified by the flight speed and the altitude. Other parameters – e.g., the Mach number or the air density – can be derived using the international standard atmosphere. Note that the flight envelope represents a continuous space which must be approximated by a grid in order to perform the gust simulation.

**Wing configurations:** Aircraft are mostly equipped with slats and flaps which allow to operate the aircraft at a higher angle of attack during takeoff and landing. These so-called high-lift configurations have to be considered during the gust analysis. On the contrary to the flight envelope, there is only a limited number of wing configurations. Usually, every wing configuration results in a new VLM/DLM model.

**Mass cases:** Since the aircraft consumes fuel and it can be fully occupied or be empty, different mass distributions have to be considered. Similar to the flight envelope, a finite grid of mass cases is used for the simulations.

**Flight control modes:** A typical civil transport aircraft is equipped with different flight control modes which have to be considered for the analysis. The normal control law provides several protections from potentially dangerous flight states, such as over-speed or too large an angle of attack. In cases of a sensor or an actuator failure, different fall-back control laws might be activated. In the worst case scenario, all protections are lost and the aircraft is operated in an open loop configuration.

**Gust lengths and gust directions:** As already mentioned, several gust lengths and two gust directions have to be taken into account while determining the limit loads.

The permutations of all these cases must be considered. The number of load cases is estimated in [Table 2.2](#). Facing the number of eight million simulations, it becomes clear that gust loads analysis is a challenging issue. However, the focus of this thesis lies on different flight points and different gust excitations. A clean wing configuration and a full fuel tank are considered. One open loop and one closed loop setup are studied in the remainder of this thesis.

### 2.2.3 Covering the Flight Envelope

The flight envelope of the Digital-X model is depicted in [Figure 2.10](#). The [EASA CS-25](#) states that flight points both on the border and inside of the envelope have to be considered. Here, 51 flight points are used as indicated in [Figure 2.10](#). The air density and the gravitational accelerations can be computed from the altitude. In combination with the flight speed, the Mach number can also be specified. Note that a reduced gust design speed is considered for flight velocities greater than the maximum cruising speed as indicated in [Figure 2.10](#).

**Table 2.2:** Estimated number of load cases.

	50	flight points
×	10	wing configurations
×	100	mass cases
×	4	control modes
×	20	gust lengths
×	2	gust directions
<hr/>		
=	8 000 000	load cases

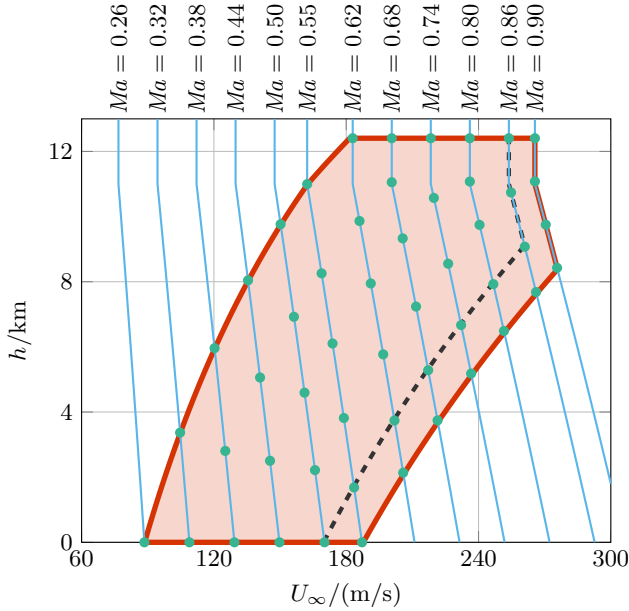


**Figure 2.10:** Flight envelope of the Digital-X model. The points  $\bullet$  are considered for the analysis. The maximum cruising speed is plotted by  $---$ . Constant Mach numbers are indicated by  $---$ .

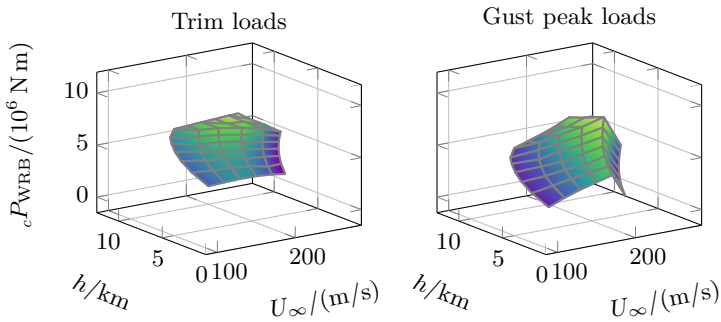


**Figure 2.11:** Trim and gust peak loads of the wing root bending moment w.r.t. the flight envelope.

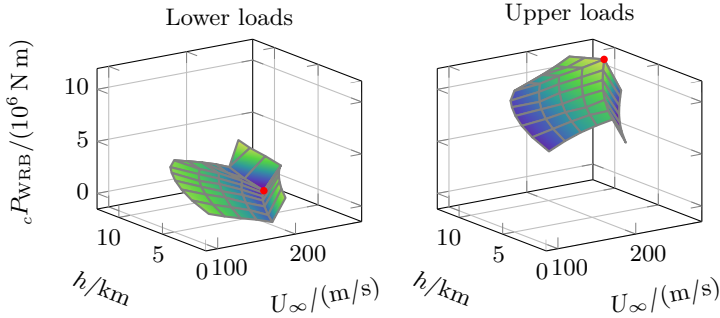


**Figure 2.12:** Maximum upper and minimum lower values of the wing root bending moment w.r.t. the flight envelope: The maximum upper and the minimum lower point is each marked by  $\bullet$ .

The resulting trim and gust peak loads of the open loop model w.r.t. the flight envelope are depicted for the wing root bending moment in Figure 2.11. While the trim loads are almost constant, the gust loads vary intensively. The kink for large flight speeds results from the reduced gust design speed above the maximum cruising speed.

The resulting limit loads for the wing root bending moment are depicted in Figure 2.12. Here, the worst case flight point is specified by  $U_\infty = 261$  m/s and  $h = 9.075$  km. However, for the other interesting quantities or in the closed loop case, different critical flight points can be identified. Note that the worst upper and lower loads can appear at different points.

The limit loads of all interesting quantities occur at different points in time. Consequently, they do not fulfill the balance of forces, i.e., the sum of all forces is not equal to zero. During the detailed loads analysis of one component, the considered part is cut free and the cut loads are considered as external forces. In order to avoid a drifting of the component, the balance of forces needs to be fulfilled. To that end, the so-called correlated loads are considered where the cut loads of the same point in time are used. However, this subordinated step is not treated in this thesis.

#### 2.2.4 Techniques for an Efficient Estimation of Maximum Gust Loads

Since these millions of simulations are time consuming, there is a need for fast and reliable algorithms to identify critical load cases. Despite of this, the literature on efficient estimation methods of worst case loads is sparse and the focus lies

on continuous turbulence. Pototzky, Zeiler, and Perry (1991) and Zeiler (1997) use matched filter concepts. This method allows to determine an excitation with unit energy for a single-input single-output (SISO) system which results in a maximum peak of the output. However, it was primarily used in order to determine correlated loads from continuous turbulence results. Fidkowski et al. (2008) use a Lyapunov based approach to compute the RMS values of the model output due to a gust excitation. This approach corresponds to computing the  $\mathcal{H}_2$  norm and the considered interpretation is well-known in control theory.

Khodaparast et al. (2011) and Khodaparast et al. (2012) propose two approaches for an efficient prediction of maximum gust loads: surrogated modeling and “anti optimization”. The idea of the surrogated modeling is to simulate only few points of the flight envelope and to obtain the remaining points by interpolation. The “anti optimization” aims at finding the worst flight point by optimizing the model parameters such that maximum loads are generated. In both approaches, only the load cases resulting from the flight envelope are considered. In Khodaparast and Cooper (2013), these approaches are extended for correlated loads. A severe drawback of both ideas is that critical flight points can easily be missed. Additionally, the simulation of the considered flight points can still be time consuming.

## 3 Robust Performance Analysis

This chapter introduces the theoretical background of robust performance analysis. In [Section 3.1](#), the notation and important preliminaries on signal norms, LTI models, LMIs and SDPs are presented. Parametric uncertainties and LPV models are introduced in [Section 3.2](#). The analysis of these models is discussed in [Section 3.3](#), where the focus lies on the worst case energy-to-peak gain. [Section 3.4](#) treats techniques for infinite dimensional LMIs. The chapter closes with a numerical benchmark of these techniques in [Section 3.5](#). The results from [Sections 3.4](#) and [3.5](#) are already partially published in [Knoblauch et al. \(2013\)](#).

### 3.1 Preliminaries

Standard notation is mostly used in this thesis. Scalar variables are denoted in normal font-weight, e.g.,  $a$ . Vectors are indicated by bolt small letters  $\mathbf{a}$  and matrices by capital bold letters  $\mathbf{A}$ . The set of real numbers is denoted  $\mathbb{R}$ , the set of nonnegative real numbers  $\mathbb{R}_+$ , and the set of complex numbers  $\mathbb{C}$ .  $\mathbb{R}^{n \times m}$  and  $\mathbb{C}^{n \times m}$  denote the sets of  $n \times m$  matrices whose elements are in  $\mathbb{R}$  and  $\mathbb{C}$ , respectively. A single superscript is used for vectors, i.e.,  $\mathbb{R}^n = \mathbb{R}^{n \times 1}$ . For a complex number  $a \in \mathbb{C}$ ,  $\bar{a}$  denotes the complex conjugate. The transpose of a matrix  $\mathbf{A} \in \mathbb{C}^{n \times m}$  is denoted  $\mathbf{A}^T$  and the complex conjugate transpose  $\mathbf{A}^*$ .  $\mathbb{S}^n \subset \mathbb{R}^{n \times n}$  refers to  $n \times n$  symmetric matrices, i.e.,  $\mathbf{A} \in \mathbb{S} \Leftrightarrow \mathbf{A} = \mathbf{A}^T$ . The set of Hermitian matrices  $\mathbf{A} = \mathbf{A}^*$  is denoted  $\mathbb{H}^n \subset \mathbb{C}^{n \times n}$ .

#### 3.1.1 Signal Norms

An  $n$ -dimensional signal  $\mathbf{x}: \mathbb{R}_+ \rightarrow \mathbb{R}^n$  is a function  $\mathbf{x}$  of the time  $t$ . The time argument of signals is usually omitted in order to simplify the notation. Important signal norms and signal spaces are defined below.

**Definition 3.1** ([Skogestad and Postlethwaite, 1996](#)): The  $\mathcal{L}_2$  norm of a signal  $\mathbf{x}$  is defined as

$$\|\mathbf{x}\|_{\mathcal{L}_2} := \sqrt{\int_0^\infty \|\mathbf{x}(t)\|_2^2 dt} = \sqrt{\int_0^\infty \mathbf{x}(t)^T \mathbf{x}(t) dt}. \quad (3.1)$$

The  $\mathcal{L}_2$  norm can be interpreted as the energy of a signal. Accordingly, it is also referred to as energy norm. The notation  $\mathbf{x} \in \mathcal{L}_2^n$  refers to  $n$ -dimensional signals

with a finite  $\mathcal{L}_2$  norm. The  $\mathcal{L}_2$  space is a subset of the extended space  $\mathcal{L}_{2e}$  whose members must be square integrable only on finite intervals (Megretski and Rantzer, 1997).

**Definition 3.2** (Skogestad and Postlethwaite, 1996): The  $\mathcal{L}_\infty$  norm of a signal  $\mathbf{x}$  is defined as

$$\|\mathbf{x}\|_{\mathcal{L}_\infty} := \sup_{t \in \mathbb{R}_+} \|\mathbf{x}(t)\|_2 = \sup_{t \in \mathbb{R}_+} \sqrt{\mathbf{x}(t)^\top \mathbf{x}(t)}. \quad (3.2)$$

For scalar valued signals  $x$ , the  $\mathcal{L}_\infty$  norm represents the maximum peak of the signal. Hence, it is also referred to as peak norm of a signal. The notation  $\mathbf{x} \in \mathcal{L}_\infty^n$  refers to  $n$ -dimensional signals with a finite  $\mathcal{L}_\infty$  norm. It should be noted that there exists a second slightly different definition in the literature (see Rotea, 1993). Here  $\mathcal{L}_\infty$  refers always to Definition 3.2.

### 3.1.2 LTI Systems

An LTI system  $\mathbf{P}$  is defined by the linear differential equation

$$\dot{\mathbf{x}} = \mathbf{A}\mathbf{x} + \mathbf{B}\mathbf{d}, \quad \mathbf{x}(0) = \mathbf{x}_0 \quad (3.3a)$$

$$\mathbf{e} = \mathbf{C}\mathbf{x} + \mathbf{D}\mathbf{d} \quad (3.3b)$$

and maps an input vector  $\mathbf{d}: \mathbb{R}_+ \rightarrow \mathbb{R}^{n_d}$  to an output vector  $\mathbf{e}: \mathbb{R}_+ \rightarrow \mathbb{R}^{n_e}$ . In (3.3),  $\mathbf{x}: \mathbb{R}_+ \rightarrow \mathbb{R}^{n_x}$  is the state vector,  $\mathbf{x}_0 \in \mathbb{R}^{n_x}$  the initial condition,  $\mathbf{A} \in \mathbb{R}^{n_x \times n_x}$  the system matrix,  $\mathbf{B} \in \mathbb{R}^{n_x \times n_d}$  the input matrix,  $\mathbf{C} \in \mathbb{R}^{n_e \times n_x}$  the output matrix, and  $\mathbf{D} \in \mathbb{R}^{n_e \times n_d}$  the feed-through matrix. Its transfer function is denoted as

$$\mathbf{P}(s) = \mathbf{C}(s\mathbf{I} - \mathbf{A})^{-1}\mathbf{B} + \mathbf{D}, \quad (3.4)$$

where  $s$  is the Laplace variable. The notation  $\mathbf{P}(j\omega)$  is used for the frequency response function (FRF).

### 3.1.3 Semidefinite Programs and Linear Matrix Inequalities

Many important problems in control theory can be expressed by LMIs and SDPs (see e.g., Boyd et al., 1994; Wu, 2001; Dettori, 2001). Both LMIs and SDPs are convex optimization problems<sup>1</sup>. Before LMIs and SDPs are defined below, positive and negative definite matrices are introduced first.

A matrix  $\mathbf{M} \in \mathbb{C}^{m \times m}$  is (semi) positive definite if  $\mathbf{u}^\top \mathbf{M} \mathbf{u} > 0$  ( $\mathbf{u}^\top \mathbf{M} \mathbf{u} \geq 0$ ) holds for all  $\mathbf{u} \in \mathbb{R}^m \setminus \{\mathbf{0}\}$ . In this case the notation  $\mathbf{M} > 0$  ( $\mathbf{M} \geq 0$ ) is used. Analogously,  $\mathbf{M} < 0 \Leftrightarrow -\mathbf{M} > 0$  is used for negative definite matrices. The notation  $\mathbf{M}_1 > \mathbf{M}_2$  means  $\mathbf{M}_1 - \mathbf{M}_2 > 0$ . Finally, a Hermitian matrix  $\mathbf{M} \in \mathbb{H}^m$  is positive definite if and only if all eigenvalues  $\text{eig}(\mathbf{M})$  are positive. Note that all eigenvalues of a Hermitian matrix are real numbers.

<sup>1</sup>Details on convex optimization are briefly explained in Appendix A.

**Definition 3.3** (Boyd et al., 1994): Using the matrices  $\mathbf{M}_0, \mathbf{M}_1, \dots, \mathbf{M}_n \in \mathbb{H}^m$  and the variables  $x_i$  collected in the vector  $\mathbf{x} \in \mathbb{R}^n$ , a linear matrix inequality (LMI) is a constraint of the form

$$\mathbf{M}(\mathbf{x}) = \mathbf{M}_0 + \mathbf{M}_1 x_1 + \dots + \mathbf{M}_n x_n > 0. \quad (3.5)$$

Note that the mapping  $\mathbf{M}: \mathbb{R}^n \rightarrow \mathbb{H}^m$  is affine.

**Definition 3.4** (Boyd et al., 1994): A semidefinite program (SDP) is a convex optimization problem with a linear objective function and LMI constraints. Using the variables from Definition 3.3 and a vector  $\mathbf{c} \in \mathbb{R}^n$ , an SDP is defined by

$$\min_{\mathbf{x}} \mathbf{c}^T \mathbf{x}, \quad \text{s.t.} \quad \mathbf{M}(\mathbf{x}) > 0. \quad (3.6)$$

It should be noted that equality constraints of the form  $\mathbf{A}\mathbf{x} = \mathbf{b}$  can be additionally considered in SDPs.

In most applications, the decision variables  $x_i$  are not expressed in a scalar fashion as in (3.5) but as matrix variables, e.g., using the matrices  $\mathbf{M}_1 \in \mathbb{C}^{m \times m}$  and  $\mathbf{M}_2 \in \mathbb{H}^m$  and the unknown  $\mathbf{X} \in \mathbb{S}^m$

$$\mathbf{M}_1^T \mathbf{X} + \mathbf{X} \mathbf{M}_1 + \mathbf{M}_2 > 0. \quad (3.7)$$

Since the elements of  $\mathbf{X}$  appear affinely in (3.7), it can easily be transformed to (3.5). Two (or more) LMIs  $\mathbf{M}_a(\mathbf{x}) > 0$  and  $\mathbf{M}_b(\mathbf{x}) > 0$  can be combined to one LMI:

$$\begin{bmatrix} \mathbf{M}_a(\mathbf{x}) & \mathbf{0} \\ \mathbf{0} & \mathbf{M}_b(\mathbf{x}) \end{bmatrix} > 0. \quad (3.8)$$

See e.g., Boyd et al. (1994), Dettori (2001) and Scherer and Weiland (2004) for further details on LMIs.

Interior-point methods allow to efficiently solve SDPs (Boyd et al., 1994). Popular solvers, e.g., SDPT3 (Toh, Todd, and Tütüncü, 1999) and SeDuMi (Sturm, 1999), are freely available and have an interface to the LMI parser YALMIP (Löfberg, 2004). Consequently, SDPs have become a powerful tool in control engineering practice.

## 3.2 Parametric Uncertain and LPV Models

In many applications, the considered system can be reasonably described by an LTI model at fixed operating points but the system changes its dynamics w.r.t. model parameters. For example, in aeroelasticity, the model depends on the flight speed and on the air density etc. While these time-varying parameters are measurable, other parameters can be unknown or uncertain, e.g., the mass distribution. A suitable approach to deal with such systems are parametric uncertain and LPV models which are introduced below.

### 3.2.1 Linear Parameter Varying Models

Before the class of LPV models is introduced, differentiable parameter vector trajectories with bounded rates are defined. The parameter vector is assumed to be a continuously differentiable function of time  $\rho: \mathbb{R}_+ \rightarrow \mathcal{P}$ . Admissible trajectories are restricted, based on physical considerations, to a compact subset  $\mathcal{P} \subset \mathbb{R}^{n_\rho}$ . In addition, the parameter rates of variation  $\dot{\rho}$  are assumed to lie within the hyperrectangle  $\dot{\mathcal{P}}$  defined by

$$\dot{\mathcal{P}} := \{ \dot{\rho} \mid |\dot{\rho}_i| \leq \nu_i \ \forall i \in \{1, \dots, n_\rho\} \}, \quad (3.9)$$

where  $\nu_i$  are nonnegative numbers. The set of all admissible trajectories is defined as

$$\mathcal{A} := \{ \rho \mid \rho(t) \in \mathcal{P}, \dot{\rho}(t) \in \dot{\mathcal{P}} \ \forall t \geq 0 \}. \quad (3.10)$$

**Definition 3.5** (Wu, 1995; Wu et al., 1996): The continuous matrix functions  $A: \mathcal{P} \rightarrow \mathbb{R}^{n_x \times n_x}$ ,  $B: \mathcal{P} \rightarrow \mathbb{R}^{n_x \times n_d}$ ,  $C: \mathcal{P} \rightarrow \mathbb{R}^{n_e \times n_x}$ ,  $D: \mathcal{P} \rightarrow \mathbb{R}^{n_e \times n_d}$ , the state vector  $x: \mathbb{R}_+ \rightarrow \mathbb{R}^{n_x}$ , the initial condition  $x_0 \in \mathbb{R}^{n_x}$ , the input vector  $d: \mathbb{R}_+ \rightarrow \mathbb{R}^{n_d}$ , and the output vector  $e: \mathbb{R}_+ \rightarrow \mathbb{R}^{n_e}$  define the linear parameter varying (LPV) system  $P_\rho$  by

$$\dot{x} = A(\rho)x + B(\rho)d, \quad x(0) = x_0 \quad (3.11a)$$

$$e = C(\rho)x + D(\rho)d. \quad (3.11b)$$

The parameter vector  $\rho$  – also referred to as scheduling signal – can be considered as an additional input, which alters the plant dynamics. For LPV systems, the parameter vector is usually assumed to be measurable. On the contrary, parametric uncertainties are – by definition – unknown. While this distinction is important for controller synthesis, it hardly affects the analysis of a system. Artificial parameters which are functions of the states can be used to describe soft nonlinearities. In this case, the model is called quasi LPV.

The derivation of LPV models from nonlinear systems is intensively studied in the literature. Marcos and Balas (2004) compare three classical approaches to generate LPV models: Jacobian based linearization, state transformation, and function substitution. Optimization based approaches to generate optimal LPV models are proposed by Pfifer and Hecker (2010) and Pfifer (2013).

### 3.2.2 Linear Fractional Representation of LPV Models

The symbolic dependence of LPV models on the scheduling parameter complicates the numerical processing of the model or makes it even impossible. As a remedy, the LPV model can be written in its LFR. This representation is based on the linear fractional transformation (LFT) which is defined below.

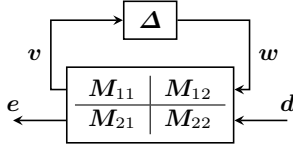


**Figure 3.1:** Graphical interpretation of the upper LFT. The loop is closed by  $\Delta$ .

**Definition 3.6** (Hecker, 2006): Using the partitioned matrix

$$M = \begin{bmatrix} M_{11} & M_{12} \\ M_{21} & M_{22} \end{bmatrix} \in \mathbb{C}^{(n_1+n_2) \times (m_1+m_2)} \quad (3.12)$$

and the matrix  $\Delta \in \mathbb{C}^{m_1 \times n_1}$ , the upper linear fractional transformation (LFT) is defined as

$$\mathcal{F}_u(M, \Delta) = M_{22} + M_{21}\Delta(\mathbf{I} - M_{11}\Delta)^{-1}M_{12}, \quad (3.13)$$

provided that the inverse  $(\mathbf{I} - M_{11}\Delta)^{-1}$  exists.

A graphical interpretation of the upper LFT is presented in Figure 3.1. The LFT describes the relation between  $d$  and  $e$  in the closed loop. This corresponds to

$$v = M_{11}w + M_{12}d \quad (3.14a)$$

$$e = M_{21}w + M_{22}d \quad (3.14b)$$

$$w = \Delta v. \quad (3.14c)$$

If the LPV system (3.11) depends only rationally on the parameters  $\rho$ , it can be written in its linear fractional representation (LFR)

$$\dot{x} = A_{11}x + A_{12}w + B_1d, \quad x(0) = x_0 \quad (3.15a)$$

$$v = A_{21}x + A_{22}w + B_2d \quad (3.15b)$$

$$e = C_1 x + C_2 w + D d \quad (3.15c)$$

$$w = \Delta(\rho)v, \quad (3.15d)$$

(see Dettori and Scherer, 1998; Dettori, 2001). The operator  $\Delta$  is also referred to as delta block or  $\Delta$ -block of an LFR. Without loss of generality, the  $\Delta$ -block can be written as the linear function

$$\Delta(\rho) = \text{diag}(\rho_1 \mathbf{I}_{s_1}, \dots, \rho_{n_\rho} \mathbf{I}_{s_{n_\rho}}), \quad (3.16)$$

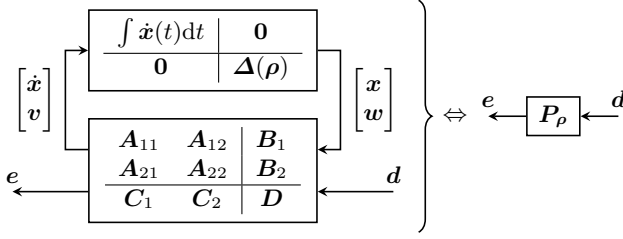


**Figure 3.2:** LFR of an LPV model.

where  $\text{diag}(\cdot)$  is the block diagonal concatenation of its arguments. Every parameter  $\rho_i$  is repeated  $s_i$  times in the  $\Delta$ -block. The LFR order is defined as

$$n_{\text{LFR}} = \sum_{i=1}^{n_\rho} s_i. \quad (3.17)$$

The parameters  $\rho_i$  are typically scaled s.t.  $\rho_i \in [-1, 1]$ . The equivalence of an LPV system and its LFR is illustrated in [Figure 3.2](#).

As already mentioned, the transformation of the LPV system (3.11) into its LFR is straightforward if the system depends only rationally on the parameters ([Hecker, 2006](#)). However, the LFR is not unique and the resulting LFR order may vary largely. [Hecker \(2006\)](#) proposes several numerical and symbolic LFR order reduction algorithms, which allow for an automated generation of low order LFRs. These approaches are available in the *Enhanced LFR-Toolbox for MATLAB* ([Hecker, Varga, and Magni, 2005](#)). If the parameter dependence is non-rational, the functional dependence must be approximated by rational functions. An optimization based approach for doing this is presented in [Pfifer and Hecker \(2010\)](#) and [Pfifer \(2013\)](#).

### 3.3 Analysis of LTI and LPV Systems

In the following section, the stability analysis of LPV systems is discussed and two important performance measures are introduced. The first one is the well-known worst case energy-to-energy gain or – mathematically speaking – the induced  $\mathcal{L}_2 \rightarrow \mathcal{L}_2$  norm. The second one is the induced  $\mathcal{L}_2 \rightarrow \mathcal{L}_\infty$  norm, which corresponds to the worst case energy-to-peak gain.

#### 3.3.1 Stability

The stability analysis of LTI systems is simple and can be performed by an eigenvalue analysis of the system matrix  $\mathbf{A}$ . On the contrary, the stability proof of

the autonomous LPV system

$$P_\rho: \dot{x} = A(\rho)x \quad (3.18)$$

is more sophisticated. It is common practice to do this by means of Lyapunov theory. To that end, a positive definite parameter dependent Lyapunov matrix  $\mathbf{X}: \mathcal{P} \rightarrow \mathbb{S}^{n_x}$  is introduced and the Lyapunov function

$$V(x, \rho) := x^T \mathbf{X}(\rho)x \quad (3.19)$$

is defined. From  $\mathbf{X} > 0$  follows that  $V(x, \rho) > 0$  for all  $x \neq 0$  and  $V(0, \rho) = 0$ . Using arguments from Lyapunov theory, it can be shown that the LPV system is exponentially stable if the derivative of  $V$  w.r.t. the time

$$\dot{V}(x, \rho, \dot{\rho}) = x^T \left( A(\rho)^T \mathbf{X}(\rho) + \mathbf{X}(\rho) A(\rho) + \sum_{i=1}^{n_\rho} \frac{\partial \mathbf{X}(\rho)}{\partial \rho_i} \dot{\rho}_i \right) x \quad (3.20)$$

is negative definite, i.e.,  $\dot{V}(x, \rho, \dot{\rho}) < 0$  for all  $x \neq 0$  and  $\dot{V}(0, \rho, \dot{\rho}) = 0$ .

Note that (3.20) is eventually an algebraic inequality in the variables  $x$ ,  $\rho$ , and  $\dot{\rho}$  which is independent of the time. This allows to consider  $\rho$  and  $\dot{\rho}$  independently. To emphasize this, the auxiliary variables  $p \in \mathcal{P}$  and  $q \in \dot{\mathcal{P}}$  are introduced and substituted in (3.19) and (3.20) for  $\rho$  and  $\dot{\rho}$ , respectively. Additionally, the shortcut  $\partial \mathbf{X}: \mathcal{P} \times \dot{\mathcal{P}} \rightarrow \mathbb{S}^{n_x}$

$$\partial \mathbf{X}(p, q) := \sum_{i=1}^{n_\rho} \frac{\partial \mathbf{X}(p)}{\partial p_i} q_i \quad (3.21)$$

is defined. Using this shortcut and (3.19) and (3.20), the following theorem provides a sufficient condition for the stability of LPV systems.

**Theorem 3.1:** *The LPV system (3.18) is exponentially stable if there exists a continuous differentiable Lyapunov matrix function  $\mathbf{X}: \mathcal{P} \rightarrow \mathbb{S}^{n_x}$  s.t. for all  $(p, q) \in \mathcal{P} \times \dot{\mathcal{P}}$*

$$\mathbf{X}(p) > 0, \quad (3.22a)$$

$$A(p)^T \mathbf{X}(p) + \mathbf{X}(p) A(p) + \partial \mathbf{X}(p, q) < 0. \quad (3.22b)$$

**Proof:** The proof can be found in Wu et al. (1996, Lemma 3.2.1) and Dettori (2001, Theorem 24). ■

In case of an unbounded parameter rate  $q_i \rightarrow \infty$ , the term  $\frac{\partial \mathbf{X}(p)}{\partial p_i}$  must vanish in order to keep  $\partial \mathbf{X}(p, q)$  finite. Consequently,  $\mathbf{X}(p)$  has to be independent of parameters with unbounded rates. Theorem 3.1 is only a sufficient condition but its LTI counterpart provides a necessary and sufficient condition.

### 3.3.2 Worst Case Energy-to-Energy Gain

The worst case energy-to-energy gain is generally accepted as a performance measure for LPV systems (Wu et al., 1996; Pfifer, 2013; Saupe, 2013). Mathematically speaking, this gain is the induced  $\mathcal{L}_2 \rightarrow \mathcal{L}_2$  norm and is defined below.

**Definition 3.7** (Wu, 1995; Wu et al., 1996): The induced  $\mathcal{L}_2 \rightarrow \mathcal{L}_2$  norm of an LPV system  $P_\rho$  is defined as

$$\|P_\rho\|_{\mathcal{L}_2 \rightarrow \mathcal{L}_2} := \sup_{\substack{\rho \in \mathcal{A} \\ d \in \mathcal{L}_2 \setminus \{0\}}} \frac{\|e\|_{\mathcal{L}_2}}{\|d\|_{\mathcal{L}_2}}, \quad (3.23)$$

where a zero initial condition is assumed.

The well-known Bounded Real Lemma provides an LMI condition for the induced  $\mathcal{L}_2 \rightarrow \mathcal{L}_2$  norm of LPV systems.

**Theorem 3.2** (Bounded Real Lemma): *An LPV system  $P_\rho$  is exponentially stable and its induced  $\mathcal{L}_2$  norm  $\|P_\rho\|_{\mathcal{L}_2 \rightarrow \mathcal{L}_2}$  from  $d$  to  $e$  is smaller than a performance index  $\gamma$  if there exists a continuous differentiable Lyapunov matrix function  $X: \mathcal{P} \rightarrow \mathbb{S}^{n_x}$  s.t. for all  $(p, q) \in \mathcal{P} \times \dot{\mathcal{P}}$*

$$X(p) > 0, \quad (3.24a)$$

$$\begin{bmatrix} A(p)^T X(p) + X(p) A(p) + \partial X(p, q) & X(p) B(p) \\ B(p)^T X(p) & -I \end{bmatrix} + \frac{1}{\gamma^2} \begin{bmatrix} C(p)^T \\ D(p)^T \end{bmatrix} \begin{bmatrix} C(p) & D(p) \end{bmatrix} < 0. \quad (3.24b)$$

**Proof:** The proof can be found in Wu et al. (1996, Lemma 3.1.3) and Dettori (2001, Theorem 24). ■

The considerations regarding to the stability after Theorem 3.1 hold analogously for the worst case energy-to-peak gain. Note that for an LTI system  $P$ , the induced  $\mathcal{L}_2 \rightarrow \mathcal{L}_2$  norm corresponds to the  $\mathcal{H}_\infty$  norm of its transfer function  $P(s)$ .

### 3.3.3 Worst Case Energy-to-Peak Gain

Another performance measure is the worst case energy-to-peak gain or mathematically speaking the induced  $\mathcal{L}_2 \rightarrow \mathcal{L}_\infty$  norm. This norm is interesting for gust loads analysis because it enables to compute guaranteed upper bounds for the peaks of the model outputs.

**Definition 3.8** (Rotea, 1993; Dettori, 2001): The induced  $\mathcal{L}_2 \rightarrow \mathcal{L}_\infty$  norm for the LPV system  $P_\rho$  is defined as

$$\|P_\rho\|_{\mathcal{L}_2 \rightarrow \mathcal{L}_\infty} := \sup_{\substack{\rho \in \mathcal{A} \\ d \in \mathcal{L}_2 \setminus \{0\}}} \frac{\|e\|_{\mathcal{L}_\infty}}{\|d\|_{\mathcal{L}_2}}, \quad (3.25)$$

where a zero initial condition is assumed.

**Remark 3.1:** A necessary condition for a finite energy-to-peak gain is a zero feed-through matrix. To see that, consider the system  $d = e$  and the disturbance

$$d(t) = \begin{cases} \frac{1}{\sqrt{b}} & 0 \leq t \leq b \\ 0 & \text{otherwise.} \end{cases} \quad (3.26)$$

Obviously,  $\|d\|_{\mathcal{L}_2} = 1$  and  $\|e\|_{\mathcal{L}_\infty} = \frac{1}{\sqrt{b}}$ . Consequently, for  $b \rightarrow 0$  an infinite large peak can be reached with unit disturbance energy. For that reason,  $\mathbf{D} = \mathbf{0}$  is assumed in the following treatise.

Several possibilities for computing the worst case energy-to-peak gain of LPV and LTI systems are presented below.

### Induced $\mathcal{L}_2 \rightarrow \mathcal{L}_\infty$ Norm for LPV Systems

The following theorem gives an LMI characterization of the induced  $\mathcal{L}_2 \rightarrow \mathcal{L}_\infty$  norm.

**Theorem 3.3:** *An LPV system  $\mathbf{P}_\rho$  is exponentially stable and its induced  $\mathcal{L}_2 \rightarrow \mathcal{L}_\infty$  norm  $\|\mathbf{P}_\rho\|_{\mathcal{L}_2 \rightarrow \mathcal{L}_\infty}$  from  $\mathbf{d}$  to  $\mathbf{e}$  is smaller than a performance index  $\gamma$  if there exists a continuous differentiable Lyapunov matrix function  $\mathbf{X}: \mathcal{P} \rightarrow \mathbb{S}^{n_x}$  s.t. for all  $(\mathbf{p}, \mathbf{q}) \in \mathcal{P} \times \dot{\mathcal{P}}$*

$$\mathbf{X}(\mathbf{p}) > 0, \quad (3.27a)$$

$$\begin{bmatrix} \mathbf{A}(\mathbf{p})^\top \mathbf{X}(\mathbf{p}) + \mathbf{X}(\mathbf{p})\mathbf{A}(\mathbf{p}) + \partial \mathbf{X}(\mathbf{p}, \mathbf{q}) & \mathbf{X}(\mathbf{p})\mathbf{B}(\mathbf{p}) \\ \mathbf{B}(\mathbf{p})^\top \mathbf{X}(\mathbf{p}) & -\gamma \mathbf{I} \end{bmatrix} < 0, \quad (3.27b)$$

$$\begin{bmatrix} \mathbf{X}(\mathbf{p}) & \mathbf{C}(\mathbf{p})^\top \\ \mathbf{C}(\mathbf{p}) & \gamma \mathbf{I} \end{bmatrix} > 0. \quad (3.27c)$$

**Proof:** The following proof is an adaption of the LTI proof from [Dettori \(2001, Theorem 12\)](#). Since the LMIs (3.27) hold for all admissible parameter trajectories,  $\rho$  and  $\dot{\rho}$  can be substituted for  $\mathbf{p}$  and  $\mathbf{q}$ , respectively. This allows the definition of the storage function  $V: \mathbb{R}^{n_x} \times \mathcal{P} \rightarrow \mathbb{R}_+$

$$V(\mathbf{x}, \rho) := \mathbf{x}^\top \mathbf{X}(\rho) \mathbf{x}. \quad (3.28)$$

Adding a small perturbation  $\varepsilon > 0$  to (3.27b) yields the non-strict LMI<sup>2</sup>

$$\begin{bmatrix} \mathbf{A}(\rho)^\top \mathbf{X}(\rho) + \mathbf{X}(\rho)\mathbf{A}(\rho) + \partial \mathbf{X}(\rho, \dot{\rho}) & \mathbf{X}(\rho)\mathbf{B}(\rho) \\ \mathbf{B}(\rho)^\top \mathbf{X}(\rho) & -(1 - \varepsilon)\gamma \mathbf{I} \end{bmatrix} \leq 0. \quad (3.29)$$

---

<sup>2</sup>The perturbation is necessary to proof that the norm is smaller (and not only smaller or equal) than  $\gamma$ .

Left and right multiplication of (3.29) by  $[\mathbf{x}^T \quad \mathbf{d}^T]$  and its transpose, respectively, leads to the dissipation inequality

$$\frac{d}{dt} V(\mathbf{x}, \boldsymbol{\rho}) \leq (1 - \epsilon) \gamma \mathbf{d}^T \mathbf{d}. \quad (3.30)$$

The case  $\mathbf{d} = \mathbf{0}$  leads directly to [Theorem 3.1](#) and hence exponential stability can be proved by the same arguments. Using  $\mathbf{x}(0) = \mathbf{0}$ , integration w.r.t.  $t$  yields

$$V(\mathbf{x}(T), \boldsymbol{\rho}(T)) \leq (1 - \epsilon) \gamma \int_0^T \mathbf{d}(t)^T \mathbf{d}(t) dt. \quad (3.31)$$

Next, using a Schur complement (see [Lemma A.4](#)) on (3.27c) yields

$$\mathbf{X}(\boldsymbol{\rho}) - \frac{1}{\gamma} \mathbf{C}(\boldsymbol{\rho})^T \mathbf{C}(\boldsymbol{\rho}) > 0. \quad (3.32)$$

Left and right multiplication by  $\mathbf{x}^T$  and  $\mathbf{x}$ , respectively, results in

$$\frac{1}{\gamma} \mathbf{e}^T \mathbf{e} = \frac{1}{\gamma} \mathbf{x}^T \mathbf{C}(\boldsymbol{\rho})^T \mathbf{C}(\boldsymbol{\rho}) \mathbf{x} \leq \mathbf{x}^T \mathbf{X}(\boldsymbol{\rho}) \mathbf{x} = V(\mathbf{x}, \boldsymbol{\rho}). \quad (3.33)$$

The evaluation of (3.33) at  $t = T$  and the combination with (3.31) gives

$$\frac{1}{\gamma} \mathbf{e}(T)^T \mathbf{e}(T) \leq (1 - \epsilon) \gamma \int_0^T \mathbf{d}(t)^T \mathbf{d}(t) dt. \quad (3.34)$$

Taking the supremum w.r.t.  $T$  results finally in

$$\|\mathbf{e}\|_{\mathcal{L}_\infty} < \gamma \|\mathbf{d}\|_{\mathcal{L}_2}, \quad (3.35)$$

which completes the proof. ■

### Induced $\mathcal{L}_2 \rightarrow \mathcal{L}_\infty$ Norm of LTI Systems in the Time Domain

In case of an LTI system, [Theorem 3.3](#) can be further simplified to allow a more efficient computation.

**Theorem 3.4:** *The induced  $\mathcal{L}_2 \rightarrow \mathcal{L}_\infty$  norm of the stable LTI system  $\mathbf{P}$  is*

$$\|\mathbf{P}\|_{\mathcal{L}_2 \rightarrow \mathcal{L}_\infty} = \sqrt{\max(\text{eig}(\mathbf{C} \mathbf{W}_c \mathbf{C}^T))} \quad (3.36)$$

where the controllability Gramian matrix  $\mathbf{W}_c$  is the solution of the Lyapunov equation

$$\mathbf{A} \mathbf{W}_c + \mathbf{W}_c \mathbf{A}^T + \mathbf{B} \mathbf{B}^T = 0. \quad (3.37)$$

**Proof:** Only a sketch of the proof is presented. For the sufficiency part, the proof for the  $\mathcal{H}_2$  LMI characterization in [Dettori \(2001, Theorem 10\)](#) can easily be adapted. This step consists in showing that

$$\gamma = \sqrt{\max(\text{eig}(\mathbf{C}\mathbf{W}_c\mathbf{C}^T))} \quad \text{and} \quad (3.38a)$$

$$\mathbf{X} = \gamma \mathbf{W}_c^{-1} \quad (3.38b)$$

satisfy (3.27). The necessity part results from the fact that a corresponding worst case excitation can be explicitly computed (see [Corollary 3.5](#)). ■

### Worst Case Excitation

In many applications, not only the norm but also the worst case excitation is of interest. From controllability analysis (see [Dullerud and Paganini, 2000](#)), it is known that the optimal input

$$\mathbf{d}(t) = \mathbf{B}^T \mathbf{e}^{\mathbf{A}^T t} \mathbf{W}_c^{-1} \mathbf{x}_0 \quad (3.39)$$

steers an LTI system with minimum energy from the initial state  $\mathbf{x}(t \rightarrow -\infty) = 0$  to the final state  $\mathbf{x}(0) = \mathbf{x}_0$ . The required energy is

$$\|\mathbf{d}\|_{\mathcal{L}_2} = \sqrt{\mathbf{x}_0^T \mathbf{W}_c^{-1} \mathbf{x}_0}. \quad (3.40)$$

Consequently, all states which can be reached with unit energy lie on the ellipsoid defined by

$$\varepsilon(\mathbf{W}_c^{-1}, 1) = \{\mathbf{x} \mid \mathbf{x}^T \mathbf{W}_c^{-1} \mathbf{x} = 1\}. \quad (3.41)$$

Further, all states which create an output satisfying  $\|\mathbf{e}\|_{\mathcal{L}_\infty} = \|\mathbf{P}\|_{\mathcal{L}_2 \rightarrow \mathcal{L}_\infty}$  lie on the ellipsoid

$$\varepsilon(\mathbf{C}\mathbf{C}^T, \|\mathbf{P}\|_{\mathcal{L}_2 \rightarrow \mathcal{L}_\infty}) = \{\mathbf{x} \mid \mathbf{x}^T \mathbf{C}^T \mathbf{C} \mathbf{x} = \|\mathbf{P}\|_{\mathcal{L}_2 \rightarrow \mathcal{L}_\infty}^2\}. \quad (3.42)$$

The state corresponding to the worst case  $\mathbf{x}_{\text{wc}}$  is the intersection of those two concentric ellipsoids. Note that this state vector is in general not unique. However, in order to find an  $\mathbf{x}_{\text{wc}}$ , an arbitrary  $\bar{\mathbf{x}}_{\text{wc}}$  with

$$\bar{\mathbf{x}}_{\text{wc}} \in \ker(\|\mathbf{P}\|_{\mathcal{L}_2 \rightarrow \mathcal{L}_\infty}^{-2} \mathbf{C}\mathbf{C}^T - \mathbf{W}_c^{-1}) \quad (3.43)$$

is chosen, where  $\ker(\cdot)$  is the kernel (or null space) of its argument. From  $\bar{\mathbf{x}}_{\text{wc}}$ , a worst case state vector can be computed as

$$\mathbf{x}_{\text{wc}} = \bar{\mathbf{x}}_{\text{wc}} / \sqrt{\bar{\mathbf{x}}_{\text{wc}}^T \mathbf{W}_c^{-1} \bar{\mathbf{x}}_{\text{wc}}}. \quad (3.44)$$

Using (3.39), the worst case excitation is

$$\mathbf{d}_{\text{wc}}(t) = \mathbf{B}^T \mathbf{e}^{\mathbf{A}^T t} \mathbf{W}_c^{-1} \mathbf{x}_{\text{wc}}. \quad (3.45)$$

This result is summarized in the following corollary.

**Corollary 3.5:** *The worst case excitation in terms of the energy-to-peak gain is*

$$\mathbf{d}_{wc}(t) = \mathbf{B}^T \mathbf{e}^{\mathbf{A}^T t} \mathbf{W}_c^{-1} \mathbf{x}_{wc}, \quad (3.46)$$

where the worst case state is computed using [Equations \(3.43\) and \(3.44\)](#).

**Example 3.1:** A graphical interpretation of the proceeding corollary is depicted in [Figure 3.3](#). The considered LTI system  $\mathbf{P}$  is

$$\begin{aligned} \dot{\mathbf{x}} &= \begin{bmatrix} -1 & -1 \\ 0 & -1 \end{bmatrix} \mathbf{x} + \begin{bmatrix} 1 \\ 1 \end{bmatrix} d \\ \mathbf{e} &= \frac{1}{4} \cdot \begin{bmatrix} 2 & 0 \\ 1 & -2 \end{bmatrix} \mathbf{x}. \end{aligned} \quad (3.47)$$

The controllability Gramian matrix of  $\mathbf{P}$  is

$$\mathbf{W}_c = \frac{1}{4} \cdot \begin{bmatrix} 1 & 1 \\ 1 & 2 \end{bmatrix} \quad (3.48)$$

and hence  $\|\mathbf{P}\|_{\mathcal{L}_2 \rightarrow \mathcal{L}_\infty} = 0.32$ .

### Induced $\mathcal{L}_2 \rightarrow \mathcal{L}_\infty$ Norm of LTI Systems in the Frequency Domain

As an alternative to [Theorem 3.4](#), the energy-to-peak gain can also be computed in the frequency domain. Recall the standard definition of the controllability Gramian:

$$\mathbf{W}_c = \int_0^\infty \mathbf{e}^{\mathbf{A}t} \mathbf{B} \mathbf{B}^T \mathbf{e}^{\mathbf{A}^T t} dt. \quad (3.49)$$

Consequently,

$$\mathbf{C} \mathbf{W}_c \mathbf{C}^T = \int_0^\infty \mathbf{C} \mathbf{e}^{\mathbf{A}t} \mathbf{B} \mathbf{B}^T \mathbf{e}^{\mathbf{A}^T t} \mathbf{C}^T dt \quad (3.50)$$

and by Parseval's Theorem

$$\mathbf{C} \mathbf{W}_c \mathbf{C}^T = \frac{1}{2\pi} \int_{-\infty}^\infty \mathbf{G}(j\omega) \mathbf{G}(j\omega)^* d\omega. \quad (3.51)$$

This leads to the following theorem.

**Theorem 3.6:** *The induced  $\mathcal{L}_2 \rightarrow \mathcal{L}_\infty$  norm of the stable LTI system  $\mathbf{P}$  is*

$$\|\mathbf{P}\|_{\mathcal{L}_2 \rightarrow \mathcal{L}_\infty} = \sqrt{\max \left( \text{eig} \left( \frac{1}{2\pi} \int_{-\infty}^\infty \mathbf{G}(j\omega) \mathbf{G}(j\omega)^* d\omega \right) \right)}. \quad (3.52)$$

**Proof:** The proof is obvious from [Theorem 3.4](#) and (3.51). ■

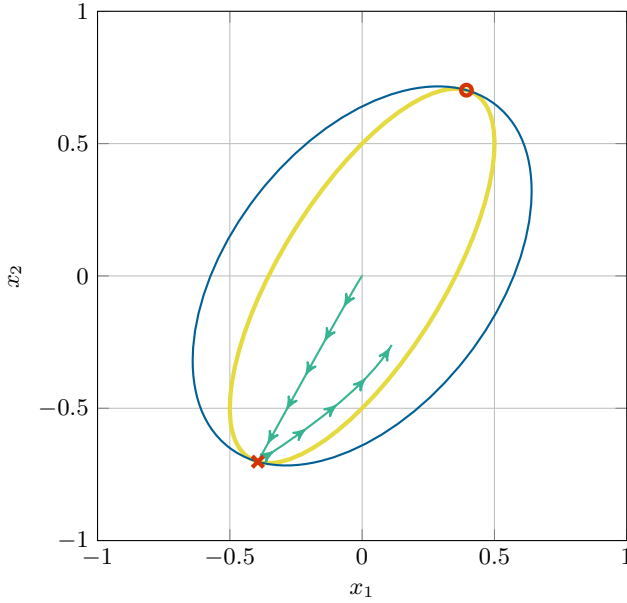


**Figure 3.3:** Graphical interpretation of [Example 3.1](#): The states which can be reached with unit energy are drawn by —. The states corresponding to  $\|e\|_{\mathcal{L}_\infty} = \|P\|_{\mathcal{L}_2 \rightarrow \mathcal{L}_\infty}$  are drawn by —. The worst case state vector  $\mathbf{x}_{wc}$  is the intersection of these two ellipses and is marked by  $\times$ . The worst case state trajectory is depicted by  $\rightarrow$ . A sign change of  $d$  and  $e$  results in the mirrored worst case state vector which is marked by  $\circ$ .

### Connection to the $\mathcal{H}_2$ Norm

Finally, the connection between the energy-to-peak gain and the  $\mathcal{H}_2$  norm is discussed. Recall first that the  $\mathcal{H}_2$  norm is defined as

$$\|P\|_{\mathcal{H}_2} := \sqrt{\text{trace} \left( \frac{1}{2\pi} \int_{-\infty}^{\infty} \mathbf{G}(j\omega) \mathbf{G}(j\omega)^* d\omega \right)} \quad (3.53)$$

where the trace of a matrix is the sum of the elements on its main diagonal. The relation between the induced  $\mathcal{L}_2 \rightarrow \mathcal{L}_\infty$  norm and the  $\mathcal{H}_2$  norm are clear if (3.52) is compared with (3.53). For that reason, the induced  $\mathcal{L}_2 \rightarrow \mathcal{L}_\infty$  norm is also referred to as generalized  $\mathcal{H}_2$  norm ([Rotea, 1993](#); [Dettori, 2001](#)). In the SISO case, the induced  $\mathcal{L}_2 \rightarrow \mathcal{L}_\infty$  norm and the  $\mathcal{H}_2$  norm are identical.

### 3.4 Techniques for Dealing with Infinite Dimensional LMIs

Based on [Theorems 3.2](#) and [3.3](#), optimization problems can be defined in order to compute an upper bound for worst case gains of LPV systems. For example, in case of the energy-to-peak gain, the resulting optimization problem reads as

$$\min_{\gamma, \mathbf{X}(\mathbf{p})} \gamma \quad \text{s.t. (3.27) holds for all } (\mathbf{p}, \mathbf{q}) \in \mathcal{P} \times \dot{\mathcal{P}}. \quad (3.54)$$

However, (3.54) is not yet an SDP. There are two issues which make the optimization problems numerically intractable. First, the decision variables can have an arbitrary functional dependence on the parameters. Second, the LMIs depend on the scheduling parameters so that they are infinite dimensional. Remedies from the literature for both problems are presented below. The remedies are explained at the examples of the energy-to-peak gain but they can easily be adapted for the energy-to-energy gain.

#### 3.4.1 Construction of Positive Definite Lyapunov Matrix Functions

The optimization problem (3.54) aims at finding a positive definite Lyapunov matrix function. Since functions can hardly be numerically determined, [Wu \(1995\)](#) and [Wu et al. \(1996\)](#) propose to assign  $n_f$  basis functions

$$\mathbf{X}(\mathbf{p}) := \sum_{i=1}^{n_f} f_i(\mathbf{p}) \mathbf{X}_i \quad \text{where } \mathbf{X}_i \in \mathbb{S}^{n_x}. \quad (3.55)$$

The new decision variables are the coefficients  $\mathbf{X}_i$  of the basis functions  $f_i$ .

More basis functions obviously increase the image space of  $\mathbf{X}$  and are hence supposed to reduce the conservatism. However, since every basis function increases the number of decision variables, this slows the optimization process down or may cause numerical problems. Consequently, the selection of the basis functions is an important step, which can have a crucial effect on the results. Unfortunately, there are hardly any guidelines in the literature how to do this but simple polynomials lead to good results in practice.

In order to ensure the positive definiteness of  $\mathbf{X}$ , the following theorem can be used.

**Theorem 3.7:** *If  $\mathbf{X}(\mathbf{p})$  is a continuous function of  $\mathbf{p} \in \mathcal{P}$  and if  $\mathbf{X}(\mathbf{0}) > 0$ , then the LMI*

$$\mathbf{A}(\mathbf{p})^T \mathbf{X}(\mathbf{p}) + \mathbf{X}(\mathbf{p}) \mathbf{A}(\mathbf{p}) + \partial \mathbf{X}(\mathbf{p}, \mathbf{q}) < 0 \quad \forall (\mathbf{p}, \mathbf{q}) \in \mathcal{P} \times \dot{\mathcal{P}} \quad (3.56)$$

*implies that  $\mathbf{X}(\mathbf{p}) > 0$  for all  $\mathbf{p} \in \mathcal{P}$ .*

**Proof:** The following proof by contradiction is adapted from [Pfifer \(2013\)](#) and [Dettori \(2001\)](#). Suppose that  $\mathbf{X}(\mathbf{0}) > \mathbf{0}$  and (3.56) hold but  $\mathbf{X}(\mathbf{p}) > \mathbf{0}$  does not. This implies the existence of a  $\bar{\mathbf{p}} \in \mathcal{P}$  such that  $\mathbf{X}(\bar{\mathbf{p}}) \not> \mathbf{0}$ . Consider a continuous trajectory  $\boldsymbol{\rho}: [0, 1] \rightarrow \mathcal{P}$  with  $\boldsymbol{\rho}(0) = \mathbf{0}$  and  $\boldsymbol{\rho}(1) = \bar{\mathbf{p}}$ . This allows to define the function  $\underline{\lambda}: [0, 1] \rightarrow \mathbb{R}$  by

$$\underline{\lambda}(t) = \min(\text{eig}(\mathbf{X}(\boldsymbol{\rho}(t)))) \quad (3.57)$$

which represents the smallest eigenvalue of  $\mathbf{X}(\boldsymbol{\rho}(t))$ . Due to the continuity of  $\mathbf{X}(\boldsymbol{\rho}(t))$ ,  $\underline{\lambda}(t)$  is also continuous. The positive definiteness of  $\mathbf{X}(\boldsymbol{\rho}(0))$  implies  $\underline{\lambda}(0) > 0$  and the indefiniteness of  $\mathbf{X}(\boldsymbol{\rho}(1))$  implies  $\underline{\lambda}(1) \leq 0$ . In combination with the continuity of  $\underline{\lambda}(t)$ , there must exist a  $\tilde{t} \in [0, 1]$  such that  $\underline{\lambda}(\tilde{t}) = 0$ . Consequently,  $\mathbf{X}(\boldsymbol{\rho}(\tilde{t}))$  has an eigenvalue at zero and this implies the existence of an eigenvector  $\tilde{\mathbf{x}}$  which satisfies  $\mathbf{X}(\boldsymbol{\rho}(\tilde{t}))\tilde{\mathbf{x}} = \mathbf{0}$ .

Evaluate (3.56) at  $\mathbf{p} = \boldsymbol{\rho}(\tilde{t})$  and  $\mathbf{q} = \mathbf{0}$ . Left and right multiplication by  $\tilde{\mathbf{x}}^T$  and  $\tilde{\mathbf{x}}$ , respectively, leads to

$$\tilde{\mathbf{x}}^T \mathbf{A}(\boldsymbol{\rho}(\tilde{t}))^T \underbrace{\mathbf{X}(\boldsymbol{\rho}(\tilde{t}))\tilde{\mathbf{x}}}_{=\mathbf{0}} + \underbrace{\tilde{\mathbf{x}}^T \mathbf{X}(\boldsymbol{\rho}(\tilde{t}))}_{=\mathbf{0}} \mathbf{A}(\boldsymbol{\rho}(\tilde{t}))\tilde{\mathbf{x}} < 0. \quad (3.58)$$

This contradicts the assumption and concludes the proof. ■

[Theorem 3.7](#) is used by [Dettori \(2001\)](#) and [Pfifer \(2013\)](#) in the context of stability analysis of LPV systems but it can also be used for robust performance. The negative definiteness of a matrix requires that any upper left square submatrix is negative definite. In case of the worst case energy-to-peak gain, the upper left block of (3.27b) corresponds directly to (3.56). For the energy-to-energy gain, the upper left block of (3.24b) can be transformed to

$$\mathbf{A}(\boldsymbol{\rho})^T \mathbf{X}(\mathbf{p}) + \mathbf{X}(\mathbf{p}) \mathbf{A}(\mathbf{p}) + \partial \mathbf{X}(\mathbf{p}, \mathbf{q}) < -\frac{1}{\gamma^2} \underbrace{\mathbf{C}(\mathbf{p})^T \mathbf{C}(\mathbf{p})}_{\geq 0} < 0. \quad (3.59)$$

Hence, [Theorems 3.2](#) and [3.3](#) imply (3.56) and consequently [Theorem 3.7](#) can be applied in order to simplify the resulting optimization problems.

### 3.4.2 Approximation Based on Gridding the Parameter Space

One way to circumvent infinite dimensional LMIs is introduced by [Wu \(1995\)](#) and [Wu et al. \(1996\)](#) and is based on gridding the parameter space. This means that the constraints are only enforced on a finite subset  $\mathcal{P}_{\text{grid}} \subset \mathcal{P}$ . Since  $\dot{\mathcal{P}}$  is a polytope and the parameter  $\mathbf{q} \in \dot{\mathcal{P}}$  enters the constraints only affinely, it is sufficient to check the constraints only at the vertices  $\dot{\mathcal{P}}_0$ , see [Proposition A.3](#). Note that  $\dot{\mathcal{P}}_0$  is a finite set. The gridding approach is thus based on an approximation of the original parameter space  $\mathcal{P} \times \dot{\mathcal{P}}$  by  $\mathcal{P}_{\text{grid}} \times \dot{\mathcal{P}}_0$ . This leads in combination with [Theorem 3.7](#) to the following algorithm.

**Algorithm 3.1:** An approximation of the upper bound for the  $\mathcal{L}_2 \rightarrow \mathcal{L}_\infty$  norm of an LPV system is determined by assigning  $n_f$  continuous basis functions

$$\mathbf{X}(\mathbf{p}) := \sum_{i=1}^{n_f} f_i(\mathbf{p}) \mathbf{X}_i \quad \text{where } \mathbf{X}_i \in \mathbb{S}^{n_x} \quad (3.60)$$

and by solving the SDP

$$\|\mathbf{P}_\rho\|_{\mathcal{L}_2 \rightarrow \mathcal{L}_\infty} \leq \min_{\gamma, \mathbf{X}_i} \gamma \quad \text{s.t.} \quad (3.61)$$

$$\mathbf{X}(\mathbf{0}) > 0, \quad (3.61a)$$

and for all  $(\mathbf{p}, \mathbf{q}) \in \mathcal{P}_{\text{grid}} \times \dot{\mathcal{P}}_0$

$$\begin{bmatrix} \mathbf{A}(\mathbf{p})^\top \mathbf{X}(\mathbf{p}) + \mathbf{X}(\mathbf{p}) \mathbf{A}(\mathbf{p}) + \partial \mathbf{X}(\mathbf{p}, \mathbf{q}) & \mathbf{X}(\mathbf{p}) \mathbf{B}(\mathbf{p}) \\ \mathbf{B}(\mathbf{p})^\top \mathbf{X}(\mathbf{p}) & -\gamma \mathbf{I} \end{bmatrix} < 0, \quad (3.61b)$$

$$\begin{bmatrix} \mathbf{X}(\mathbf{p}) & \mathbf{C}(\mathbf{p})^\top \\ \mathbf{C}(\mathbf{p}) & \gamma \mathbf{I} \end{bmatrix} > 0. \quad (3.61c)$$

One advantage of the gridding approach is its simplicity. Further, arbitrary parameter spaces as well as arbitrary nonlinearities can be considered. The severest disadvantage is the loss of sufficiency. It is thus self-explanatory that the density of the grid must be carefully chosen. However, even in the  $\mu$ -framework, the analysis is often performed on a finite grid of frequency points. It is further possible to check the validity of the results on a second denser grid  $\bar{\mathcal{P}}_{\text{grid}}$ . Therefore, it is proposed in the literature (e.g. [Pfifer, 2013](#)) to optimize only the performance index on the denser grid while the original obtained Lyapunov matrix function is used. In this thesis on the contrary, this validation is cast into a simple eigenvalue problem. To that end, (3.27b) and (3.27c) are converted using Schur complements:

$$(3.27b) \Leftrightarrow \begin{cases} \underbrace{\mathbf{A}(\mathbf{p})^\top \mathbf{X}(\mathbf{p}) + \mathbf{X}(\mathbf{p}) \mathbf{A}(\mathbf{p}) + \partial \mathbf{X}(\mathbf{p}, \mathbf{q})}_{=:\Xi(\mathbf{p}, \mathbf{q})} < 0 \\ -\gamma \mathbf{I} - \mathbf{B}(\mathbf{p})^\top \mathbf{X}(\mathbf{p}) \Xi(\mathbf{p}, \mathbf{q})^{-1} \mathbf{X}(\mathbf{p}) \mathbf{B}(\mathbf{p}) < 0 \end{cases} \quad (3.62a)$$

$$(3.27c) \Leftrightarrow \begin{cases} \mathbf{X}(\mathbf{p}) > 0 \\ \gamma \mathbf{I} - \mathbf{C}(\mathbf{p}) \mathbf{X}(\mathbf{p})^{-1} \mathbf{C}(\mathbf{p})^\top > 0. \end{cases} \quad (3.62b)$$

In (3.62), the Lyapunov matrix function  $\mathbf{X}$  is assumed to be known from an initial analysis on a sparse grid. This allows to compute the performance index by solving eigenvalue problems as explained in [Algorithm 3.2](#).

**Algorithm 3.2:** In order to validate the original solution for the sparse grid  $\mathcal{P}_{\text{grid}}$  on a second much denser grid  $\bar{\mathcal{P}}_{\text{grid}}$ , check for every  $(\mathbf{p}, \mathbf{q}) \in \bar{\mathcal{P}}_{\text{grid}} \times \dot{\mathcal{P}}_0$  if

$$\min(\text{eig}(\mathbf{X}(\mathbf{p}))) > 0 \quad (3.63a)$$

$$\max(\text{eig}(\Xi(\mathbf{p}, \mathbf{q}))) < 0 \quad (3.63b)$$

and compute

$$\bar{\gamma}_1(\mathbf{p}, \mathbf{q}) = \max(\text{eig}(-\mathbf{B}(\mathbf{p})^T \mathbf{X}(\mathbf{p}) \Xi(\mathbf{p}, \mathbf{q})^{-1} \mathbf{X}(\mathbf{p}) \mathbf{B}(\mathbf{p}))) \quad (3.63c)$$

$$\bar{\gamma}_2(\mathbf{p}, \mathbf{q}) = \max(\text{eig}(\mathbf{C}(\mathbf{p}) \mathbf{X}(\mathbf{p})^{-1} \mathbf{C}(\mathbf{p})^T)) . \quad (3.63d)$$

The upper bound for the induced  $\mathcal{L}_2 \rightarrow \mathcal{L}_\infty$  norm on the denser grid is

$$\bar{\gamma} = \begin{cases} \max_{\mathbf{p}, \mathbf{q}}(\max(\bar{\gamma}_1(\mathbf{p}, \mathbf{q}), \bar{\gamma}_2(\mathbf{p}, \mathbf{q}))) & \text{if (3.63a) and (3.63b) hold} \\ \infty & \text{otherwise.} \end{cases} \quad (3.63e)$$

If the performance index increases only slightly, this indicates – but does not prove – the validity of the results. The advantage of this approach is that eigenvalues can be more efficiently determined than solving SDPs. Additionally, grid points  $\mathbf{p}$  with large  $\bar{\gamma}(\mathbf{p}, \mathbf{q})$  indicate where the grid for the original SDP has to be refined. Note finally that despite of [Theorem 3.7](#), the positive definiteness of  $\mathbf{X}(\mathbf{p})$  is checked at every grid point. The reason is that a rank deficiency of  $\mathbf{X}(\mathbf{p})$  might occur between two grid points.

### 3.4.3 Relaxation Based on Multi Convexity

The following relaxation is restricted to so-called polytopic LPV systems. These systems are characterized by an affine parameter dependence of the system matrices, e.g., for the state matrix

$$\mathbf{A}(\boldsymbol{\rho}) = \mathbf{A}_0 + \sum_{i=1}^{n_\rho} \rho_i \mathbf{A}_i . \quad (3.64)$$

Additionally, the parameter space  $\mathcal{P}$  is assumed to be a convex polytope, i.e.,  $\mathcal{P} = \text{conv}(\mathcal{P}_0)$ . If further an affine Lyapunov matrix function

$$\mathbf{X}(\mathbf{p}) = \mathbf{X}_0 + \sum_{i=1}^{n_\rho} p_i \mathbf{X}_i \quad \Rightarrow \quad \partial \mathbf{X}(\mathbf{p}, \mathbf{q}) = \sum_{i=1}^{n_\rho} q_i \mathbf{X}_i \quad (3.65)$$

is considered, the constraints [\(3.27a\)](#) and [\(3.27c\)](#) become affine in  $\mathbf{p}$ . Consequently, [Proposition A.3](#) can be applied and it is sufficient to enforce [\(3.27a\)](#) and [\(3.27c\)](#) only at  $\mathcal{P}_0$ . The LMI [\(3.27b\)](#), however, is a quadratic function of  $\mathbf{p}$ :

$$\mathbf{F}(\mathbf{p}, \mathbf{q}) = \sum_{i=0}^{n_\rho} \sum_{j=0}^{n_\rho} p_i p_j \begin{bmatrix} \mathbf{A}_i^T \mathbf{X}_j + \mathbf{X}_j \mathbf{A}_i & \mathbf{X}_j \mathbf{B}_i \\ \mathbf{B}_i^T \mathbf{X}_j & \gamma \mathbf{I} \end{bmatrix} + \sum_{k=0}^{n_\rho} q_k \begin{bmatrix} \mathbf{0} & \mathbf{X}_k \\ \mathbf{0} & \mathbf{0} \end{bmatrix} < 0, \quad (3.66)$$

where  $p_0 = 1$  is used to shorten the notation. In order to apply [Proposition A.3](#) also to (3.66), the function

$$f(\mathbf{p}, \mathbf{q}) = \mathbf{x}^T \mathbf{F}(\mathbf{p}, \mathbf{q}) \mathbf{x} \quad (3.67)$$

must be multi convex for any  $\mathbf{x} \neq \mathbf{0}$ . This is the case if

$$\frac{\partial^2}{\partial p_i^2} f(\mathbf{p}, \mathbf{q}) = 2\mathbf{x}^T \begin{bmatrix} \mathbf{A}_i^T \mathbf{X}_i + \mathbf{X}_i \mathbf{A}_i & \mathbf{X}_i \mathbf{B}_i \\ \mathbf{B}_i^T \mathbf{X}_i & \mathbf{0} \end{bmatrix} \mathbf{x} \geq 0 \quad (3.68)$$

for all  $i = 1, \dots, n_\rho$ . Consequently, the additional constraint

$$\begin{bmatrix} \mathbf{A}_i^T \mathbf{X}_i + \mathbf{X}_i \mathbf{A}_i & \mathbf{X}_i \mathbf{B}_i \\ \mathbf{B}_i^T \mathbf{X}_i & \mathbf{0} \end{bmatrix} \geq 0 \quad (3.69)$$

is imposed for all  $i = 1, \dots, n_\rho$ . Further details can be found in [Gahinet, Apkarian, and Chilali \(1996\)](#). The result is summarized in the following algorithm. Note that [Theorem 3.7](#) is additionally used for the first LMI.

**Algorithm 3.3:** An upper bound for the  $\mathcal{L}_2 \rightarrow \mathcal{L}_\infty$  norm of a polytopic LPV system is determined by solving the SDP

$$\|\mathbf{P}_\rho\|_{\mathcal{L}_2 \rightarrow \mathcal{L}_\infty} \leq \min_{\gamma, \mathbf{X}_i} \gamma \quad \text{s.t.} \quad (3.70)$$

$$\mathbf{X}(\mathbf{0}) > 0, \quad (3.70a)$$

and for all  $(\mathbf{p}, \mathbf{q}) \in \mathcal{P}_0 \times \dot{\mathcal{P}}_0$

$$\begin{bmatrix} \mathbf{A}(\mathbf{p})^T \mathbf{X}(\mathbf{p}) + \mathbf{X}(\mathbf{p}) \mathbf{A}(\mathbf{p}) + \partial \mathbf{X}(\mathbf{p}, \mathbf{q}) & \mathbf{X}(\mathbf{p}) \mathbf{B}(\mathbf{p}) \\ \mathbf{B}(\mathbf{p})^T \mathbf{X}(\mathbf{p}) & -\gamma \mathbf{I} \end{bmatrix} < 0, \quad (3.70b)$$

$$\begin{bmatrix} \mathbf{X}(\mathbf{p}) & \mathbf{C}(\mathbf{p})^T \\ \mathbf{C}(\mathbf{p}) & \gamma \mathbf{I} \end{bmatrix} > 0, \quad (3.70c)$$

and for  $i = 1, \dots, n_\rho$

$$\begin{bmatrix} \mathbf{A}_i^T \mathbf{X}_i + \mathbf{X}_i \mathbf{A}_i & \mathbf{X}_i \mathbf{B}_i \\ \mathbf{B}_i^T \mathbf{X}_i & \mathbf{0} \end{bmatrix} \geq 0. \quad (3.70d)$$

The drawback of the polytopic approach is that it is restricted to affine parameter dependent LPV systems. While every LPV system can be over-bounded by such a model, this approach is usually extremely conservative ([Wu, 1995](#)).

### 3.4.4 Relaxation Based on the Full Block S-Procedure

The last relaxation method requires that the LPV model is given in an LFR and is based on the Full Block S-Procedure (see [Scherer, 1997](#); [Scherer, 2001](#)).

**Theorem 3.8** (Full Block S-Procedure): *Consider the quadratic constraint*

$$\mathbf{F}(\mathbf{p})^T \mathbf{T} \mathbf{F}(\mathbf{p}) < 0, \quad (3.71)$$

where  $\mathbf{F}(\mathbf{p}) = \mathcal{F}_u(\mathbf{M}, \Delta(\mathbf{p}))$  (corresponding to [Definition 3.6](#)) and  $\mathbf{T} \in \mathbb{S}^{n_2}$ . [Equation \(3.71\)](#) holds if and only if there exists a general multiplier  $\Pi \in \mathbb{S}^{2n_1}$  s.t.

$$\begin{bmatrix} M_{11} & M_{12} \\ \mathbf{I} & \mathbf{0} \\ M_{21} & M_{22} \end{bmatrix}^T \left[ \begin{array}{c|c} \Pi & \mathbf{0} \\ \hline \mathbf{0} & T \end{array} \right] \begin{bmatrix} M_{11} & M_{12} \\ \mathbf{I} & \mathbf{0} \\ M_{21} & M_{22} \end{bmatrix} < 0 \quad (3.72)$$

and for all  $\mathbf{p} \in \mathcal{P}$

$$\begin{bmatrix} \mathbf{I} \\ \Delta(\mathbf{p}) \end{bmatrix}^T \Pi \begin{bmatrix} \mathbf{I} \\ \Delta(\mathbf{p}) \end{bmatrix} \geq 0. \quad (3.73)$$

**Proof:** A proof can be found in [Scherer \(2001\)](#). ■

### Structure of Multipliers

In order to relax the still infinite dimensional second constraint (3.73), the structure of the multiplier is restricted. Different types of multipliers can be found in the literature. They are all based on the structure

$$\Pi = \begin{bmatrix} \mathbf{Q} & \mathbf{S} \\ \mathbf{S}^T & \mathbf{R} \end{bmatrix}, \quad (3.74)$$

where  $\mathbf{Q}, \mathbf{R} \in \mathbb{S}^{n_1}$  and  $\mathbf{S} \in \mathbb{R}^{n_1 \times n_1}$ .

**Diagonal multipliers** Recall first the diagonal structure of the  $\Delta$ -block (see (3.16)) where every parameter  $p_i$  is repeated  $s_i$  times and scaled to  $|p_i| \leq 1$ . A similar structure is applied to the multiplier  $\Pi$  which leads to

$$\mathbf{R} = \text{diag}(\mathbf{R}_1, \dots, \mathbf{R}_{n_\rho}) \leq 0, \quad \text{where } \mathbf{R}_i \in \mathbb{S}^{s_i}, \quad (3.75a)$$

$$\mathbf{Q} = -\mathbf{R}, \quad (3.75b)$$

$$\mathbf{S} = \text{diag}(\mathbf{S}_1, \dots, \mathbf{S}_{n_\rho}), \quad \text{where } \mathbf{S}_i = -\mathbf{S}_i^T \in \mathbb{R}^{s_i \times s_i}. \quad (3.75c)$$

This renders the constraint (3.73) into a block diagonal like structure of which one block is

$$\begin{bmatrix} \mathbf{I} \\ p_i \mathbf{I} \end{bmatrix}^T \begin{bmatrix} -\mathbf{R}_i & \mathbf{S}_i \\ \mathbf{S}_i^T & \mathbf{R}_i \end{bmatrix} \begin{bmatrix} \mathbf{I} \\ p_i \mathbf{I} \end{bmatrix} = \underbrace{(p_i^2 - 1)}_{\leq 0} \underbrace{\mathbf{R}_i}_{\leq 0} + p_i \underbrace{(\mathbf{S}_i + \mathbf{S}_i^T)}_{=0} \geq 0. \quad (3.76)$$

Consequently, the second constraint (3.73) is always fulfilled. A special case is  $\mathbf{S} = \mathbf{0}$ , where the number of decision variables is reduced on the price of more conservatism. Finally, this type of multiplier is related with the *DG* scales in the  $\mu$ -analysis framework. ([Dettori, 2001](#); [Pfifer, 2013](#))

**Full block multipliers** The full block multipliers require no structure of  $\Delta \in \mathcal{P}$  but it is assumed that the  $\mathcal{P}$  is a convex polytope, i.e.,  $\mathcal{P} = \text{conv}(\mathcal{P}_0)$ . Using the partitioned matrix (3.73), the constraint (3.74) becomes

$$\mathbf{F}(\Delta) := \mathbf{Q} + \mathbf{S}^T \Delta + \Delta^T \mathbf{S} + \Delta^T \mathbf{R} \Delta \geq 0. \quad (3.77)$$

Similar to the multi convexity approach, the idea is to check the definiteness of  $\mathbf{F}(\Delta)$  only on the vertices  $\mathcal{P}_0$ . Therefore, by Proposition A.3,  $\mathbf{x}^T \mathbf{F}(\Delta) \mathbf{x}$  must be a concave function which is the case if  $\mathbf{R} \leq 0$ . Hence, constraint (3.73) can be transformed to

$$\begin{bmatrix} \mathbf{I} \\ \Delta(\mathbf{p}) \end{bmatrix}^T \begin{bmatrix} \mathbf{Q} & \mathbf{S} \\ \mathbf{S}^T & \mathbf{R} \end{bmatrix} \begin{bmatrix} \mathbf{I} \\ \Delta(\mathbf{p}) \end{bmatrix} \geq 0 \quad \forall \mathbf{p} \in \mathcal{P}_0 \quad \text{and} \quad \mathbf{R} \leq 0. \quad (3.78)$$

The diagonal multipliers are a subset of the full block multipliers. Hence, the latter are supposed to be less conservative. However, they introduce more additional decision variables and increase the number of LMIs. (Dettori, 2001; Pfifer, 2013)

**Further multipliers** Other types of multipliers can be found in e.g., Pfifer (2013). It should be also noted that different types of multipliers can be combined.

### LFR of Theorem 3.3

In order to use the Full Block S-Procedure, it is necessary to write Equation (3.27) as a quadratic constraint. To that end, the Lyapunov matrix function is written as

$$\mathbf{X}(\mathbf{p}) = \mathbf{F}_X(\mathbf{p})^T \mathbf{T}_X \mathbf{F}_X(\mathbf{p}). \quad (3.79)$$

where the basis functions are defined by  $\mathbf{F}_X(\mathbf{p})$  and their coefficients are collected in  $\mathbf{T}_X \in \mathbb{S}$ . For example a quadratic basis function w.r.t. one parameter  $p$  can be written as

$$\mathbf{X}(p) = \mathbf{X}_0 + p\mathbf{X}_1 + p^2\mathbf{X}_2 = \begin{bmatrix} \mathbf{I} \\ p\mathbf{I} \end{bmatrix}^T \begin{bmatrix} \mathbf{X}_0 & \frac{1}{2}\mathbf{X}_1 \\ \frac{1}{2}\mathbf{X}_1 & \mathbf{X}_2 \end{bmatrix} \begin{bmatrix} \mathbf{I} \\ p\mathbf{I} \end{bmatrix}, \quad (3.80)$$

where  $\mathbf{X}_0, \mathbf{X}_1, \mathbf{X}_2 \in \mathbb{S}$ . Further, the differential operator is

$$\partial \mathbf{X}(\mathbf{p}, \mathbf{q}) = \begin{bmatrix} \partial \mathbf{F}_X(\mathbf{p}, \mathbf{q}) \\ \mathbf{F}_X(\mathbf{p}) \end{bmatrix}^T \begin{bmatrix} \mathbf{0} & \mathbf{T}_X \\ \mathbf{T}_X & \mathbf{0} \end{bmatrix} \begin{bmatrix} \partial \mathbf{F}_X(\mathbf{p}, \mathbf{q}) \\ \mathbf{F}_X(\mathbf{p}) \end{bmatrix}. \quad (3.81)$$

This allows to write (3.27) as

$$\mathbf{F}_X(\mathbf{p})^T \mathbf{T}_X \mathbf{F}_X(\mathbf{p}) > 0 \quad (3.82a)$$

$$\underbrace{F_{AB}(\mathbf{p}, \mathbf{q})^\top}_{=:T_{AB}} \left[ \begin{array}{cc|c} \mathbf{0} & T_X & \mathbf{0} \\ T_X & \mathbf{0} & \mathbf{0} \\ \hline \mathbf{0} & \mathbf{0} & -\gamma \mathbf{I} \end{array} \right] \underbrace{\left[ \begin{array}{cc} F_X(\mathbf{p}) & \mathbf{0} \\ F_X(\mathbf{p})\mathbf{A}(\mathbf{p}) + \partial F_X(\mathbf{p}) & \mathbf{B}(\mathbf{p}) \\ \hline \mathbf{0} & \mathbf{I} \end{array} \right]}_{=:F_{AB}(\mathbf{p}, \mathbf{q})} < 0, \quad (3.82b)$$

$$F_C(\mathbf{p})^\top \underbrace{\left[ \begin{array}{ccc|c} T_X & \mathbf{0} & \mathbf{0} & \mathbf{0} \\ \hline \mathbf{0} & \gamma \mathbf{I} & \mathbf{0} & \mathbf{0} \\ \mathbf{0} & \mathbf{0} & \mathbf{0} & \mathbf{I} \\ \hline \mathbf{0} & \mathbf{0} & \mathbf{I} & \mathbf{0} \end{array} \right]}_{=:T_C} \underbrace{\left[ \begin{array}{cc} F_X(\mathbf{p}) & \mathbf{0} \\ \hline \mathbf{0} & \mathbf{I} \\ C(\mathbf{p}) & \mathbf{0} \\ \hline \mathbf{0} & \mathbf{I} \end{array} \right]}_{=:F_C(\mathbf{p})} > 0. \quad (3.82c)$$

Note that the matrix functions  $F_X(\mathbf{p})$ ,  $F_{AB}(\mathbf{p}, \mathbf{q})$ , and  $F_C(\mathbf{p})$  must be given as LFRs:

$$F_X(\mathbf{p}) = \mathcal{F}_u(M_X, \Delta_X(\mathbf{p})) \quad (3.83a)$$

$$F_{AB}(\mathbf{p}, \mathbf{q}) = \mathcal{F}_u(M_{AB}, \Delta_{AB}(\mathbf{p}, \mathbf{q})) \quad (3.83b)$$

$$F_C(\mathbf{p}) = \mathcal{F}_u(M_C, \Delta_C(\mathbf{p})), \quad (3.83c)$$

where the three matrices  $M_X$ ,  $M_{AB}$ , and  $M_C$  are partitioned according to [Definition 3.6](#).

Using these variables, the following algorithm can be stated where [Theorem 3.7](#) is used for the first LMI.

**Algorithm 3.4:** An upper bound for the  $\mathcal{L}_2 \rightarrow \mathcal{L}_\infty$  norm of an LPV system given as an LFR is determined by solving the SDP

$$\|P_\rho\|_{\mathcal{L}_2 \rightarrow \mathcal{L}_\infty} \leq \min_{\mathbf{x}} \gamma \quad \text{s.t.} \quad (3.84)$$

$$\underbrace{M_{X22}^\top T_X M_{X22}}_{=:X(0)} > 0 \quad (3.84a)$$

$$\left[ \begin{array}{cc} M_{AB11} & M_{AB12} \\ \hline \mathbf{I} & \mathbf{0} \\ M_{AB21} & M_{AB22} \end{array} \right]^\top \left[ \begin{array}{c|c} \Pi_{AB} & \mathbf{0} \\ \hline \mathbf{0} & T_{AB} \end{array} \right] \left[ \begin{array}{cc} M_{AB11} & M_{AB12} \\ \hline \mathbf{I} & \mathbf{0} \\ M_{AB21} & M_{AB22} \end{array} \right] < 0 \quad (3.84b)$$

$$\left[ \begin{array}{cc} M_{C11} & M_{C12} \\ \hline \mathbf{I} & \mathbf{0} \\ M_{C21} & M_{C22} \end{array} \right]^\top \left[ \begin{array}{c|c} \Pi_C & \mathbf{0} \\ \hline \mathbf{0} & -T_C \end{array} \right] \left[ \begin{array}{cc} M_{C11} & M_{C12} \\ \hline \mathbf{I} & \mathbf{0} \\ M_{C21} & M_{C22} \end{array} \right] < 0 \quad (3.84c)$$

and for all  $(\mathbf{p}, \mathbf{q}) \in \mathcal{P}_0 \times \dot{\mathcal{P}}_0$

$$\left[ \begin{array}{c} \mathbf{I} \\ \Delta_{AB}(\mathbf{p}, \mathbf{q}) \end{array} \right]^\top \Pi_{AB} \left[ \begin{array}{c} \mathbf{I} \\ \Delta_{AB}(\mathbf{p}, \mathbf{q}) \end{array} \right] \geq 0, \quad (3.84d)$$

$$\begin{bmatrix} \mathbf{I} \\ \Delta_C(p) \end{bmatrix}^T \Pi_C \begin{bmatrix} \mathbf{I} \\ \Delta_C(p) \end{bmatrix} \geq 0. \quad (3.84e)$$

The decision variables  $\chi$  contain of the elements of  $\gamma$ ,  $\mathbf{T}_X$ ,  $\Pi_{AB}$ , and  $\Pi_C$ . Note that the structure from (3.75) or (3.78) has to be imposed on the multiplier  $\Pi_{AB}$  and  $\Pi_C$  in order to yield numerically tractable conditions.

The severest disadvantage of using the Full Block S-Procedure is the need for an LFR of the considered LPV system. In case of a non-rational functional dependence, the LPV system must be approximated first and the resulting LFR can be of high order. Another point is the number of additional decision variables. Especially for parameter dependent Lyapunov matrices of systems with many states, the  $\Delta$ -block grows rapidly. Since this introduces many additional decision variables, such problems become quickly intractable.

## 3.5 A Benchmark of Techniques for Infinite Dimensional LMIs

While the techniques introduced in the preceding section are well-known, there is a lack of a neutral comparison. This is assessed in the present section using the example of a simple aeroelastic system. The benchmark criteria are the conservatism and the computation time.

### 3.5.1 Model of the Aeroelastic System

The considered aeroelastic system, taken from [Bisplinghoff, Ashley, and Halfman \(1955\)](#), is illustrated in [Figure 3.4](#). The equations of motion are

$$\begin{bmatrix} m & m \cdot x_{cg} \\ m \cdot x_{cg} & I \end{bmatrix} \begin{bmatrix} \ddot{h} \\ \ddot{\alpha} \end{bmatrix} + \begin{bmatrix} k_h & 0 \\ 0 & k_\alpha \end{bmatrix} \begin{bmatrix} h \\ \alpha \end{bmatrix} = \begin{bmatrix} -L \\ \tau \end{bmatrix}, \quad (3.85)$$

where  $h$  denotes the vertical deflection and  $\alpha$  the pitch angle. The lift  $L$  and the pitching moment  $\tau$  are given by

$$\begin{bmatrix} -L \\ \tau \end{bmatrix} = \frac{1}{2} \rho U_\infty^2 \begin{bmatrix} \mathbf{Q}_{\text{eig}} & \mathbf{Q}_{\text{gust}} \end{bmatrix} \begin{bmatrix} h \\ \alpha \\ v_{\text{gust}} \end{bmatrix}. \quad (3.86)$$

The Theodorsen function  $\mathbf{Q}_{\text{eig}}(s)$  models the relation between the aerodynamic forces and the eigen movement. The Sears function  $\mathbf{Q}_{\text{gust}}(s)$  maps the vertical gust velocity  $v_{\text{gust}}$  on  $L$  and  $\tau$ . Both transfer functions are non-rational in the Laplace domain. In order to yield a state space realization, R. T. Jones' rational approximation is used. The functions depend on the free stream velocity  $U_\infty$ , the

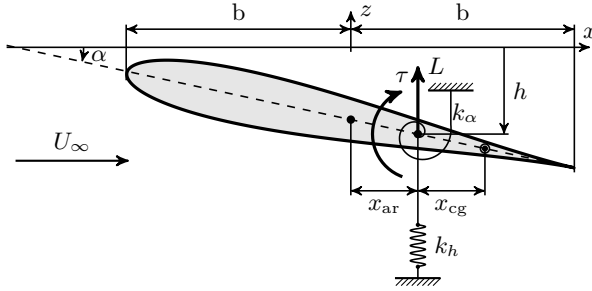


**Figure 3.4:** Aeroelastic system: The airfoil is flexibly restrained. The figure is adapted from [Bisplinghoff, Ashley, and Halfman \(1955\)](#).

**Table 3.1:** Model parameters: explanation and default values.

Sym.	Explanation	Value
$k_h$	translational stiffness	0.04
$k_\alpha$	rotational stiffness	0.25
$m$	mass	1.00
$I$	inertia	0.25
$x_{cg}$	location of the center of gravity	0.20
$U_\infty$	free stream velocity	0.70
$\rho$	air density	0.80
$b$	half chord length	1.00
$x_{ar}$	location of the aerodynamic reference axis	-0.20

half chord length  $b$ , and the location of the aerodynamic reference axis  $x_{ar}$ . The transfer functions  $\mathbf{Q}_{\text{eig}}$  and  $\mathbf{Q}_{\text{gust}}$  are explicitly given in [Bisplinghoff, Ashley, and Halfman \(1955\)](#). Default values and explanations for all model parameters are given in [Table 3.1](#).

In the considered scenarios, the model input is the gust velocity  $d = v_{\text{gust}}$  and the outputs are the spring forces

$$\mathbf{e} = \begin{bmatrix} k_h \cdot h \\ k_\alpha \cdot \alpha \end{bmatrix}. \quad (3.87)$$

Since the parameter dependence of the resulting state space model is highly involved, the state space matrices are compiled in [Appendix B.1](#). However, the model has eight states, namely  $h$ ,  $\alpha$ ,  $\dot{h}$ ,  $\dot{\alpha}$  and four aerodynamic lag states. Moreover, the feed through matrix is zero.

### 3.5.2 Numerical and Implementational Aspects

In order to reduce numerical problems, it is common practice to precondition the system before the analysis. The following steps are adapted from [Saupe \(2013\)](#) and [Skogestad and Postlethwaite \(1996\)](#)

1. The inputs are scaled with the maximum expected energy.
2. The outputs are scaled with the maximum LTI norm. To obtain this norm, the parameter space is gridded and the LTI norm is computed for every grid point. Note that the LTI norm computation is much less numerically sensitive than a robust analysis.
3. In order to balance the state space matrices, a time invariant state transformation is applied using Matlab's `ssbal`.

The analysis is performed using Matlab. The LMIs are coded using YALMIP ([Löfberg, 2004](#)) and the applied SDP solver is SDPT3 ([Toh, Todd, and Tütüncü, 1999](#)).

### 3.5.3 Assessment of the Multi Convexity Approach

The first assessment investigates the performance of the multi convexity approach. To that end, the translational stiffnesses  $k_h$  is considered to be uncertain, because this results directly in a polytopic model without any overbounding of the parameter space. The parameter range  $k_h \in [0.01, 0.30]$  and a zero parameter rate bound are chosen. A Bode diagram of the resulting system is depicted in [Figure 3.5](#) for ten values of  $k_h$ .

The parameter space is gridded with 100 equidistantly space values of  $k_h$ . The maximum norm over the corresponding LTI models is used to scale the system. This implies that a norm value of 1 is a lower bound for the results. An LFR based analysis (using diagonal multipliers) serves as a reference solution. The analysis results are compiled in [Table 3.2](#). In case of a constant Lyapunov matrix, the constraints for both norms are infeasible, independent of the relaxation method. Next, an affine Lyapunov matrix is considered. In case of the energy-to-energy gain, the multi convexity approach result is double as large as the LFR based result.<sup>3</sup> The latter is only slightly greater than 1 and hence not conservative. For the energy-to-peak gain, the conservatism of the multi convexity approach is comparable to the LFR based result for an affine Lyapunov matrix function. However, the LFR based result can be improved by choosing a quadratic Lyapunov matrix function which yields a non-conservative result. Consequently, the multi convexity approach leads here to an overestimation of the norm by 18%.

---

<sup>3</sup>In order to eliminate the possibilities of implementational and numerical problems, the multi convexity results are backed up using LMI Lab (see *Robust Control Toolbox: User's Guide* 2011), which yields the same result.

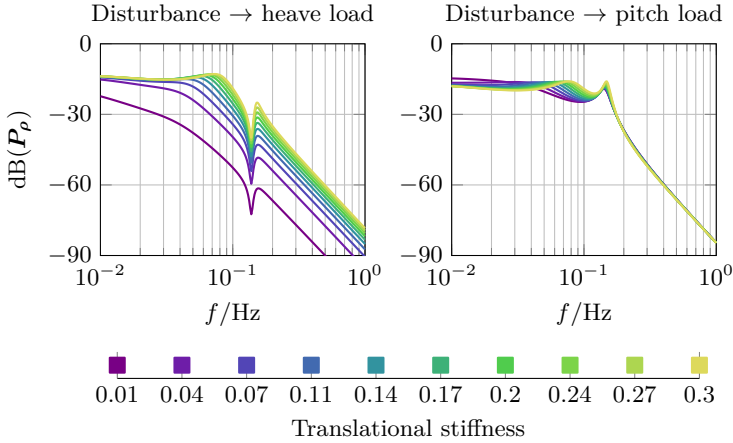


**Figure 3.5:** Bode diagram for the multi convexity assessment: The translational stiffness is indicated by the color.

**Table 3.2:** Results for the assessment of the multi convexity approach.

$X(p)$	Relaxation	Norm	
		$\ P_\rho\ _{\mathcal{L}_2 \rightarrow \mathcal{L}_2}$	$\ P_\rho\ _{\mathcal{L}_2 \rightarrow \mathcal{L}_\infty}$
Const.	polytopic/LFR-based	infeasible	
Affine	polytopic	2.159	1.179
Affine	LFR based (diag. multiplier)	1.053	1.162
Quad.	LFR based (diag. multiplier)	1.001	1.000

Although the considered model can be covered by a polytopic LPV model without any overbounding, the result for the energy-to-energy gain is extremely conservative. This can be caused only by the additional constraint (3.70d) and appears to be a systematic problem of this approach. In combination with the restriction to polytopic LPV models and affine Lyapunov matrix functions, this approach seems here to be unfavorable.

### 3.5.4 Assessment of Multipliers for the Full Block S-Procedure

In the second assessment, the effect of the multipliers for the Full Block S-Procedure is considered. To that end, the mass is assumed to be uncertain in the interval  $m \in [0.4, 1.5]$  and the free stream velocity in the range of  $U_\infty \in [0.5, 0.8]$ . The

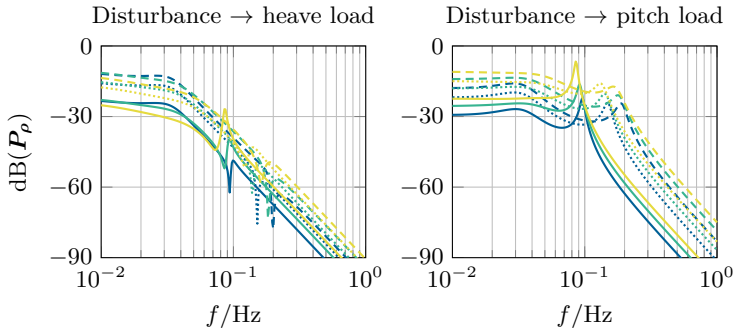


**Figure 3.6:** Bode diagram of the second to the fourth assessment:  $3 \times 3$  values of  $U_\infty$  and  $m$  are considered. The same color indicates the same velocity  $U_\infty$ .

**Table 3.3:** Results for the assessment of different multipliers. ( $\#\chi$  refers to the number of decision variables and  $\#\text{LMIs}$  to the number of LMIs.)

a) Energy-to-energy gain

Relaxation	Norm	Time	$\#\chi$	$\#\text{LMIs}$
diag multipl. / $\mathbf{X}(\mathbf{p})$	1.002	10 s	857	113
full block multipl. / $\mathbf{X}(\mathbf{p})$	1.002	67 s	2825	305
diag multipl. / $\mathbf{X}(\mathbf{0})$	1.002	8 s	729	81
full block multipl. / $\mathbf{X}(\mathbf{0})$	1.002	43 s	2297	209

b) Energy-to-peak gain

Relaxation	Norm	Time	$\#\chi$	$\#\text{LMIs}$
diag multipl. / $\mathbf{X}(\mathbf{p})$	1.162	9 s	985	155
full block multipl. / $\mathbf{X}(\mathbf{p})$	1.095	84 s	3353	411
diag multipl. / $\mathbf{X}(\mathbf{0})$	1.162	8 s	857	123
full block multipl. / $\mathbf{X}(\mathbf{0})$	1.095	59 s	2825	315

parameter rates are again set to zero. This leads to the  $\Delta$ -block  $\text{diag}(m\mathbf{I}_3, U_\infty\mathbf{I}_7)$ . The Bode diagram for the resulting model family is depicted in Figure 3.6 for three different values per uncertain parameter. Here, quadratic Lyapunov matrix functions are used. Additionally, the effect of the relaxation of the first LMI applying Theorem 3.7 is studied.

The analysis results are shown in Table 3.3. Regarding the energy-to-energy gain, all four methods obtain the same low conservative result. However, they differ distinctly in the computation time and the SDP problem size. The number of decision variables ( $\#\chi$ ) for the full block multipliers is more than three times greater than for the diagonal ones. The full block multipliers increase the LMI size ( $\#\text{LMIs}$ ) by a factor of 2.5. The increased problem size is reflected in the computation time which lasts more than 6.5 times longer. Using Theorem 3.7, which allows to consider only  $\mathbf{X}(\mathbf{0}) > 0$ , reduces  $\#\chi$  and  $\#\text{LMIs}$  by approx. 15 %. This results in a reduced computation time. Similar results are obtained for the energy-to-peak gain. The only difference is that the full block multipliers reduce the conservatism by 6 %.

Summarizing, it can be concluded that full block multipliers improve the results at the best only slightly. In combination with the increased problem size they are not beneficial for the considered example. On the contrary, the usage of Theorem 3.7 has proved to be useful.

### 3.5.5 Assessment of the Gridding Approach

The gridding based approximation is assessed below. The model of the preceding subsection is used and a grid of  $51 \times 51$  points is considered. During an initial analysis only  $6 \times 6$  points are used. Afterwards the results are validated on the full grid (cf. Algorithm 3.2), which leads to a set of invalid grid points. A subset of these points are next additionally used for a second analysis, which is again validated on the full grid. A grid of  $11 \times 11$  points serves as a reference solution. All grids are illustrated in Figure 3.7.

The results are compiled in Table 3.4. First of all, both approaches lead to same results, which are consistent with the LFR based ones. The results of the two step analysis are valid on all  $51 \times 51$  points although the SDP is solved only on 41 and 39 grid points. Since the adaption of the grid allows to consider much less grid points, the analysis can be sped up compared to directly using a dense grid.

For the energy-to-peak gain, the results are finally backed up by a  $\mu$ -analysis. To that end, the function `wcgain` of the robust control toolbox (*Robust Control Toolbox: User's Guide* 2011) is used. Using the default parameters of `wcgain` results in an upper bound which is smaller than the maximum LTI norm. In order to yield consistent results, it was necessary to use 2000 logarithmically spaced frequency points between 0.01 Hz and 1.00 Hz. The reason for the sensitivity toward the frequency grid is the distinct resonance of the system. See also Figure 3.8.

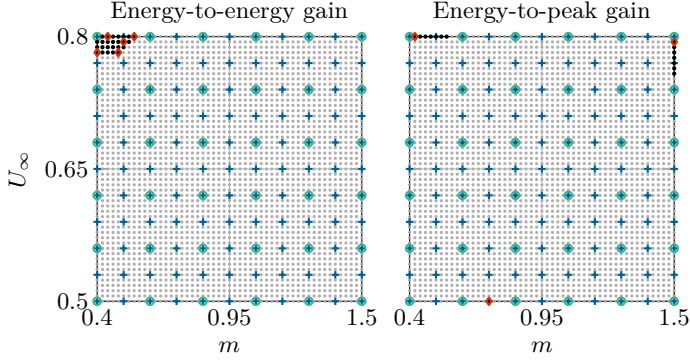


**Figure 3.7:** Grid points for the third assessment: The parameter space is gridded by  $51 \times 51$  points ( $\circ$ ).  $6 \times 6$  points ( $\circ$ ) are used for an initial analysis. The other points are used for validation, where the invalid points ( $\circ$ ) are obtained. A subset of these points ( $\diamond$ ) are finally used for a second analysis. A second grid ( $+$ ) of the size  $11 \times 11$  serves as reference.

**Table 3.4:** Results for the assessment of the gridding approach. ( $\#\chi$  refers to the number of decision variables and  $\#\text{LMIs}$  to the number of LMIs.)

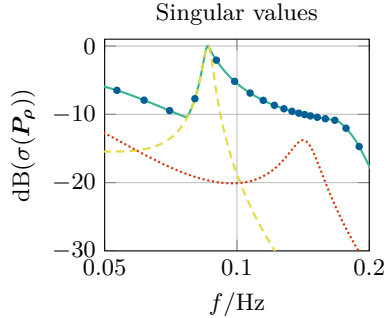
a) Energy-to-energy gain

Grid points	Norm	Time	$\#\chi$	$\#\text{LMIs}$
$11 \times 11$ (fixed)	1.002	13 s	217	1097
41/2601 (adaptive)	1.002	6 s	217	377
wcgain (default freq. grid)	0.797	150 s	N/A	N/A
wcgain (customized freq. grid)	1.002	3618 s	N/A	N/A

b) Energy-to-peak gain

Grid points	Norm	Time	$\#\chi$	$\#\text{LMIs}$
$11 \times 11$ (fixed)	1.000	19 s	217	2307
39/2601 (adaptive)	1.000	9 s	217	749

**Figure 3.8:** Worst case gain analysis for the third assessment: The results using the default options of `wcgain` (•) are smaller than the maximum LTI norm. A customized frequency grid (—) leads to consistent results. Additionally, a singular value plot of the nominal model (·····) and of the worst case model (---) are depicted.



### 3.5.6 Assessment of Different Lyapunov Basis Functions

The last assessment treats different Lyapunov basis functions at the example of the two preceding sections. The following basis functions are considered:

$$\mathbf{X}_{\text{aff}}(\mathbf{p}) = \mathbf{X}_0 + U_\infty \mathbf{X}_{11} + m \mathbf{X}_{12} \quad (3.88a)$$

$$\mathbf{X}_{\text{quad}}(\mathbf{p}) = \mathbf{X}_{\text{aff}}(\mathbf{p}) + U_\infty^2 \mathbf{X}_{21} + m^2 \mathbf{X}_{22} + U_\infty m \mathbf{X}_{23} \quad (3.88b)$$

$$\mathbf{X}_{\text{cub}}(\mathbf{p}) = \mathbf{X}_{\text{quad}}(\mathbf{p}) + U_\infty^3 \mathbf{X}_{31} + m^3 \mathbf{X}_{32} + U_\infty^2 m \mathbf{X}_{33} + U_\infty m^2 \mathbf{X}_{34} \quad (3.88c)$$

The SDPs for a constant  $\mathbf{X}(\mathbf{p})$  and for functions depending on only one parameter are infeasible. The free stream velocity  $U_\infty$  is considered as a time varying parameter. The rate bounds  $\dot{U}_\infty \in [-0.08\nu, 0.08\nu]$  with  $\nu \in \{0.0, 0.25, \dots, 1.0\}$  are used.

The results are depicted in Figure 3.9. While the norm values differ only slightly for small parameter rate bounds, they differ greatly otherwise. For increased rate bounds, higher order basis functions yield less conservative results. Note that an affine basis function in combination with a high rate bound leads to an infeasible SDP. The results for the quadratic and the cubic basis function differ only for the maximum rate bound in case of the energy-to-energy gain.

Finally, the relaxation method is revisited. The gridding approach leads always to the smallest results. At an increased rate bound, the LFR based results start to be more conservative. The overestimation using full block multipliers is smaller than for diagonal ones. However, while the SDP for the diagonal multipliers can be solved in less than a minute, the computation using the full block multipliers lasts up to thirty minutes. Further, the full block multipliers cause numerical problems in many cases. A third order basis function for the energy-to-peak gain leads even to an “out of memory” error.<sup>4</sup> The reason is that a third order basis function doubles the LFR size of  $\mathbf{X}(\mathbf{p})$ . Because  $\mathbf{X}(\mathbf{p})$  appears in every LMI, the overall LFR size is almost doubled and consequently the multiplier size is greatly increased.

<sup>4</sup>The used desktop computer is equipped with 12 GB RAM.

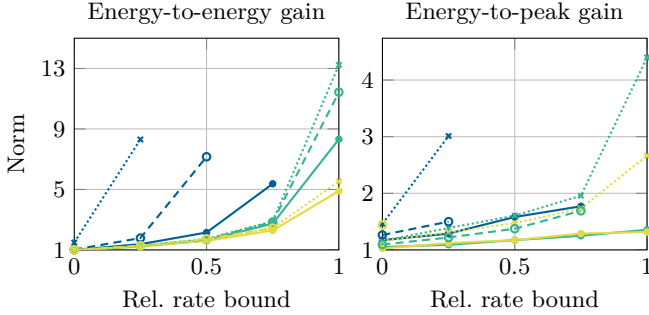


**Figure 3.9:** Results of the fourth assessment: The induced system norms are depicted w.r.t. the relative rate bound. The colors indicate the Lyapunov basis function and  $\bullet$  represents an affine function,  $\circ$  a quadratic function, and  $\circ$  a cubic function. In case of a grid based approximation, a solid line  $\bullet$  is used. In case of the Full Block S-Procedure, the line styles  $\cdots$  and  $\cdots$  refer to diagonal and full block multipliers, respectively. Missing points indicate that the corresponding SDP could not be solved.

### 3.5.7 Conclusions

The most important observation is that the LFR based and the gridding based analysis yields comparable results. On the contrary, the polytopic approach is – independent of any model overbounding during the modeling – very conservative for the considered examples.

Since the LFR based analysis provides a guaranteed upper bound, it is convenient to use this approach provided that an LFR model exists. Referring to the different multipliers, the theoretical superiority of full block multipliers over diagonal ones is proved at few examples. However, while the reduced conservatism is small, severe numerical problems are introduced and the computation lasts 5 to 50 times longer. Consequently, diagonal multipliers are the first choice and full block ones can be considered as a fall-back alternative.

In case that no LFR model is given or the LFR order is very high, the gridding approach is a reasonable option. As already mentioned, this approach yields comparable results. Due to the two step analysis, the SDP can be solved on a sparse grid while the validity is ensured on a dense grid. The results are hence supposed to be reliable.

The last important result is that a parameter dependent Lyapunov matrix function allows to distinctly reduce the conservatism of the analysis results. Note that this observation holds for both the gridding approach and the LFR based relaxation.

## 4 Analysis of Uncertain LPV Systems using IQCs

While parameter dependence and many “soft” nonlinearities can be described using LPV models, “hard” nonlinearities such as saturations and dead zones cannot be reasonably covered. These nonlinearities can be involved by integral quadratic constraints (IQCs). To that end, the system is represented by a feedback interconnection of an LPV model  $P_\rho$  and a nonlinear or an uncertain block  $\Delta$  (see Figure 4.1). The input/output behavior of  $\Delta$  is then described by constraints which can be incorporated in the robust performance analysis. In the present thesis, the focus lies on constraints for the saturation nonlinearity which are later used for the worst case analysis of a saturated gust load alleviation system.

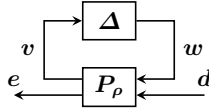


**Figure 4.1:** Feedback interconnection of an LPV model with a nonlinear block.

The chapter starts with an introduction to IQCs in Section 4.1. IQCs are defined and a list of important IQCs is provided. In Section 4.2 it is shown how uncertain LPV models can be described and analyzed using IQCs. LMI constraints which bounds the worst case energy-to-energy gain and the worst case energy-to-peak gain are given. It is further shown how the conservatism can be reduced by means of a local analysis. Finally, in Section 4.3, an aeroelastic system in combination with a saturated gust load alleviation controller is considered as an examples in order to examine the influence of different IQCs and saturation limits.

### 4.1 Integral Quadratic Constraints

#### 4.1.1 Definition and Properties

This section describes constraints for a causal operator  $\Delta$  which can be incorporated in the input/output analysis. The constraints are called IQCs and are taken from Megretski and Rantzer (1997). They can be expressed in the frequency domain as well as in the time domain. First, the definition in the frequency domain is given.

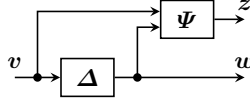


**Figure 4.2:** Graphical interpretation of an IQC.

**Definition 4.1** (Megretski and Rantzer, 1997): Let  $\Pi: \mathbb{R} \rightarrow \mathbb{H}^{(n_v+n_w)}$  be a measurable Hermitian-valued function. A bounded, causal operator  $\Delta: \mathcal{L}_{2e}^{n_v} \rightarrow \mathcal{L}_{2e}^{n_w}$  satisfies an IQC defined by the multiplier  $\Pi$  if the following inequality holds for all  $v \in \mathcal{L}_{2e}^{n_v}$ ,  $w = \Delta(v)$ , and  $T \geq 0$ :

$$\int_{-\infty}^{\infty} \begin{bmatrix} \hat{v}(j\omega) \\ \hat{w}(j\omega) \end{bmatrix}^* \Pi(j\omega) \begin{bmatrix} \hat{v}(j\omega) \\ \hat{w}(j\omega) \end{bmatrix} d\omega \geq 0. \quad (4.1)$$

In (4.1),  $\hat{v}$  and  $\hat{w}$  are Fourier transforms of  $v$  and  $w$ , respectively.

The multiplier  $\Pi$  can be factorized as

$$\Pi(j\omega) = \Psi(j\omega)^* M \Psi(j\omega) \quad (4.2)$$

which allows to connect the frequency domain formulation to a time domain formulation (see Megretski and Rantzer, 1997; Megretski, 2010; Seiler, 2015). This leads to a definition of an IQC in the time domain.

**Definition 4.2** (Pfifer and Seiler, 2014b): Let  $M \in \mathbb{S}^{n_z}$  and  $\Psi: \mathcal{L}_{2e}^{n_v+n_w} \rightarrow \mathcal{L}_{2e}^{n_z}$  be a stable linear system. A bounded, causal operator  $\Delta: \mathcal{L}_{2e}^{n_v} \rightarrow \mathcal{L}_{2e}^{n_w}$  satisfies an IQC defined by  $(\Psi, M)$  if the following inequality holds for all  $v \in \mathcal{L}_{2e}^{n_v}$ ,  $w = \Delta(v)$ , and  $T \geq 0$ :

$$\int_0^T z(t)^T M z(t) dt \geq 0, \quad (4.3)$$

where  $z$  is the output of the linear system  $\Psi$

$$\dot{x}_\Psi = A_\Psi x_\Psi + B_{\Psi 1} v + B_{\Psi 2} w, \quad x_\Psi(0) = 0 \quad (4.4a)$$

$$z = C_\Psi x_\Psi + D_{\Psi 1} v + D_{\Psi 2} w. \quad (4.4b)$$

The notation  $\Delta \in \text{IQC}(\Psi, M)$  is used if  $\Delta$  satisfies the IQC defined by  $(\Psi, M)$ .

Figure 4.2 provides a graphical interpretation of a time domain IQC. The input and output signals of  $\Delta$  are filtered through  $\Psi$ . If  $\Delta \in \text{IQC}(\Psi, M)$ , then the output signal  $z$  satisfies the (time domain) constraint in Equation (4.3) for any finite-horizon  $T \geq 0$ .

The following example, taken from Pfifer and Seiler (2014a), shows how a norm bounded uncertainty can be described by an IQC.

**Example 4.1:** Consider a causal (possibly nonlinear) SISO operator  $\Delta$  with an induced  $\mathcal{L}_2$  norm bound  $\|\Delta\|_{\mathcal{L}_2 \rightarrow \mathcal{L}_2} \leq b$ , i.e.,

$$\|w\|_{\mathcal{L}_2} \leq b \|v\|_{\mathcal{L}_2} \quad \forall v \in \mathcal{L}_2 \text{ and } w = \Delta(v) \quad (4.5)$$

or equivalently

$$\int_0^\infty w(t)^2 dt \leq b^2 \int_0^\infty v(t)^2 dt. \quad (4.6)$$

Next, it is shown that the former inequality holds in fact also for all finite time horizons. To that end, consider the truncated signal

$$\tilde{v}(t) = \begin{cases} v(t) & \text{if } t < T \\ 0 & \text{otherwise} \end{cases} \quad (4.7)$$

and the corresponding output  $\tilde{w} = \Delta(\tilde{v})$ . It is easy to see that the inequality

$$\int_0^T \tilde{w}(t)^2 dt \leq \int_0^\infty \tilde{w}(t)^2 dt \leq b^2 \int_0^\infty \tilde{v}(t)^2 dt = b^2 \int_0^T \tilde{v}(t)^2 dt \quad (4.8)$$

is true. Because  $\Delta$  is causal,  $\tilde{w}(t) = w(t)$  if  $t < T$  and hence

$$\int_0^T w(t)^2 dt \leq b^2 \int_0^T v(t)^2 dt \quad \text{for all } T \geq 0. \quad (4.9)$$

Finally, rewriting (4.9) leads to

$$\int_0^T \begin{bmatrix} v(t) \\ w(t) \end{bmatrix}^\top \begin{bmatrix} b^2 & 0 \\ 0 & -1 \end{bmatrix} \begin{bmatrix} v(t) \\ w(t) \end{bmatrix} dt \geq 0 \quad (4.10)$$

which is an IQC defined by  $\Psi = \mathbf{I}_2$  and  $\mathbf{M} = \begin{bmatrix} b^2 & 0 \\ 0 & -1 \end{bmatrix}$ .

It should be noted that there exists a technical detail for time domain IQCs which is discussed in the following remark.

**Remark 4.1:** A distinction between hard/complete and soft/conditional IQCs can be found in the literature (see e.g., Megretski and Rantzer, 1997; Seiler, 2015).

Definition 4.2 represents a hard IQC because the integral constraint (4.3) has to hold for all finite time intervals  $T \geq 0$ . On the contrary, for a soft IQC, it must hold only for the infinite time interval

$$\int_0^\infty z(t)^\top \mathbf{M} z(t) dt \geq 0. \quad (4.11)$$

Further, the factorization of a frequency domain IQC into a time domain IQC is not unique and there might exist a hard and a soft factorization for the same IQC. Numerical procedures for the hard factorization and conditions to check their existence can be found in Seiler (2015). However, this detail is not further considered in this thesis and there exists a hard factorization for all used frequency domain IQCs.

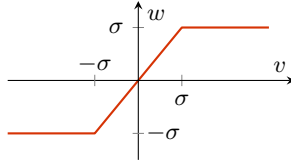


**Figure 4.3:** Saturation nonlinearity.

#### 4.1.2 IQCs for Saturation

The advantage of the IQC framework is that many properties of nonlinearities can be described by them. In order to arrive at low conservatism, an as accurate as possible description must be found for the considered nonlinearity. This can be achieved by combining several IQCs. To that end, [Megretski and Rantzer \(1997\)](#) present a lot of IQCs, which can be combined to describe a wide class of uncertainties/nonlinearities.

Here, a selection of IQCs for the saturation nonlinearity  $w = \text{sat}(v)$  defined by

$$w = \text{sat}(v) = \begin{cases} v & \text{if } |v| < \sigma \\ \text{sgn}(v) \cdot \sigma & \text{otherwise,} \end{cases} \quad (4.12)$$

is given. In (4.12),  $\sigma$  denotes the saturation limit. The saturation nonlinearity is depicted in [Figure 4.3](#). Three properties of saturation can be described by classical IQCs from [Megretski and Rantzer \(1997\)](#).

**Memoryless sector bounded nonlinearity:** [Figure 4.4](#) shows that the saturation lies in the sector defined by two lines with slope  $\alpha = 0$  and  $\beta = 1$ , denoted as sector  $[0, 1]$ . More general, a memoryless nonlinearity  $\phi: \mathbb{R} \rightarrow \mathbb{R}$  lies in a sector  $[\alpha, \beta]$  if

$$(w(t) - \alpha v(t))(\beta v(t) - w(t)) \geq 0 \quad (4.13)$$

holds for all  $v(t) \in \mathbb{R}$  and  $w(t) = \phi(v(t))$ . This can be equivalently expressed as

$$\begin{bmatrix} v(t) \\ w(t) \end{bmatrix}^T \begin{bmatrix} -2\alpha\beta & \alpha + \beta \\ \alpha + \beta & -2 \end{bmatrix} \begin{bmatrix} v(t) \\ w(t) \end{bmatrix} \geq 0. \quad (4.14)$$

Since (4.14) has to hold pointwise in time, it also holds when integrated over time

$$\int_0^T \begin{bmatrix} v(t) \\ w(t) \end{bmatrix}^T \begin{bmatrix} -2\alpha\beta & \alpha + \beta \\ \alpha + \beta & -2 \end{bmatrix} \begin{bmatrix} v(t) \\ w(t) \end{bmatrix} dt \geq 0 \quad (4.15)$$

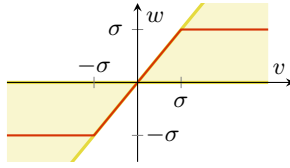


**Figure 4.4:** Sector constraint (yellow) for the saturation nonlinearity (red).

for any  $T \geq 0$ . Note that the converse is not true. Hence, the saturation function satisfies the IQC defined by

$$\Psi = \mathbf{I}_2 \quad \text{and} \quad M = \begin{bmatrix} -2\alpha\beta & \alpha + \beta \\ \alpha + \beta & -2 \end{bmatrix}, \quad (4.16)$$

with  $\alpha = 0$  and  $\beta = 1$ . Note that the sector IQC holds also for time varying, memoryless nonlinearities  $w(t) = \phi(v(t), t)$ .

**Popov IQC:** In order to capture the time invariance of saturation, the Popov IQC can be used. Consider a memoryless and time invariant nonlinearity  $w(t) = \phi(v(t))$ , where  $\phi: \mathbb{R} \rightarrow \mathbb{R}$  is a continuous function with  $v(0) = 0$ , and  $w$  and  $\dot{v}$  are square integrable. Then, the integral constraint

$$\int_0^\infty \dot{v}(t)w(t)dt = 0 \quad (4.17)$$

holds. Equation (4.17) corresponds to the frequency domain IQC defined by

$$\Pi(j\omega) = \pm \begin{bmatrix} 0 & j\omega \\ -j\omega & 0 \end{bmatrix}. \quad (4.18)$$

However, since  $\Pi$  is not bounded on the imaginary axis, it is not a proper IQC. As a remedy, the loop transformation from Figure 4.5 can be used. The operator  $\bar{\Delta}$  satisfies the IQC defined by

$$\bar{\Pi}(j\omega) = \pm \begin{bmatrix} 0 & \frac{j\omega}{1-j\omega} \\ \frac{-j\omega}{1+j\omega} & 0 \end{bmatrix}. \quad (4.19)$$

In order to revert the low-pass filter, the non-proper filter  $s + 1$  must be added to the interconnection (see Figure 4.5). This requires that the plant is strictly proper. The combination of the Popov IQC and of the sector constraint IQC yields the classical Popov criterion (Megretski and Rantzer, 1997).

**Zames-Falb IQC:** Finally, saturation is described by a monotonic, slope restricted, and odd function which is the last property satisfying a classical IQC.

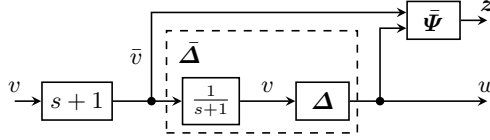


**Figure 4.5:** Popov IQC: loop transformation to yield a proper IQC.

Consider  $w(t) = \phi(v(t))$  where  $\phi: \mathbb{R} \rightarrow \mathbb{R}$  is a monotonic and odd function and its slope is bounded by  $\frac{\partial \phi}{\partial v} \in [0, k]$  for a constant  $k > 0$ . Then,  $v$  and  $w$  satisfy the IQC

$$\Pi(j\omega) = \begin{bmatrix} 0 & 1 + H(j\omega) \\ 1 + \overline{H(j\omega)} & -(2 + H(j\omega) + \overline{H(j\omega)})/k \end{bmatrix} \quad (4.20)$$

where  $H(s)$  is an arbitrary rational transfer function whose impulse response has an  $\mathcal{L}_1$  norm not larger than one. Details can be found in [Zames and Falb \(1968\)](#).

## 4.2 Analysis of Uncertain LPV Systems

In the following section, uncertain LPV models are introduced. The uncertainty is described by IQCs. This allows to specify a dissipation inequality which bounds the induced  $\mathcal{L}_2 \rightarrow \mathcal{L}_2$  or the  $\mathcal{L}_2 \rightarrow \mathcal{L}_\infty$  norm.

### 4.2.1 Uncertain LPV System

[Pfifer and Seiler \(2014a\)](#) propose to describe uncertain LPV system by the feedback interconnection of an LPV system  $P_\rho$  with a nonlinear and/or an uncertain operator  $\Delta$  (see [Figure 4.6a](#)). This corresponds to an upper LFT which is denoted as  $\mathcal{F}_u(P_\rho, \Delta)$ . In order to derive a tractable solution for computing system norms, the exact relation  $w = \Delta(v)$  is replaced by an IQC  $(\Psi, M)$  such that  $\Delta \in \text{IQC}(\Psi, M)$ . The resulting analysis interconnection is depicted in [Figure 4.6b](#) and its dynamics is ruled by

$$\dot{x} = A(\rho)x + B_1(\rho)w + B_2(\rho)d, \quad x(0) = x_0 \quad (4.21a)$$

$$z = C_1(\rho)x + D_{11}(\rho)w + D_{12}(\rho)d \quad (4.21b)$$

$$e = C_2(\rho)x + D_{21}(\rho)w + D_{22}(\rho)d \quad (4.21c)$$

$$w = \Delta(v). \quad (4.21d)$$

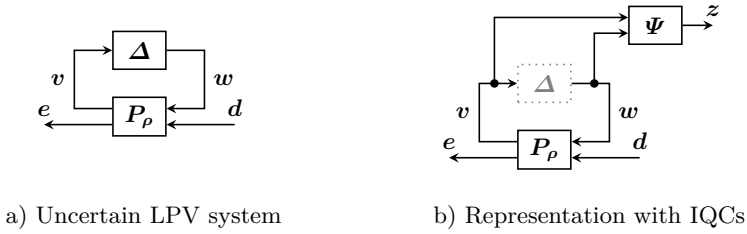


**Figure 4.6:** Uncertain LPV model with IQCs.

Note that  $\mathbf{x}$  includes the states of  $\mathbf{P}_\rho$  and  $\Psi$ . In the later analysis, the uncertainty  $\Delta$  is removed and  $\mathbf{w}$  is treated as an external signal s.t.

$$\int_0^T \mathbf{z}(t)^\top \mathbf{M} \mathbf{z}(t) dt \geq 0 \quad \forall T \geq 0. \quad (4.22)$$

The interconnection in Figure 4.6b can also be used to validate an IQC. The interconnection is excited with a finite test signal  $\mathbf{d}$ . If  $\Delta \in \text{IQC}(\Psi, \mathbf{M})$ , (4.22) must hold (Megretski and Rantzer, 1997).

It is finally assumed that the interconnection  $\mathcal{F}_u(\mathbf{P}_\rho, \Delta)$  is well-posed. In principle, this means that the mapping from  $\mathbf{d}$  to  $\mathbf{e}$  is causal. A precise definition is given below.

**Definition 4.3** (Seiler, 2015): The feedback interconnection of  $\mathbf{P}_\rho$  and  $\Delta$  is well-posed if for each  $\mathbf{d} \in \mathcal{L}_{2e}$  there exists a unique  $\mathbf{e} \in \mathcal{L}_{2e}$  such that the mapping from  $\mathbf{d}$  to  $\mathbf{e}$  is causal.

### 4.2.2 Worst Case Energy-to-Energy Gain

The induced  $\mathcal{L}_2 \rightarrow \mathcal{L}_2$  norm of uncertain LPV systems is defined similar to the nominal case.

**Definition 4.4** (Pfffer and Seiler, 2014a): The induced  $\mathcal{L}_2 \rightarrow \mathcal{L}_2$  norm for the uncertain LPV system  $\mathcal{F}_u(\mathbf{P}_\rho, \Delta)$  is defined as

$$\|\mathcal{F}_u(\mathbf{P}_\rho, \Delta)\|_{\mathcal{L}_2 \rightarrow \mathcal{L}_2} := \sup_{\Delta \in \text{IQC}(\Psi, \mathbf{M})} \sup_{\substack{\rho \in \mathcal{A} \\ \mathbf{d} \in \mathcal{L}_2 \setminus \{0\}}} \frac{\|\mathbf{e}\|_{\mathcal{L}_2}}{\|\mathbf{d}\|_{\mathcal{L}_2}}. \quad (4.23)$$

The following Bounded Real Lemma for LPV systems with IQCs is found in Pfffer and Seiler (2014a) and Pfffer and Seiler (2014b). It states a dissipation inequality which bounds the worst case energy-to-energy gain.

**Theorem 4.1:** *The induced  $\mathcal{L}_2$  norm from  $\mathbf{d}$  to  $\mathbf{e}$  of an uncertain LPV system  $\|\mathcal{F}_u(\mathbf{P}_\rho, \Delta)\|_{\mathcal{L}_2 \rightarrow \mathcal{L}_2}$  is smaller than a performance index  $\gamma$  if the interconnection is well posed for all  $\Delta \in \text{IQC}(\Psi, M)$  and if there exists a continuous differentiable Lyapunov matrix  $X: \mathcal{P} \rightarrow \mathbb{S}^{n_x}$  and a scalar  $\lambda > 0$  s.t. for all  $(\mathbf{p}, \mathbf{q}) \in \mathcal{P} \times \mathcal{P}$*

$$X(\mathbf{p}) > 0, \quad (4.24a)$$

$$\begin{aligned} & \begin{bmatrix} A(\rho)^T X(\mathbf{p}) + X(\mathbf{p}) A(\mathbf{p}) + \partial X(\mathbf{p}, \mathbf{q}) & X(\mathbf{p}) B_1(\rho) & X(\mathbf{p}) B_2(\mathbf{p}) \\ B_1(\mathbf{p})^T X(\mathbf{p}) & \mathbf{0} & \mathbf{0} \\ B_2(\mathbf{p})^T X(\mathbf{p}) & \mathbf{0} & -\mathbf{I} \end{bmatrix} \\ & + \lambda \begin{bmatrix} C_1(\mathbf{p})^T \\ D_{11}(\mathbf{p})^T \\ D_{12}(\mathbf{p})^T \end{bmatrix} M \begin{bmatrix} C_1(\mathbf{p}) & D_{11}(\mathbf{p}) & D_{12}(\mathbf{p}) \end{bmatrix} \\ & + \frac{1}{\gamma^2} \begin{bmatrix} C_2(\mathbf{p})^T \\ D_{21}(\mathbf{p})^T \\ D_{22}(\mathbf{p})^T \end{bmatrix} \begin{bmatrix} C_2(\mathbf{p}) & D_{21}(\mathbf{p}) & D_{22}(\mathbf{p}) \end{bmatrix} < 0. \end{aligned} \quad (4.24b)$$

**Proof:** A proof can be found in Pfifer and Seiler (2014b, Theorem 2). ■

It should be noted that exponential stability of the feedback interconnection  $\mathcal{F}_u(\mathbf{P}_\rho, \Delta)$  can hardly be checked. Instead, Megretski and Rantzer (1997) and Seiler (2015) propose to check the induced  $\mathcal{L}_2$  norm of the perturbed interconnection

$$\dot{\mathbf{x}} = A(\rho)\mathbf{x} + B(\rho)\mathbf{w}, \quad \mathbf{x}(0) = \mathbf{x}_0 \quad (4.25a)$$

$$\mathbf{v} = C(\rho)\mathbf{x} + D(\rho)\mathbf{w} + \mathbf{d}_1 \quad (4.25b)$$

$$\mathbf{w} = \Delta \mathbf{v} + \mathbf{d}_2 \quad (4.25c)$$

which is depicted in Figure 4.7. If the induced  $\mathcal{L}_2$  norm from  $\mathbf{d} = [\mathbf{d}_1^T \ \mathbf{d}_2^T]^T$  to  $\mathbf{e} = [\mathbf{v}^T \ \mathbf{w}^T]^T$  is finite, then the uncertain LPV system  $\mathcal{F}_u(\mathbf{P}_\rho, \Delta)$  is said to be input/output stable.

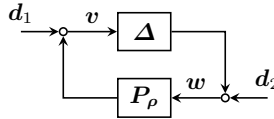


**Figure 4.7:** Perturbed uncertain LPV system for stability analysis.

### 4.2.3 Worst Case Energy-to-Peak Gain

As already mentioned, the worst case energy-to-peak gain is the more interesting norm for gust loads analysis. For an uncertain LPV system, this norm is defined as follows:

**Definition 4.5:** The induced  $\mathcal{L}_2 \rightarrow \mathcal{L}_\infty$  norm of an uncertain LPV system  $\mathcal{F}_u(\mathbf{P}_\rho, \Delta)$  is defined as

$$\|\mathcal{F}_u(\mathbf{P}_\rho, \Delta)\|_{\mathcal{L}_2 \rightarrow \mathcal{L}_\infty} := \sup_{\Delta \in \text{IQC}(\Psi, \mathbf{M})} \sup_{\substack{\rho \in \mathcal{A} \\ d \in \mathcal{L}_2 \setminus \{0\}}} \frac{\|e\|_{\mathcal{L}_\infty}}{\|d\|_{\mathcal{L}_2}}. \quad (4.26)$$

The following theorem is an adaption of [Theorem 4.1](#) and provides an LMI constraint for the induced  $\mathcal{L}_2 \rightarrow \mathcal{L}_\infty$  norm with IQCs.

**Theorem 4.2:** *The induced  $\mathcal{L}_2 \rightarrow \mathcal{L}_\infty$  norm from  $d$  to  $e$  of an uncertain LPV system  $\|\mathcal{F}_u(\mathbf{P}_\rho, \Delta)\|_{\mathcal{L}_2 \rightarrow \mathcal{L}_\infty}$  with  $\mathbf{D}_{21}(\rho) = \mathbf{0}$  and  $\mathbf{D}_{22}(\rho) = \mathbf{0}$  is smaller than a performance index  $\gamma$  if the interconnection is well posed for all  $\Delta \in \text{IQC}(\Psi, \mathbf{M})$  and if there exists a continuous differentiable Lyapunov matrix function  $\mathbf{X}: \mathcal{P} \rightarrow \mathbb{S}^{n_x}$  and a scalar  $\lambda > 0$  s.t. for all  $(p, q) \in \mathcal{P} \times \dot{\mathcal{P}}$*

$$\mathbf{X}(p) > 0, \quad (4.27a)$$

$$\begin{bmatrix} \mathbf{A}(p)^T \mathbf{X}(p) + \mathbf{X}(p) \mathbf{A}(p) + \partial \mathbf{X}(p, q) & \mathbf{X}(p) \mathbf{B}_1(p) & \mathbf{X}(p) \mathbf{B}_2(p) \\ \mathbf{B}_1(p)^T \mathbf{X}(p) & \mathbf{0} & \mathbf{0} \\ \mathbf{B}_2(p)^T \mathbf{X}(p) & \mathbf{0} & -\gamma \mathbf{I} \end{bmatrix} \\ + \lambda \begin{bmatrix} \mathbf{C}_1(p)^T \\ \mathbf{D}_{11}(p)^T \\ \mathbf{D}_{12}(p)^T \end{bmatrix} \mathbf{M} \begin{bmatrix} \mathbf{C}_1(p) & \mathbf{D}_{11}(p) & \mathbf{D}_{12}(p) \end{bmatrix} < 0, \quad (4.27b)$$

$$\begin{bmatrix} \mathbf{X}(p) & \mathbf{C}_2(p)^T \\ \mathbf{C}_2(p) & \gamma \mathbf{I} \end{bmatrix} > 0. \quad (4.27c)$$

**Proof:** The proof is similar to the proof of [Theorem 3.3](#). From well-posedness follows that the signals  $x$ ,  $e$ ,  $w$ ,  $v$ , and  $z$  due to an excitation  $d \in \mathcal{L}_2$  are well-defined. Since the LMIs (4.27) hold for all admissible parameter trajectories,  $\rho$  and  $\dot{\rho}$  can be substituted for  $p$  and  $q$ , respectively. This allows the definition of the storage function  $V: \mathbb{R}^{n_x} \times \mathcal{P} \rightarrow \mathbb{R}_+$

$$V(x, \rho) := x^T \mathbf{X}(\rho) x. \quad (4.28)$$

A small perturbation  $\varepsilon > 0$  is added to (4.27b) to yield a non-strict LMI. Next, left and right multiplication by  $[x^T \ w^T \ d^T]$  and its transpose, respectively, lead to the dissipation inequality

$$\frac{d}{dt} V(x, \rho) \leq (1 - \varepsilon) \gamma d^T d - \lambda z^T \mathbf{M} z. \quad (4.29)$$

Using  $x(0) = \mathbf{0}$ , integration w.r.t.  $t$  yields

$$V(x(T), \rho(T)) \leq (1 - \varepsilon) \gamma \int_0^T d(T)^T d(T) dt - \int_0^T \lambda z^T \mathbf{M} z dt. \quad (4.30)$$

Because of the IQC constraint (4.3) and  $\lambda > 0$ , the summand  $\lambda \int_0^T \mathbf{z}^T \mathbf{M} \mathbf{z} dt \geq 0$  and hence

$$V(\mathbf{x}(T), \boldsymbol{\rho}(T)) \leq (1 - \epsilon) \gamma \int_0^T \mathbf{d}(T)^T \mathbf{d}(T) dt. \quad (4.31)$$

Next, expanding (4.27c), using a Schur complement (see Lemma A.4), and left and right multiplication by  $\mathbf{x}^T$  and  $\mathbf{x}$ , respectively, results in

$$\frac{1}{\gamma} \mathbf{e}^T \mathbf{e} = \frac{1}{\gamma} \mathbf{x}^T \mathbf{C}(\boldsymbol{\rho})^T \mathbf{C}(\boldsymbol{\rho}) \mathbf{x} \leq \mathbf{x}^T \mathbf{X}(\boldsymbol{\rho}) \mathbf{x} = V(\mathbf{x}, \boldsymbol{\rho}). \quad (4.32)$$

The evaluation of (4.32) at  $t = T$  and the combination with (4.31) gives

$$\frac{1}{\gamma} \mathbf{e}(T)^T \mathbf{e}(T) \leq (1 - \epsilon) \gamma \int_0^T \mathbf{d}(T)^T \mathbf{d}(T) dt. \quad (4.33)$$

Taking the supremum w.r.t.  $T$  results finally in

$$\|\mathbf{e}\|_{\mathcal{L}_\infty} \leq \gamma \|\mathbf{d}\|_{\mathcal{L}_2}, \quad (4.34)$$

which completes the proof.  $\blacksquare$

For simplicity, the preceding theorem is given in terms of a single IQC  $(\boldsymbol{\Psi}, \mathbf{M})$ . It can easily be modified to handle multiples IQCs. Consider the case of multiple uncertainties, which are satisfied each by several IQCs. This leads to a list of IQCs defined by  $(\boldsymbol{\Psi}_i, \mathbf{M}_i)$  with  $i = 1, \dots, n_{\text{IQC}}$ . Every  $\boldsymbol{\Psi}_i$  is connected to the input and output of the corresponding uncertainty which yields the outputs

$$\mathbf{z}_i = \mathbf{C}_{1i} \mathbf{x} + \mathbf{D}_{11i} \mathbf{w} + \mathbf{D}_{12i} \mathbf{d}. \quad (4.35)$$

In (4.35),  $\mathbf{C}_{1i}$ ,  $\mathbf{D}_{11i}$  and  $\mathbf{D}_{12i}$  denote the output and feed-through matrices of the corresponding  $\boldsymbol{\Psi}_i$ . The states of  $\mathbf{P}_\rho$  and of all  $\boldsymbol{\Psi}_i$  are included in  $\mathbf{x}$  and the output of every uncertainty is contained in  $\mathbf{w}$ . In order to use Theorem 4.2 for computing the induced  $\mathcal{L}_2 \rightarrow \mathcal{L}_\infty$  norm of the resulting system, the second summand of the constraint (4.27b) is modified to

$$\sum_{i=1}^{n_{\text{IQC}}} \lambda_i \begin{bmatrix} \mathbf{C}_{1i}(\mathbf{p})^T \\ \mathbf{D}_{11i}(\mathbf{p})^T \\ \mathbf{D}_{12i}(\mathbf{p})^T \end{bmatrix} \mathbf{M}_i \begin{bmatrix} \mathbf{C}_{1i}(\mathbf{p}) & \mathbf{D}_{11i}(\mathbf{p}) & \mathbf{D}_{12i}(\mathbf{p}) \end{bmatrix}. \quad (4.36)$$

The positive scalars  $\lambda_i$  are additional unknowns in the SDP.

Note finally that the same step as for the nominal LPV analysis are applied in order to yield a numerical tractable SDP. Basis functions for the Lyapunov matrix function are assigned and the parameter space is gridded or the Full Block S-Procedure is used for an LFT based analysis. See Section 3.4 for details.

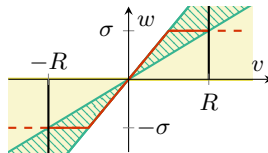
#### 4.2.4 Analysis of Saturated Systems using Local IQCs



In Section 4.1.2, standard constraints from the literature (Megretski and Rantzer, 1997; Zames and Falb, 1968) for the saturation function are given. While all these IQCs guarantee global robust performance of a system under saturation, all of them are independent of the saturation limit. Hence, they are expected to be very conservative for many practical applications. It is well understood in the literature that performance results which only hold locally can greatly improve the analysis of saturated systems by incorporating the actual saturation limit (see Hindi and Boyd, 1998; Hu, Lin, and Chen, 2002; Hu and Lin, 2002). If the global performance requirement is relaxed to only consider local performance, a modified, less conservative version of the sector bound IQC can be used.

The approach pursued in this thesis is based on the notion of local IQCs (Summers and Packard, 2010). There, a general framework for the local analysis of systems under perturbations described by IQCs is given. The specific nature of the perturbation, namely the saturation function, is exploited to obtain local conditions. The conditions are similar to the IQCs for saturations given in Fang, Lin, and Rotea (2008).

The global sector constraint for the saturation function is defined by the sector  $[0, 1]$ . It is easily seen that the sector bound holds independent of the size of the input  $v$  (see Figure 4.8). If an  $\mathcal{L}_\infty$  norm bound on the saturation input  $v$  is known, i.e.  $|v| \leq R$ , then a refined sector constraint can be given. Instead of checking over the whole sector  $[0, 1]$ , it is sufficient to only consider the smaller sector  $[\sigma/R, 1]$  (cf. Figure 4.8). Recall that  $\sigma$  is the saturation limit.

In order to validate the assumed  $\mathcal{L}_\infty$  bound  $R$  on  $v$ , the interconnection in Figure 4.9 is considered where the performance output is replaced by the (possibly vector valued) nonlinearity input  $v$ . Assume that the disturbance energy is constrained by  $\|d\|_{\mathcal{L}_2} \leq 1$ . Next the induced  $\mathcal{L}_2 \rightarrow \mathcal{L}_\infty$  norm  $\gamma$  from  $d$  to the nonlinearity input  $v$  is computed using Theorem 4.2. If  $\gamma < R$ , then  $\|v\|_{\mathcal{L}_\infty} \leq R$ . Hence, the condition for applying the local IQC is satisfied. While this appears to be a circle conclusion, the following theorem proves the validity of this statement. The theorem is adapted from Summers and Packard (2010) which considers local IQCs w.r.t.  $\mathcal{L}_2$  bounds for  $v$ .



**Figure 4.8:** Local sector constraint IQC for saturation: Because of  $|v| \leq R$ , only the solid drawn part of the saturation (—) can be reached but not the dashed one (---). This allows to decrease the sector from  to .

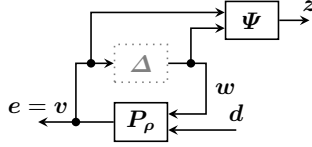


**Figure 4.9:** Analysis interconnection for validating a local IQC: The performance output  $e$  is replaced by the nonlinearity input  $v$ .

**Theorem 4.3:** Consider the interconnection in Figure 4.9. Assume that the interconnection is well posed, that  $\Delta$  satisfies the IQC  $(\Psi, \mathbf{M})$  locally for  $\|v\|_{\mathcal{L}_\infty} < R$ , and that  $\|d\|_{\mathcal{L}_2} \leq 1$ . If Theorem 4.3 is satisfied with  $\gamma < R$ , then  $\|v\|_{\mathcal{L}_\infty} < R$ . Further, the conditions for applying the local IQC are satisfied.

**Proof:** From Theorem 4.3 and  $\|d\|_{\mathcal{L}_2} \leq 1$ , it follows that  $\|v\|_{\mathcal{L}_\infty} < \gamma$ . In order to prove that  $\gamma < R$  validates the local IQC, the LMIs from (4.27) are transformed to

$$v(T)^T v(T) \leq \gamma^2 \int_0^T d(t)^T d(t) dt - \gamma \lambda \int_0^T z(t)^T M z(t) dt \quad (4.37)$$

(cf. the proof of Theorem 4.3 for details and replace  $e$  by  $v$ ).

Next, the function

$$N(T) = \sqrt{\sup_{0 \leq t \leq T} v(t)^T v(t)} \quad (4.38)$$

is defined. Note that  $N(T)$  represents the  $\mathcal{L}_\infty$  norm of  $v$  truncated at the time  $T$ . Because the states  $x$  are continuous functions of the time and  $v = C_2 x$ ,  $N(T)$  must also be continuous. By definition,  $N(T)$  is further a non-decreasing function. From the zero initial condition follows further that  $N(0) = 0$ .

Assume by contradiction that there exists a  $\tilde{T}$  such that  $N(\tilde{T}) > R$ . Because  $N(T)$  is a continuous, non-decreasing function with  $N(0) = 0$ , this implies the existence of a  $\hat{T} < \tilde{T}$  s.t.  $N(\hat{T}) = R$  and  $N(T) < R$  for all  $T < \hat{T}$ . Hence, on the interval  $[0, \hat{T}]$ , the IQC  $(\Psi, \mathbf{M})$  is locally satisfied. Consequently, in Equation (4.37),  $\gamma \lambda \int_0^T z(t)^T M z(t) dt > 0$  for all  $0 \leq T \leq \hat{T}$  and hence

$$v(T)^T v(T) \leq \gamma^2 \int_0^T d(t)^T d(t) dt. \quad (4.39)$$

Taking the supremum of (4.39) w.r.t.  $0 \leq T \leq \hat{T}$  yields

$$R^2 = N^2(\hat{T}) \leq \gamma^2 \int_0^{\hat{T}} d(t)^T d(t) dt \leq \gamma^2 \|d\|_{\mathcal{L}_2} < \gamma^2. \quad (4.40)$$

Hence,  $R < \gamma$  which contradicts  $\gamma < R$  and proves the theorem.  $\blacksquare$

For simplicity, the preceding theorem considers only a single nonlinearity and a single IQC. It can easily be modified to deal with multiple global and local IQCs (cf. [Summers and Packard, 2010](#)). It is further possible, to use local IQCs w.r.t. both  $\mathcal{L}_2$  and  $\mathcal{L}_\infty$  bounds on  $v$ .

In order to reduce the conservatism of the analysis, a possibly small bound on  $v$  should be determined. In case of using the sector IQC for the saturation nonlinearity, this can be achieved by the iterative procedure in [Algorithm 4.1](#).

---

**Algorithm 4.1:**

---

- 1: compute the nominal induced  $\mathcal{L}_2 \rightarrow \mathcal{L}_\infty$  norm  $\gamma_0$  from  $d$  to  $v$
  - 2: **repeat**
  - 3:   use  $R_i = 1.1 \cdot \gamma_{i-1}$  to define the local sector IQC for sector  $[\max(\sigma/R_i, 1), 1]$
  - 4:   compute the robust induced  $\mathcal{L}_2 \rightarrow \mathcal{L}_\infty$  norm  $\gamma_i$  from  $d$  to  $v$
  - 5: **until**  $\gamma_i < R_i$
  - 6: compute the induced  $\mathcal{L}_2 \rightarrow \mathcal{L}_\infty$  norm of the performance channel
- 

In order to find an initial guess for the  $\mathcal{L}_\infty$  bound on  $v$ , the nominal induced  $\mathcal{L}_2 \rightarrow \mathcal{L}_\infty$  norm  $\gamma_0$  from  $d$  to  $v$  is computed ([Step 1](#)). Because the nominal analysis probably underestimates the true bound, a back-off factor of 1.1 is used to get a bound  $R_i$  and to define a sector IQC for the local analysis ([Step 3](#)). In [Step 4](#), this local and other global IQCs are then use to compute the robust induced  $\mathcal{L}_2 \rightarrow \mathcal{L}_\infty$  norm  $\gamma_i$  from  $d$  to  $v$  by using [Theorem 4.2](#). In combination with  $\|d\|_{\mathcal{L}_2} \leq 1$ , this allows to apply [Theorem 4.3](#). If this step fails, [Steps 3](#) and [4](#) are repeated until  $\gamma_i < R_i$ . In [Step 6](#), an upper bound for the worst case energy-to-peak gain of the performance channel is computed. Note that in the last step the more common worst case energy gain can be alternatively considered using [Theorem 4.1](#).

In an early version of [Algorithm 4.1](#) (see [Knoblach, Pfifer, and Seiler, 2015](#)), a global analysis is performed to validate the local IQC constraint. The benefit of this new approach is that the iteration can be directly started with a local IQC. The advantage is that this allows to analyze systems which are only locally – but not globally – stable. Additionally, the convergence behavior is improved.

## 4.3 Analysis of an Aeroelastic System

In order to evaluate the proposed approach and to investigate the effects of different IQCs, the worst case energy-to-peak gain of a simple aeroservoelastic system is computed. An aeroelastic system in combination with a gust load alleviation system is considered.

### 4.3.1 Aeroservoelastic System

A similar system as for the benchmark in [Section 3.5](#) is used. The difference is that a flap is added which can be used to actively reduce the gust loads. The example

system is illustrated in [Figure 4.10](#). The equations of motion are

$$\begin{bmatrix} m & m \cdot x_{cg} \\ m \cdot x_{cg} & I \end{bmatrix} \begin{bmatrix} \ddot{h} \\ \ddot{\alpha} \end{bmatrix} + \begin{bmatrix} k_h & 0 \\ 0 & k_\alpha \end{bmatrix} \begin{bmatrix} h \\ \alpha \end{bmatrix} = \begin{bmatrix} -L \\ \tau \end{bmatrix} \quad (4.41)$$

where  $h$  denotes the vertical deflection and  $\alpha$  the pitch angle. The lift  $L$  and the pitching moment  $\tau$  are given by

$$\begin{bmatrix} -L \\ \tau \end{bmatrix} = \frac{1}{2} \rho v^2 \begin{bmatrix} \mathbf{Q}_{\text{eig}}(s) & | & \mathbf{Q}_{\text{gust}}(s) \end{bmatrix} \begin{bmatrix} h \\ \alpha \\ \beta \\ v_{\text{gust}} \end{bmatrix}. \quad (4.42)$$

The Theodorsen function  $\mathbf{Q}_{\text{eig}}(s)$  models the relation between the aerodynamic forces and the heave, the pitching and the flap movement, denoted  $h$ ,  $\alpha$ , and  $\beta$ , respectively. The Sears function  $\mathbf{Q}_{\text{gust}}(s)$  maps the vertical gust velocity  $v_{\text{gust}}$  on  $L$  and  $\tau$ . Both transfer functions are non-rational in the Laplace domain. In order to yield a state space realization, R. T. Jones' rational approximation is used. The functions depend on the free stream velocity  $U_\infty$ , the half chord length  $b$ , the location of the aerodynamic reference axis  $x_{\text{ar}}$ , and the hinge position  $x_{\text{hp}}$ .  $\mathbf{Q}_{\text{eig}}$  and  $\mathbf{Q}_{\text{gust}}$  are explicitly given in [Bisplinghoff, Ashley, and Halfman \(1955\)](#). Here, the velocity  $U_\infty$  is considered as scheduling parameter. Ten equidistantly spaced grid points in the interval  $U_\infty \in [0.3, 0.9]$  are used. The rate bounds are  $\dot{U}_\infty \in [-0.1, 0.1]$ . The other parameters are compiled in [Table 4.1](#).

The closed loop configuration in [Figure 4.11](#) is considered. The weighting filter  $W$  defined by

$$\dot{x}_W = \frac{1}{10} x_W + \frac{1}{10} d \quad (4.43a)$$

$$v_{\text{gust}} = x_W \quad (4.43b)$$

is used to shape suitable gusts with unit energy. The performance outputs are the spring forces

$$\mathbf{e} = \begin{bmatrix} e_h \\ e_\alpha \end{bmatrix} = \begin{bmatrix} k_h \cdot h \\ k_\alpha \cdot \alpha \end{bmatrix}. \quad (4.44)$$

The first order low pass filter  $G_{\text{act}}$

$$\dot{x}_{\text{act}} = x_{\text{act}} + u \quad (4.45a)$$

$$v = x_{\text{act}} \quad (4.45b)$$

serves as an actuator model. Since the flap deflection  $\beta$  is assumed to be limited, saturation

$$\beta = w = \text{sat}(v) \quad (4.46)$$

is added.



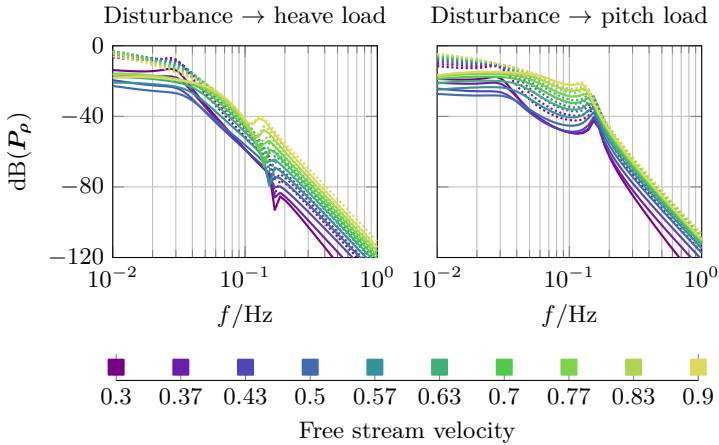


**Figure 4.12:** Bode diagram of the aeroservoelastic system: The ..... lines represent the open loop and — ones the nominal closed loop. The color indicates the free stream velocity.

A simple gust load alleviation system which is based on a gain scheduled (by  $U_\infty$ ) proportional controller  $\mathbf{K}$

$$u = \begin{bmatrix} 4.2 & -27.3 & 149.2 \end{bmatrix} + U_\infty \begin{bmatrix} 0.19 & -49.4 & 138.6 \end{bmatrix} \begin{bmatrix} v_{gust} \\ e_h \\ e_\alpha \end{bmatrix} \quad (4.47)$$

is used to close the loop. The controller is tuned using `syntune` (Apkarian and Noll, 2006). The tuning goal is to minimize the variance of the performance output.

Since the parameter dependence of the resulting state space model is highly involved, the open loop state space matrices are compiled in Appendix B.2. A Bode diagram of the open and the nominal closed loop (i.e., without saturation) is depicted in Figure 4.12 for different parameter values.

### 4.3.2 Comparison of IQCs

The effect of different IQCs is investigated using the LTI model corresponding to the highest free stream velocity. The globally valid sector  $[0, 1]$  is considered separately, in combination with the Popov IQC and in combination with three different parameterizations of the Zames-Falb IQC. The Zames-Falb IQC is parameterized by a first order low pass filter

$$H(s) = \frac{1}{\frac{1}{T_{ZF}}s + 1}, \quad (4.48)$$

**Table 4.2:** Results for several IQC combinations.

$T_{ZF}$	S	S/P	S/ZF 0.01	S/ZF 0.1	S/ZF 1	S/P/ZF all
Norm	0.185	0.184	0.183	0.175	0.181	0.175
Impr.	0%	0%	1%	5%	2%	5%

where the three values for the time constant  $T_{ZF} \in \{0.01, 0.1, 1\}$  are used. Finally, the combination of the sector IQC, the Popov IQC, and all three Zames-Falb IQCs is considered. The results are compiled in [Table 4.2](#). The best result is achieved using the sector IQC and the Zames-Falb IQC with  $T_{ZF} = 0.1$ . The results cannot be improved by adding the Popov IQC or combining several Zames-Falb IQCs. For that reason, the sector and the Zames-Falb IQCs with  $T_{ZF} = 0.1$  are used below.

### 4.3.3 Convergence of Local IQCs

The convergence behavior of [Algorithm 4.1](#) is investigated using two examples.

#### Example 1

The LPV model from [Section 4.3.1](#) is used and the six saturation limits  $\sigma \in \{0, 3, \dots, 15\}$  are considered. The Lyapunov matrix is parameterized by a quadratic function. The results are depicted in [Figure 4.13a](#), where the induced  $\mathcal{L}_2 \rightarrow \mathcal{L}_\infty$  norm is plotted as a function of the iteration. In the left subplot, the norm from the disturbance to saturation input can be seen and, in the right one, the norm of the performance channel.

First of all, the initial guesses for the sector constraint using the nominal analysis result are already close to the converged result. This leads to a fast convergence after the second iteration. The upper bound for the worst case energy-to-peak gain from the gust to the saturation input can be reduced by only 2 %. However, the proposed algorithm allows to reduce the upper bound for the performance channel by up to 69 % (depending on the saturation limit).

In order to estimate the conservatism induced by the description of saturation with IQCs, the robust analysis results are compared to standard LPV analysis results for the open and the nominal closed loop. A saturation limit of zero corresponds to the open loop. Using [Algorithm 4.1](#) for a zero saturation limit leads to conservative results, as it can be seen in [Figure 4.13a](#). The reason for this is that a zero saturation limit leads always to the sector  $[0, 1]$ .

On the contrary, a very high saturation limit corresponds to the nominal closed loop. Specifically, an  $\mathcal{L}_\infty$  norm of the saturation input less than the saturation limit results in a never saturated system. Consequently, the sector converges to  $[1, 1]$  which represents the smallest possible sector. In the considered example, the upper bound for the robust norm for a saturation limit of  $\sigma = 15$  becomes even

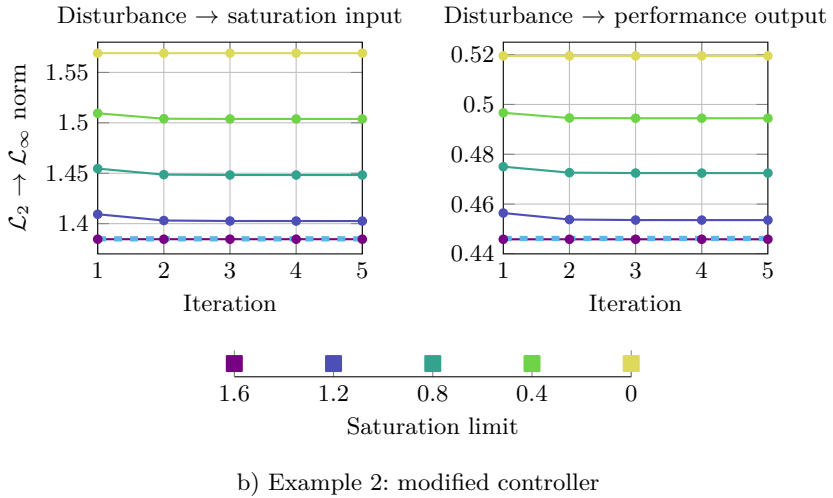
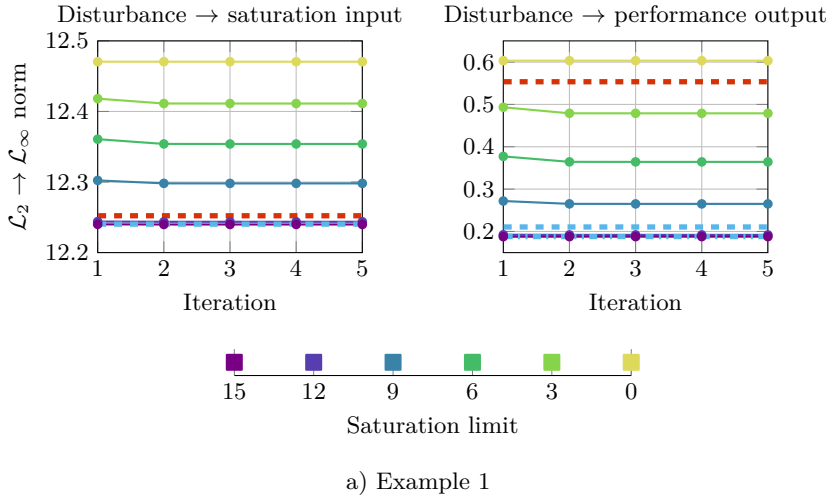


**Figure 4.13:** Convergence of local IQCs: The induced  $\mathcal{L}_2 \rightarrow \mathcal{L}_\infty$  gain is depicted as function of the iteration number ( $\bullet$ ) for several saturation limits indicated by the color. The results are compared to the open ( $\text{---}$ ) and the nominal closed ( $\text{---}$ ) loop results. In case of the closed loop, a third order test function for the Lyapunov matrix ( $\text{---}$ ) is additionally considered.

smaller than the result for the nominal closed loop. The reason for this unexpected result is that the nominal LPV analysis is already conservative. In case of the robust analysis, the additional state of the Zames-Falb IQC introduces additional decision variables which reduce the conservatism. However, using a third order test function for the Lyapunov matrix function yields consistent results.

### Example 2

In the first examples, the  $\mathcal{L}_\infty$  norm bound for the saturation input varies only slightly (see Figure 4.13a). This means that the variable  $R_{i+1}$  in Algorithm 4.1 (Step 4) is almost constant and consequently the algorithm converges extremely fast. In order to examine the convergence behavior of Algorithm 4.1 if this is not the case, a second example is considered. To that end, the feedforward path of the gust load alleviation system is removed, i.e., the modified controller  $\mathbf{K}$  is

$$u = \left( \begin{bmatrix} 0 & -27.3 & 149.2 \end{bmatrix} + U_\infty \begin{bmatrix} 0 & -49.4 & 138.6 \end{bmatrix} \right) \begin{bmatrix} v_{\text{gust}} \\ e_h \\ e_\alpha \end{bmatrix}. \quad (4.49)$$

Further, the saturation limits  $\sigma \in \{0, 0.4, \dots, 1.6\}$  are used. All other parameters are identical to the preceding examples. The results are depicted in Figure 4.13b in the same fashion.

It is easy to see that the  $\mathcal{L}_\infty$  norm bound for the saturation input norm bound varies larger. Here, this bound can be reduced by approximatively 15 % (compared to 2 % in the first example). However, the convergence of the algorithm is still excellent. The convergence behavior of Algorithm 4.1 appears hence to be very good.

### 4.3.4 Influence of the Parameter Rate Bounds

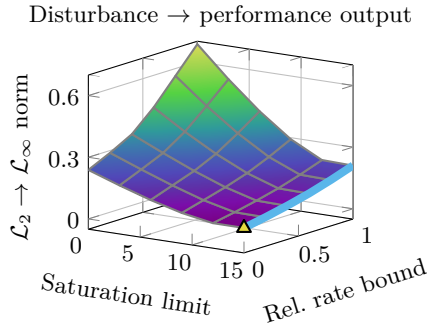
In a last example, the influence of the parameter rate bounds is analyzed. To that end, Algorithm 4.1 is used to compute an upper bound of the induced  $\mathcal{L}_2 \rightarrow \mathcal{L}_\infty$  norm for the saturation limits  $\sigma \in \{0, 3, \dots, 15\}$  and for the rate bounds  $\dot{U}_\infty \in [-0.1\nu, 0.1\nu]$  with  $\nu \in \{0.0, 0.2, \dots, 1.0\}$ . The results are illustrated in Figure 4.14.

Regarding the saturation limits, the results from the preceding subsection hold for all parameter rate bounds. For high saturation limits, the norm bounds converge to the nominal LPV analysis results. As expected, reducing the parameter rate bounds leads to a smaller upper bound. If the rate bound approaches zero, the robust analysis converges to the maximum LTI norm w.r.t. all ten nominal closed loop models. The latter norm is known not to be conservative and provides consequently a lower bound for the worst case performance.

### 4.3.5 Conclusions

The analysis of saturated LPV systems using IQCs is discussed in this section. In order to reduce the conservatism of the analysis results, an iterative procedure to

**Figure 4.14:** Influence of the parameter rate bounds: The induced  $\mathcal{L}_2 \rightarrow \mathcal{L}_\infty$  norm is computed for several rate bounds and saturation limits and compared to norms of the nominal closed loop (—). Finally,  $\Delta$  indicates the maximum LTI norm of the nominal closed loop.



refine local IQCs is proposed. This method is intensively studied at the example of a two-dimensional thin airfoil in combination with a gust load alleviation system. Summarizing, it can be said that the results are conservative if a low saturation limit is considered and the system is most of the time saturated. On the contrary, for relatively high saturation limits, [Algorithm 4.1](#) converges to the nominal case and is hence only slightly conservative. However, this approach allows to compute guaranteed upper bounds for the outputs of saturated LPV systems.

## 5 LTI Performance Analysis for Gust Loads Computation

While robust control theory methods have been accepted as powerful tools for flutter analysis (see e.g., [Lind and Brenner, 1999](#); [Borglund, 2003](#); [Borglund, 2004](#); [Borglund, 2005](#)), they have never been used for loads analysis. However, the similarities between the discrete gust problem and the energy-to-peak gain are obvious. In both cases, a set of models is considered and there is the question: what are the maximum output peaks? The aim of this chapter is consequently to investigate if and how the energy-to-peak gain can be used for the discrete gust problem. It is shown how this method can be used to determine guaranteed upper bounds for the peak loads and how to efficiently identify critical flight points.

The chapter is organized as follows: A weighting filter is introduced and designed in [Section 5.1](#). Next,  $\mathcal{L}_\infty$  norm bounds for the peak loads are computed using the worst case energy-to-peak gain in [Section 5.2](#). The analysis results are compared to the simulation results from [Section 2.2](#). Additionally, worst case excitations for specific cases are computed and the inclusion of the trim loads is demonstrated. The determination of lower bounds for the peak loads is treated in [Section 5.3](#). Finally, the results are evaluated and discussed in [Section 5.4](#). Note that the present chapter extends results from [Knobloch \(2013b\)](#) and [Knobloch \(2013a\)](#) where a simpler model with only two – instead of more than several hundreds – outputs is considered.

### 5.1 Weighting Filter

By definition, the worst case energy-to-peak gain represents an  $\mathcal{L}_\infty$  norm bound for the output caused by an arbitrary excitation with a maximum energy of  $\|d\|_{\mathcal{L}_2} \leq 1$ . Such an excitation is obviously not the same as a “one-minus-cosine” gust. In order to remedy this problem, a weighting filter is introduced (see [Figure 5.1](#)). Assume that this pre-filter is able to create a “one-minus-cosine” gust of arbitrary

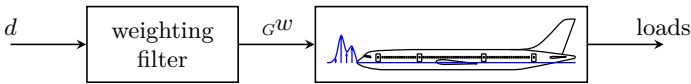


**Figure 5.1:** Interconnection of the aircraft model and the weighting filter.

length with a maximum energy of  $\|d\|_{\mathcal{L}_2} \leq 1$ . Then, the induced  $\mathcal{L}_2 \rightarrow \mathcal{L}_\infty$  norm of the weighted system represents an upper bound for the gust peak loads. Note that the weighting filter must be stable and strictly proper in order to fulfill the requirements for a finite induced  $\mathcal{L}_2 \rightarrow \mathcal{L}_\infty$  norm (see [Remark 3.1](#)).

### 5.1.1 Design of the Weighting Filter

Recall the definition of the “one-minus-cosine” gust excitation

$${}_G w(t) = \begin{cases} \frac{U_{\text{ref}} \cdot F_g}{2U_\infty} \left( \frac{H}{107 \text{ m}} \right)^{1/6} \left( 1 - \cos \left( \pi \frac{U_\infty t}{H} \right) \right) & \text{if } 0 \leq U_\infty t \leq 2H \\ 0 & \text{otherwise.} \end{cases} \quad (5.1)$$

(cf. [Section 2.2](#), [Equations \(2.28\)](#) and [\(2.29\)](#)). Because this excitation depends on the flight speed  $U_\infty$  as well as on the design gust speed defined by  $U_{\text{ref}}$  and  $F_g$ , a reasonable weighting filter must depend on the same parameters. In order to remove these dependences for the filter design, all quantities are normalized. This is indicated by overlining the variable, e.g.,  $\bar{t}$ .

Here, the time and accordingly the Laplace variable<sup>1</sup> are normalized by

$$\bar{t} = t \cdot U_\infty / 1 \text{ m} \quad \text{and} \quad \bar{s} = s \cdot 1 \text{ m} / U_\infty. \quad (5.2)$$

Assume that the filter  $\bar{W}$  maps the disturbance  $\bar{d}$  with  $\|\bar{d}\|_{\mathcal{L}_2} = 1$  to the normalized “one-minus-cosine” gust of arbitrary length

$${}_G \bar{w}(\bar{t}) = \frac{U_\infty}{U_{\text{ref}} \cdot F_g} \cdot {}_G w(\bar{t} \cdot 1 \text{ m} / U_\infty). \quad (5.3)$$

In order to revoke the normalization of the signals,  $\bar{t} = t \cdot U_\infty / 1 \text{ m}$  is substituted and the signals are appropriately scaled. Because the normalization changes the  $\mathcal{L}_2$  norm of a signal, the disturbance is multiplied with  $1/\sqrt{U_\infty}$  to keep  $\|d\|_{\mathcal{L}_2} = 1$ . For achieving the correct amplitude of the “one-minus-cosine” gust,  ${}_G \bar{w}$  must be multiplied with the factor  $U_{\text{ref}} \cdot U_\infty^{-1} \cdot F_g$ . The denormalized weighting filter can thus be achieved by applying both factors:

$$W(s) = U_{\text{ref}} \cdot U_\infty^{-3/2} \cdot F_g \cdot \bar{W}(s \cdot 1 \text{ m} / U_\infty). \quad (5.4)$$

The denormalization of all quantities is summarized in [Table 5.1](#).

In order to ensure a unique state space representation of the weighting filter at all flight points, its denormalization is analogously expressed in its state space

<sup>1</sup>Note that the normalized Laplace variable is related to the reduced Laplace variable of the DLM which depends on the reference chord length (see [Section 2.1](#), [Equation \(2.14\)](#)). In order to avoid a dependence on aircraft specific parameters, a reference chord length of  $c_{\text{ref}} = 2 \text{ m}$  is used for the weighting filter.

**Table 5.1:** Denormalization of the disturbance, the gust, and the weighting filter.

Disturbance:	$d(t) = U_\infty^{-1/2} \cdot \bar{d}(t \cdot U_\infty / 1 \text{ m})$
Gust:	${}_G w(t) = U_{\text{ref}} \cdot U_\infty^{-1} \cdot F_g \cdot {}_G \bar{w}(t \cdot U_\infty / 1 \text{ m})$
Filter:	$W(s) = U_{\text{ref}} \cdot U_\infty^{-3/2} \cdot F_g \cdot \bar{W}(s \cdot 1 \text{ m} / U_\infty)$

representation. Let  $\bar{W}(\bar{s}) = \bar{\mathbf{C}}_W (\mathbf{I}\bar{s} - \bar{\mathbf{A}}_W)^{-1} \bar{\mathbf{C}}_W$ , then  $W(s)$  can be realized using the matrices  $\mathbf{A}_W = U_\infty \cdot \bar{\mathbf{A}}_W$ ,  $\mathbf{B}_W = U_\infty \cdot \bar{\mathbf{B}}_W$ , and  $\mathbf{C}_W = U_{\text{ref}} \cdot U_\infty^{-3/2} \cdot F_g \cdot \bar{\mathbf{C}}_W$ . Recall that  $\mathbf{D}_W$  must be zero to meet [Remark 3.1](#).

The remaining problem is to find a weighting filter  $\bar{W}$  which is able to create all normalized “one-minus-cosine” gusts  ${}_G \bar{w}$  with maximal unit energy. Obviously, this filter is not unique and hence there is the question which is the best one. Here it is decided to define the best filter as the one which requires a similar amount of energy to create “one-minus-cosine” gusts of all possible lengths. In order to solve the resulting optimization problem, the required energy for creating a specific gust must be computed. This requires the inversion of a test weighting filter  $\widetilde{W}$ . Recall that the weighting filter must be strictly proper which complicates the inversions in the time domain. Consequently, the inversion is performed in the frequency domain, which leads to

$$\bar{d}(\bar{s}) = \widetilde{W}(\bar{s})^{-1} {}_G \bar{w}(\bar{s}). \quad (5.5)$$

Using Parseval’s Theorem ([Zhou and Doyle, 1998](#)), the energy of  $\bar{d}$  is

$$\|\bar{d}\|_{\mathcal{L}_2} = \frac{1}{2\pi} \int_{-\infty}^{\infty} \left| \widetilde{W}(\mathrm{j}\bar{\omega})^{-1} {}_G \bar{w}(\mathrm{j}\bar{\omega}) \right|^2 \mathrm{d}\bar{\omega}. \quad (5.6)$$

Note that  $\|\bar{d}\|_{\mathcal{L}_2}$  is a function of the gust length  $H$ . In order to find an optimal filter as defined above, the ratio between the maximum required energy and the minimum required energy is minimized. The optimization problem is thus

$$\min_{\widetilde{W}} \frac{\max_H \|\bar{d}\|_{\mathcal{L}_2}}{\min_H \|\bar{d}\|_{\mathcal{L}_2}}. \quad (5.7)$$

Using the optimal solution  $\widetilde{W}_{\text{opt}}$ , the desired weighting filter is

$$\bar{W} = \max_H \|\bar{d}\|_{\mathcal{L}_2} \widetilde{W}_{\text{opt}}, \quad (5.8)$$

which ensures that all discrete gusts can be indeed created with unit energy.

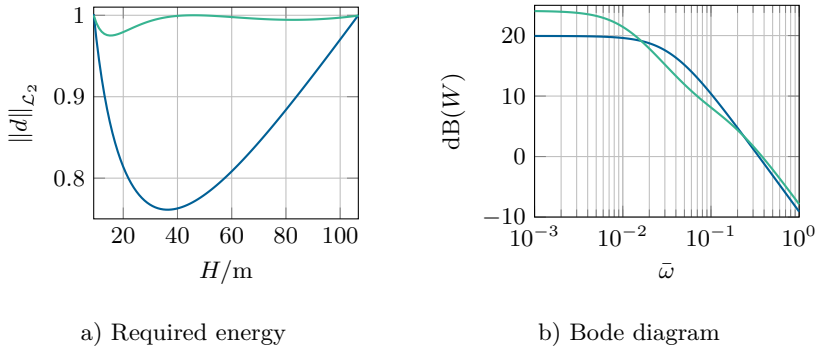


**Figure 5.2:** Optimization results for the weighting filter: In the left plot, the required energy to create a “one-minus-cosine” gust is plotted as a function of the gust length. The first order system is drawn by — and the second order system by —. The corresponding Bode diagrams are depicted in the right plot.

The test filter is parametrized with

$$\widetilde{W} = \frac{\sum_{i=1}^{n-1} b_i \bar{\omega}^i}{\sum_{i=1}^n a_i \bar{\omega}^i}, \quad (5.9)$$

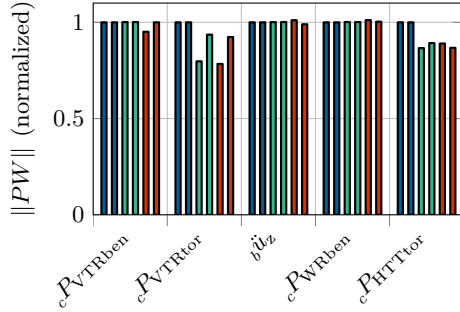
where  $a_i$  and  $b_i$  are the decision variables. This parameterization ensures a strictly proper result. As it can be seen in Equation (5.6), the phase of the filter does not affect the result. Consequently, any unstable pole or zero can be mirrored into the left half plane. The optimization is performed using MOPS (see Joos et al., 2002). Because no good initial values could be found intuitively, a genetic algorithm is used in a first step. The final optimization is pursued using a gradient free pattern search algorithm.

Results for a first and a second order filter are depicted in Figure 5.2. As it can be seen in Figure 5.2a, the required energy for a 40 m gust using the first order filter is less than 0.80. On the contrary, the minimum required energy using the second order system is already 0.98. This can be only slightly improved with a higher order system. The corresponding Bode diagrams are depicted in Figure 5.2b.

### 5.1.2 Evaluation of the Weighting Filter

Since the weighting filter crucially affects the conservatism of the analysis, the chosen filter is evaluated carefully. To that end, the energy-to-peak gains for specific outputs are computed using different weighting filters. The considered

**Figure 5.3:** Energy-to-peak gain for different weighting filters: The original weighting filter (blue) is compared with a brute force optimized one (green). A modification of the original filter (red) yields comparable results. The results are normalized with the original weighting filter. The two bars per filter and per interesting quantity represent the two flight points.



flight points are ( $Ma = 0.26, h = 0 \text{ km}$ ) and ( $Ma = 0.86, h = 10.74 \text{ km}$ ). The considered interesting quantities are the VTP root torsional moment ( $cP_{VTRtor}$ ) and the torsional bending moment close to the HTP tip ( $cP_{HTTtor}$ ). Additionally, the following general important interesting quantities are considered: the VTP root bending moment ( $cP_{VTRben}$ ), the vertical rigid body acceleration ( $b_{\ddot{u}_z}$ ), and finally the wing root bending moment ( $cP_{WRben}$ ).

In order to investigate the conservatism induced by the weighting filter, the second order weighting filter from the preceding section (referred to as original one) is compared with a brute force optimized filter. The optimization of this filter aims directly at minimizing the energy-to-peak gain for the considered transfer paths, which allows to detect conservatism due to a badly chosen weighting filter. The filter's FRF is directly parameterized, i.e., the decision variables are the discrete frequencies  $\bar{\omega}_i$  and the corresponding gains  $\bar{W}_0(\bar{\omega}_i)$ .<sup>2</sup> Here, 25 sampling points are used and frequency points in between are obtained by interpolation. Beside the different decision variables and the different criterion, the optimization is performed analogously to the preceding section. Since the problem is well conditioned and reasonable initial values are known from the original weighting filter, the pattern search algorithm is used directly. Because this filter is only optimal for the considered aircraft and outputs, it is only used as a reference for the chosen weighting filter but not for an analysis of the complete aircraft.

The resulting energy-to-peak gains are depicted in Figure 5.3. The results indicate that the original weighting filter is indeed conservative for some interesting quantities. An analysis of the corresponding Bode diagrams (see Figure 5.4) indicates the need for an additional roll-off for frequencies  $\bar{\omega} > 1$ . Consequently, the original weighting filter is modified by multiplying a second order Butterworth filter with a cut-off frequency of  $\bar{\omega} = 1.7$ . Note that this requires to increase the gain of the filter slightly in order to be still able to create all gusts with unit energy. The results are additionally depicted in Figures 5.3 and 5.4 where a good agreement

<sup>2</sup>Recall that the phase has no effect on the results and is thus neglected.

**Figure 5.4:** Bode diagram of different weighting filters: The brute force optimized filter (—) is compared to the original filter (—). The sampling points of the optimization are • and the modified filter is - - -.

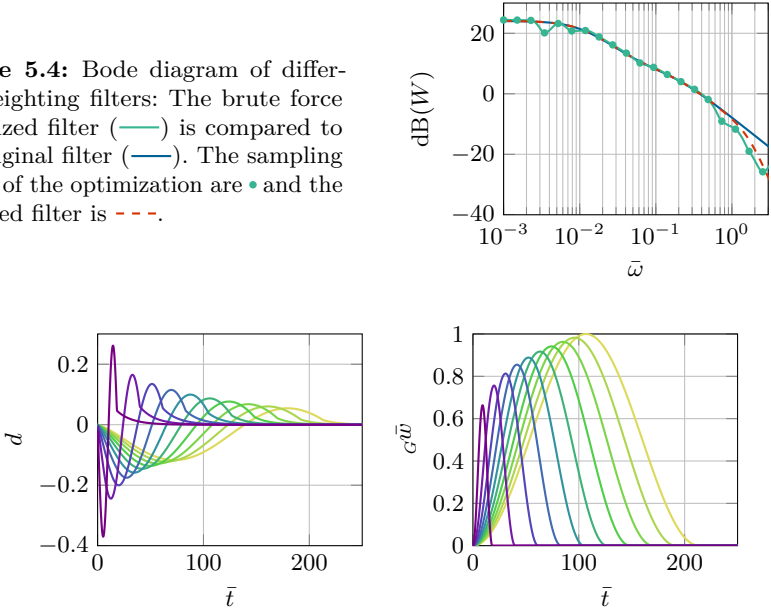


**Figure 5.5:** Disturbance and weighting filter output: The disturbances  $d$  are chosen such that the filter outputs match the normalized “one-minus-cosine” gusts.

with the brute force optimized filter can be seen. Consequently, the modified filter is proved valid and is used through the remaining part of this thesis.

In order to validate the design steps, the required disturbances and the corresponding filter outputs are finally depicted in Figure 5.5. For the purpose of validation, the  $\mathcal{L}_2$  norms of the disturbances are computed in the time domain. The results are identical to their frequency domain counterparts. The weighting filter outputs match perfectly the normalized “one-minus-cosine” gusts. Because of the non-proper weighting filter, the inverse filter cannot be directly realized. As a remedy, a third order low pass filter is applied to the weighting filter. The additional poles at  $\bar{\omega} = -10^5$  are far beyond the excitation’s frequency range, so that they do not affect the results.

## 5.2 Determination of Worst Case Gust Loads

The worst case energy-to-peak gain is used in this section for the analysis of gust loads. First, implementational aspects are discussed. Next, the wing loads are

analyzed and worst case excitations for selected interesting quantities and flight points are presented. Afterwards, the inclusion of trim loads is presented. Finally, the analysis results for the HTP and VTP are briefly discussed.

### 5.2.1 Implementational Aspects

Both gust directions are separately analyzed by connecting the considered gust input with the weighting filter of [Section 5.1](#). For the vertical gust, the considered model outputs are the wing and HTP shear, torsional, and bending loads. Because the lateral gust input is omitted, the resulting model has 726 states. The number of considered outputs is 162. In cases of the lateral gust, the model outputs are the VTP shear, torsional and bending loads. The resulting model has 728 states and 51 outputs.

In order to determine the induced  $\mathcal{L}_2 \rightarrow \mathcal{L}_\infty$  norm for every output, [Theorem 3.4](#) is used. To that end, the controllability Gramian  $\mathbf{W}_c$  is computed only once using the `gram` command of the Matlab's Control System Toolbox (see *Control System Toolbox: User's Guide* 2013). Afterwards, every row of the output matrix  $\mathbf{C}_{i\bullet}$  is used individually:

$$\|P_{d \rightarrow e_i}\|_{\mathcal{L}_2 \rightarrow \mathcal{L}_\infty} = \sqrt{\mathbf{C}_{i\bullet} \mathbf{W}_c \mathbf{C}_{i\bullet}^T}. \quad (5.10)$$

The advantage of this approach is that the numerically expensive computation of the controllability Gramian has to be performed only once. The bounds for every interesting quantity can be subsequently computed by “cheap” matrix multiplications.

### 5.2.2 Analysis of the Wing Loads

Since the weighting filter is able to create an arbitrary “one-minus-cosine” gust with unit energy, the induced  $\mathcal{L}_2 \rightarrow \mathcal{L}_\infty$  norm of the weighted model provides an  $\mathcal{L}_\infty$  norm bound for the gust peak loads. In a first step, this norm bound is compared to the peak loads from discrete gust simulations. The peaks and the norm bounds are depicted w.r.t. the flight point<sup>3</sup> and the wing span in [Figure 5.6](#). Obviously, the absolute values of the peaks and the norm are not the same. Nevertheless, the shape of the plots in both columns looks very similar.

In order to verify the similarity between both shapes, the ratio of the norm bound to the peaks is depicted in [Figure 5.7](#). The division by the peaks from the simulations implies that a ratio of one is the optimal result and any larger value is a direct measure of the conservatism. Additionally, some statistical key values of the norm to peak ratio are compiled in [Table 5.2](#).

---

<sup>3</sup>The flight points are firstly sorted according to the Mach number and secondly w.r.t. the altitude.

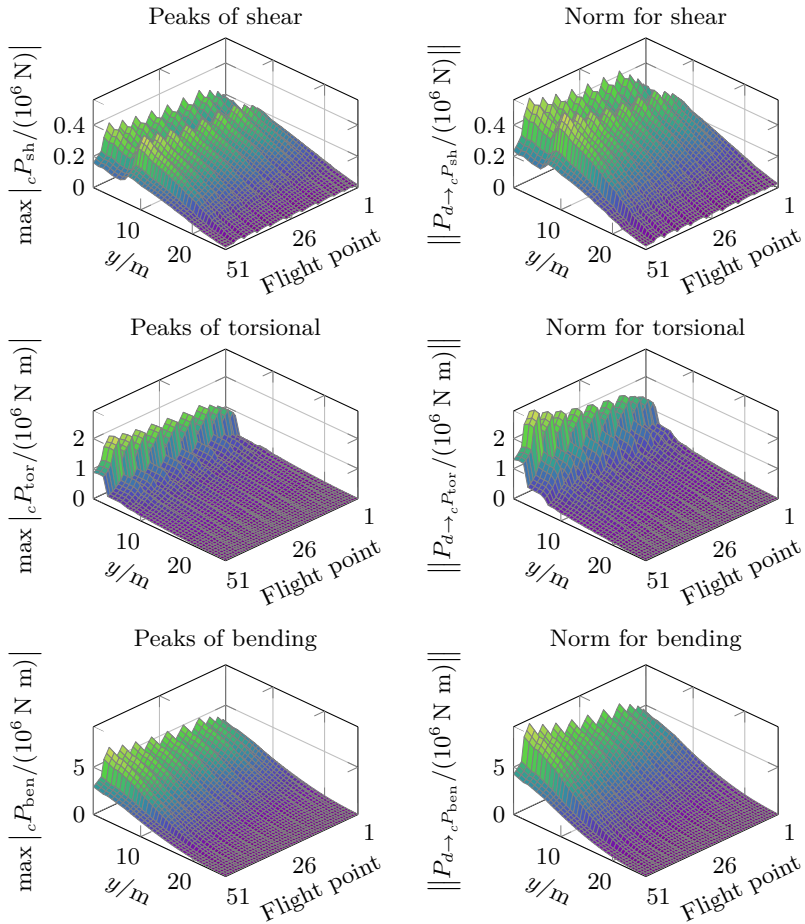


**Figure 5.6:** Peak and norm for the wing loads: The shear, torsional, and bending load peaks from discrete gust simulations are depicted w.r.t. the flight point (cf. Footnote 3, Page 81) and wing span  $y$  in the left column of the figure. In the same fashion, the  $\mathcal{L}_\infty$  norm bound is illustrated in the right column. A similar shape between the peak and the norm can be recognized.

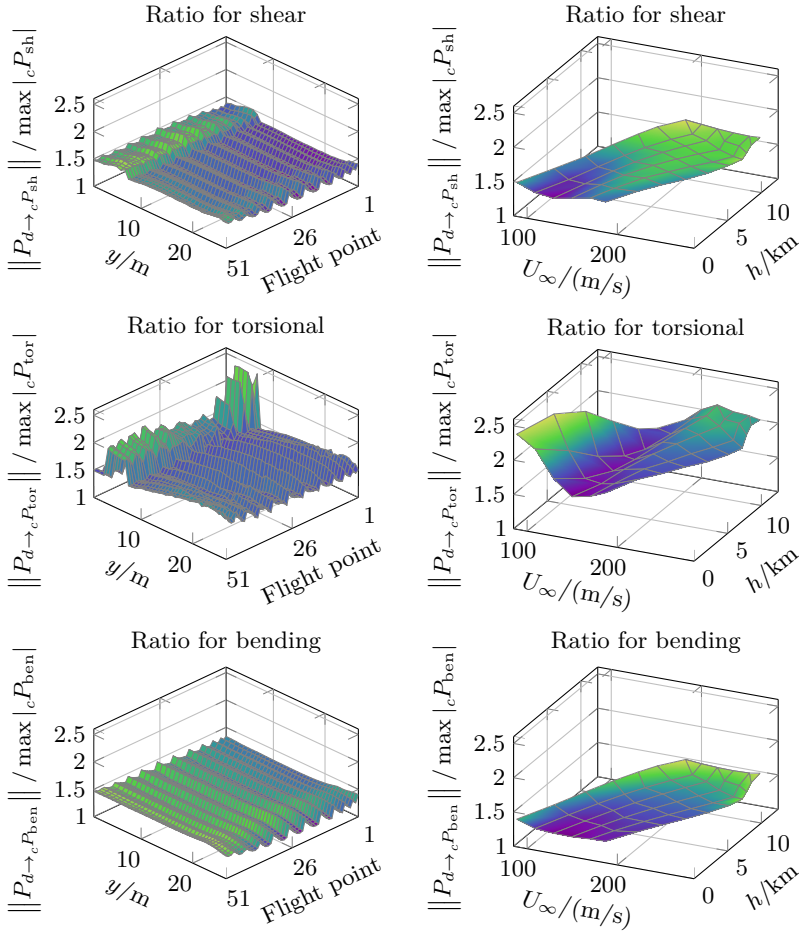


**Figure 5.7:** Norm to peak ratio for the wing loads: In the left column, the ratio of the  $L_\infty$  norm bounds to the peak loads is depicted w.r.t. flight point (cf. [Footnote 3, Page 81](#)). In the right column, the worst ratio of every flight point is plotted regarding to flight speed and altitude.

**Table 5.2:** Statistical evaluation of the norm to peak ratio for the wing loads: The mean, minimum, maximum value and the standard deviation of the norm to peak ratio for the shear, torsional and bending loads are compiled. For the torsional moment, interesting quantities for the outer part of the wing ( $y \geq 6.9$  m) are separately considered.

	Shear	Torsional	Torsional*	Bending
mean	1.38	1.59	1.57	1.35
min	1.26	1.21	1.39	1.19
max	1.62	2.45	1.83	1.49
std	0.07	0.16	0.09	0.06

\* Interesting quantities of the outer part of the wing.

First the bending moment is considered. A trivial – but nevertheless important – result is that the ratio is always greater than one. Consequently, the norm provides indeed an upper bound for the discrete gust peak loads. A mean ratio of 1.35 (cf. Table 5.2) means an average conservatism of 35 % which is a lot in terms of loads analysis. However, since the ratio varies only slightly between 1.19 and 1.49, the conservatism is relatively constant. Further, no striking dependence on the flight point can be recognized in Figure 5.7 (lower right subplot). This result has to be put into the context that the bending peak loads vary between  $2.2 \times 10^4$  N m and  $6.3 \times 10^6$  N m, which is a variation of more than two decades. Consequently, the energy-to-peak gain provides here a guaranteed – but not overly conservative – upper bound for the maximum peak loads, which can be used as an excellent indicator for critical flight points.

Next, the shear force is regarded where similar results are obtained. Here, the mean ratio is slightly greater but the standard deviation is comparable. However, the ratio at the inner part of the wing ( $y < 6.9$  m) is noticeable greater than at the outer wing (see the upper left subplot of Figure 5.7). The reason is discussed in the next subsection.

Finally, the torsional loads are considered. Here, distinct differences between the inner part ( $y < 6.9$  m) and the outer part of the wing can be recognized (cf. Figure 5.7, middle left subplot). The results of the outer part are comparable to the ones for the shear force and the bending moment. On the contrary, the conservatism for the inner wing is severely larger. Here, the worst ratio is 2.44 and the variation w.r.t. the flight point is obviously larger (cf. Figure 5.7, middle right subplot). The reason for this result is discussed in the next subsection.

Nevertheless, the critical flight points obtained by the norm correspond for all three quantities with the actual critical flight conditions. This means that the actual maximum peak loads and the maximum norm occur at the same flight point.

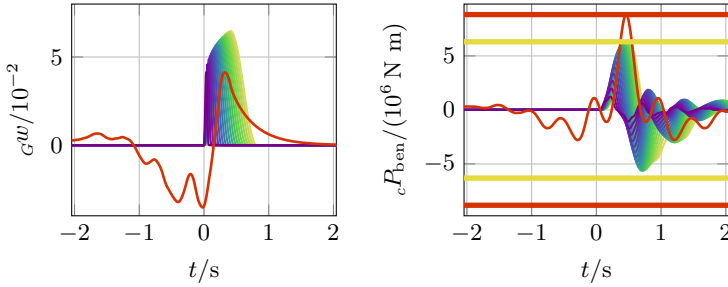


**Figure 5.8:** Worst case excitation for the wing root bending moment: The worst case gust in terms of the energy-to-peak gains (—) is depicted together with the “one-minus-cosine” gusts in the left subplot. The resulting wing root bending moments are illustrated in the right subplot using the same colors. The induced  $\mathcal{L}_2 \rightarrow \mathcal{L}_\infty$  norm (—) is actually reached. The maximum peak of the “one-minus-cosine” gust simulations is indicated by —. The worst case gust is shifted w.r.t. the time s.t. the maximum peaks occur simultaneously.

How this can be used in the further gust loads analysis process is explained in the following [Section 5.3](#).

### 5.2.3 Worst Case Gusts for the Wing Loads

In order to further evaluate the results, worst case excitations for two selected scenarios are computed.

First, the wing root bending moment for the flight point 45 ( $Ma = 0.86$ ,  $h = 9.075$  km) is considered. A worst case disturbance  $d$  with  $\|d\|_{\mathcal{L}_2} = 1$  is computed using [Corollary 3.5](#). The output of the weighting filter due to this excitation represents the worst case gust in terms of the energy-to-peak gain. This worst case gust and the corresponding wing root bending moment are depicted in [Figure 5.8](#) together with results from “one-minus-cosine” gusts simulations. It can be seen that the worst case gust reaches indeed the predicted  $\mathcal{L}_\infty$  norm. An interesting fact is that the worst case gust shape is similar to the excitation during wake vortex encounters (see [Kier, 2011](#); [Kier, 2013](#)). This means that the identified worst case gusts can occur indeed and are thus relevant.

In a second example, the results for the torsional moment at the inner part of the wing are considered. To that end, the worst ratio is considered, which is specified by flight point 3 ( $Ma = 0.32$ ,  $h = 3.368$  km) and  $y = 5.24$  m. A worst case gust is computed in the same way as in the preceding paragraph. The worst case gust and the corresponding torsional moment are illustrated in [Figure 5.9](#). The oscillating nature of the gust is obvious. This leads to the suspicion that for the

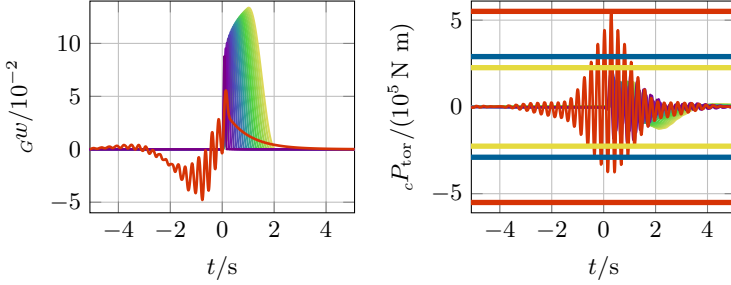


**Figure 5.9:** Worst case excitation for the wing torsional moment: The worst case gust (—) is depicted together with the “one-minus-cosine” gusts in the left subplot. The corresponding wing torsional moments (for  $y = 5.24$  m) are depicted in the right subplot using the same colors. The induced  $\mathcal{L}_2 \rightarrow \mathcal{L}_\infty$  norm (—) is actually reached. Additionally, the incremental loads from a continuous turbulence analysis (—) are illustrated and compared to the peak loads from discrete gust simulations (—). The worst case gust is shifted w.r.t. the time s.t. the maximum peaks occur simultaneously.

considered load case, the continuous turbulence loads are greater than the discrete gust loads and that this also affects the performance analysis.

Consequently, a continuous turbulence analysis is performed and additionally depicted in Figure 5.9. It can be seen that the continuous turbulence loads are higher than the discrete gust loads. This confirms the suspicion. The higher norm to peak ratio of the shear forces at the inner wing can be similarly explained.

A logical question is whether a continuous turbulence load case can easily be distinguished from a “one-minus-cosine” gust case. To that end, the Bode diagram of the considered case is depicted in Figure 5.10 where the weighting filter is already applied. The distinct resonance at  $f = 3.9$  Hz can clearly be recognized which corresponds to the oscillation of the worst case gust. An obvious criterion for a continuous turbulence load case might consequently be the existence of a distinct resonance. However, this is not further examined in the remainder of this thesis but might be worth to be considered in the further research process.

### 5.2.4 Inclusion of Trim Loads

As stated in Section 2.2, the trim loads have to be considered to yield the maximum upper and minimum lower loads. Similar to the normal loads computation process, this can be achieved by superimposing the  $\mathcal{L}_\infty$  norm bound with the trim loads.

**Figure 5.10:** Bode diagram for the wing torsional moment: The distinct resonance (—) is the reason for the overestimation using the energy-to-peak gain. Note that the weighting filter is already applied.

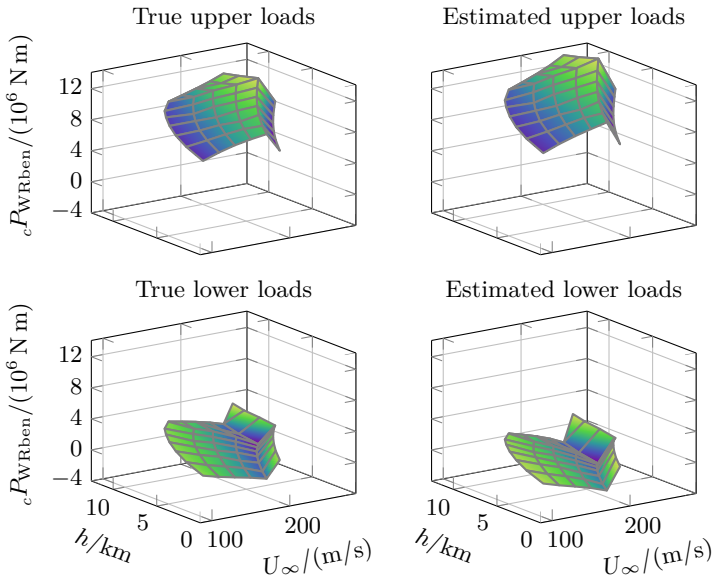
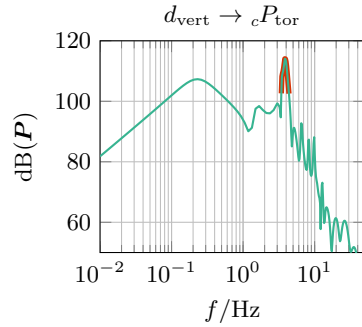


**Figure 5.11:** Superposition of gust and trim loads: The trim loads are superimposed with the peak from “one-minus-cosine” gust simulations (referred to as true loads; left column) and the norm bounds (right column).

This leads to the following bounds for the maximum and minimum loads:

$${}_c\mathbf{P}_{\text{upper}} \leq {}_c\mathbf{P}_{\text{trim}} + \left\| \mathbf{P}_{d \rightarrow {}_cP} \right\|_{\mathcal{L}_2 \rightarrow \mathcal{L}_\infty} \quad (5.11)$$

and

$${}_c\mathbf{P}_{\text{lower}} \geq {}_c\mathbf{P}_{\text{trim}} - \left\| \mathbf{P}_{d \rightarrow {}_cP} \right\|_{\mathcal{L}_2 \rightarrow \mathcal{L}_\infty} . \quad (5.12)$$

This is shown for the wing root bending moment in [Figure 5.11](#). The superposition of the trim loads and the norm bounds provides a good and guaranteed conservative estimation of the true upper and lower limit loads. For simplicity, only the gust increments are considered in the remainder of this thesis.

## 5.2.5 Analysis of the Tail Loads

The tail loads are analyzed in the present section. First, the HTP loads due to vertical gusts are considered. Afterwards, the effect of lateral gusts on the VTP are investigated. Since both results are comparable to the wing loads, the results are not discussed in detail.

### Analysis of the HTP Loads

The analysis is performed in the same way as for the wing loads. The results are depicted in [Figure 5.12](#) and statistical key values are compiled in [Table 5.3a](#). The results correspond well with the ones of the wing loads.

For the shear force and the bending moment, the minimum ratio between norm and peak loads is comparable to the one of the wing loads. On the contrary, the maximum ratio is clearly greater than in case of the wing. These high ratios are caused by exceptions which represent 9.8 % (shear force) and 6.3 % (bending moment) of all cases. At these samples, the continuous turbulence and the “one-minus-cosine” gust loads are very close. However, the critical flight points are still met, i.e., the actual loads peaks and the norm is maximal at the same flight points.

**Table 5.3:** Statistical evaluation of the norm to peak ratio for the HTP and VTP loads: The mean, minimum, maximum value and the standard deviation of the norm to peak ratio for the shear, torsional and bending loads are compiled.

a) HTP loads				b) VTP loads		
	Shear	Torsional	Bending	Shear	Torsional	Bending
mean	1.49	1.73	1.47	2.04	2.08	1.90
min	1.28	1.53	1.28	1.46	1.77	1.39
max	1.80	1.99	1.74	2.32	2.39	2.32
std	0.12	0.08	0.12	0.18	0.09	0.21

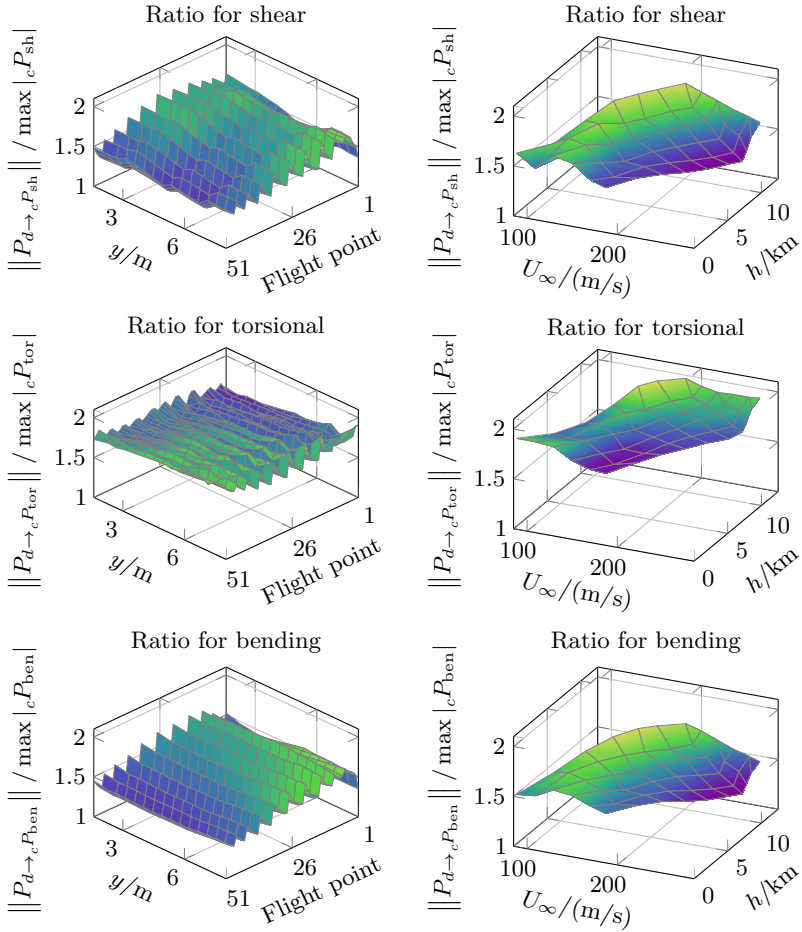


**Figure 5.12:** Norm to peak ratio for the HTP loads: In the left column, the ratio of the  $\mathcal{L}_\infty$  norm bounds to the peak loads is depicted w.r.t. flight point (cf. Footnote 3, Page 81) and the HTP span. In the right column, the worst ratio of every flight point is plotted regarding to flight speed and altitude.

Regarding the torsional loads, it must be said that the ratio is clearly greater than for the other interesting quantities. The reason is that all cases are continuous turbulence loads. Using these loads as a reference, the maximum ratio decreases from 1.99 to 1.69.

### Analysis of the VTP Loads

The analysis results are depicted in [Figure 5.13](#) and statistical values are compiled in [Table 5.3b](#). The ratio between the “one-minus-cosine” gusts and the norm is here in general greater than for the wing and the HTP loads. The reason is that here for all flight points and for all interesting quantities the continuous turbulence loads are greater than the discrete gust loads. Nonetheless, the critical flight points are correctly identified.

## 5.3 Determination of Lower Bounds for Maximum Peak Loads

In the preceding section, it is shown how the worst case energy-to-peak gain can be used to determine an upper bound for discrete gust peak loads. The conservatism of the analysis results was evaluated using simulation results of the complete flight envelope. These simulation results must be expensively determined and are consequently in general not available. In order to estimate the conservatism anyway, lower bounds for the maximum peak loads are instead computed. Here, few critical flight points are identified using the energy-to-peak gain. Afterwards, discrete gust simulations for these few points are carried out and the results are used as lower bounds.

The critical flight points are determined by creating a ranking. To that end, the flight points are sorted for every interesting quantity w.r.t. the  $\mathcal{L}_\infty$  norm bound in descending order. In order to merge the results of all interesting quantities, score points are assigned: for every first rank three points are used, for every second rank two points, and for every third rank one point. The rationale behind this is to weight first ranks stronger than second ranks. Nevertheless, it must be mentioned that this a pure heuristic criterion but it works well in practice.

The ranking results are compiled in [Table 5.4](#). The wing and the HTP loads due to vertical gusts are considered together, while the VTP loads from lateral gusts are treated independently. The top three critical points are considered for the simulations. Hence, the flight points 11, 45, and 17 ( $(Ma, h) \in \{(0.50, 0.000 \text{ km}); (0.86, 9.075 \text{ km}); (0.55, 1.684 \text{ km})\}$ ) are considered for the lateral gust. In case of the vertical gust, the regarded flight points are 45, 40, and 46 ( $(Ma, h) \in \{(0.86, 9.075 \text{ km}); (0.80, 7.926 \text{ km}); (0.86, 10.740 \text{ km})\}$ ).

The two times three flight points are simulated using each twenty gust lengths as described in [Section 2.2](#). The resulting peak loads are used as lower bounds. The results are depicted in [Figure 5.14](#). It can be seen that the lower bounds are

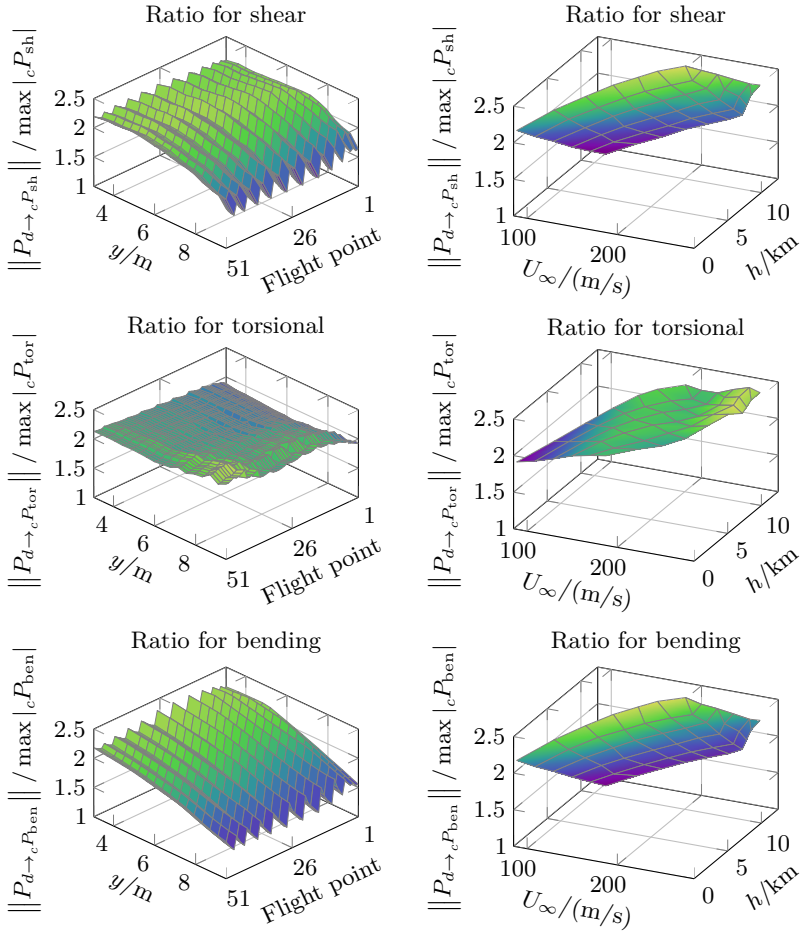


**Figure 5.13:** Norm to peak ratio for the VTP loads: In the left column, the ratio of the  $\mathcal{L}_\infty$  norm bounds to the peak loads is depicted w.r.t. flight point (cf. Footnote 3, Page 81) and the VTP span. In the right column, the worst ratio of every flight point is plotted regarding to flight speed and altitude.

**Table 5.4:** Ranking of the flight points: The most critical flight points (FP) are compiled. The number of first ( $\#1^{\text{st}}$ ), second ( $\#2^{\text{nd}}$ ), and third ranks ( $\#3^{\text{rd}}$ ) and the resulting score points are given. The top three critical points are each considered for the simulations.

a) Lateral gust						b) Vertical gust					
	FP	#1 <sup>st</sup>	#2 <sup>nd</sup>	#3 <sup>rd</sup>	Pnt.		FP	#1 <sup>st</sup>	#2 <sup>nd</sup>	#3 <sup>rd</sup>	Pnt.
1	11	39	2	2	123	45	141	9	8	449	
2	45	11	9	20	71	40	9	81	34	223	
3	17	0	31	9	71	46	11	60	10	163	
4	40	1	9	2	23	35	1	6	74	89	
5	23	0	0	10	10	47	0	5	32	42	
6	35	0	0	8	8	29	0	1	2	4	

very close to the true peak loads. For the wing loads, the lower bounds are actually identical to the peak loads. In case of the HTP and VTP, the underestimation is 7 % and 3 % respectively. Consequently, the purely heuristic criterion fulfills its purpose and there is no need for a more sophisticated criterion.

Finally, the resulting peak loads from a continuous turbulence analysis are additionally depicted in [Figure 5.14](#). For the VTP, it can be seen that the continuous turbulence loads are almost as great as the maximum energy-to-peak gain. This allows to conclude that for VTP, “one-minus-cosine” gusts are not the critical excitation. Hence, despite of the high conservatism of the energy-to-peak gain, the norm represents also here valuable information.

## 5.4 Evaluation and Conclusions

The energy-to-peak gain combined with the weighting filter provides a guaranteed upper bound for the “one-minus-cosine” gust peak loads. It must be clearly noted that the  $\mathcal{L}_\infty$  norm bound is conservative as it can be inferred from the ratio of the norm to the peak loads from simulations. This ratio varies between 1.19 and 2.45. However, in all cases with large conservatism, the continuous turbulence loads are greater than the discrete gust loads. If the maximum of the discrete gust and the continuous turbulence loads is used as reference, the worst ratio is decreased to 1.67.

However, next to the meaning of the absolute value of the ratio, it can be recognized that the ratio varies only slightly w.r.t. the envelope. Note that the maximum peak of one interesting quantity can be more than four times greater than its minimum peak. Next, the peaks of all interesting quantities reach over

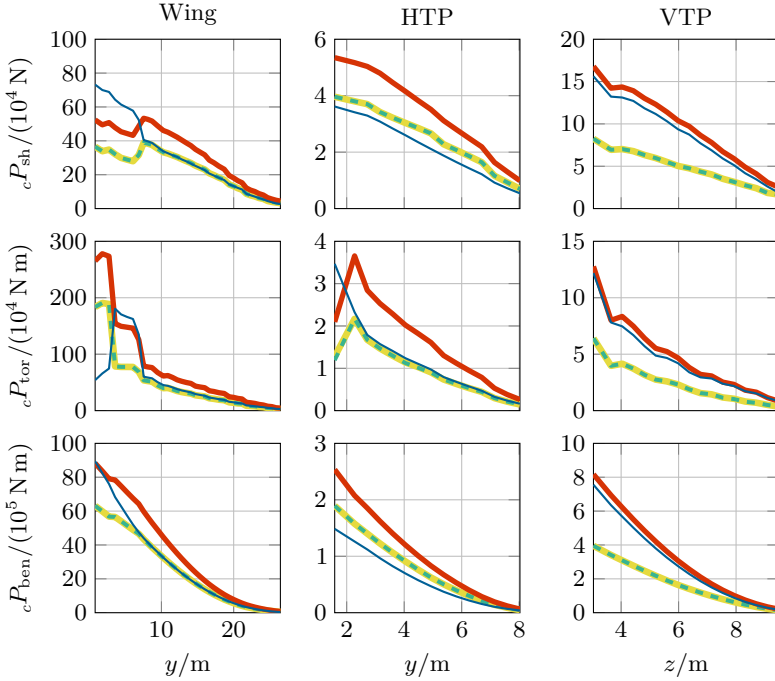


**Figure 5.14:** Lower and upper load bounds: The true peak loads from discrete gust simulations at all flight points are  $\text{—}$ . The lower bounds (obtained by the simulation of three selected flight points) are  $\text{---}$ . Since the true loads and lower bounds are very close, the two lines coincide which appears as  $\text{—}$ . The upper bounds (obtained by the energy-to-peak gain) are  $\text{—}$ . Additionally, the incremental loads from continuous turbulence ( $\text{—}$ ) are depicted.

more than two decades. Compared to this, a variation between 1.19 and 1.67 is relatively small. Consequently, large values of the norm bound correspond to maximum peaks of discrete gust simulations. The  $\mathcal{L}_\infty$  norm bound can hence be used to obtain critical flight points. Standard “one-minus-cosine” gust simulations are next carried out to determine a lower bound for the maximum peak loads. In most cases, the obtained lower bound is identical to the actual peak loads.

The computational effort is compared in Table 5.5. While the simulations for all flight points and both gust directions last 135.9 min, the norm for all outputs at all flight points can be computed within 7.8 min. The simulations of the discrete gusts for the critical flight points last 8.0 min. Thus, the lower and the upper bound for

**Table 5.5:** Required computation times for all discrete gust simulations, the determination of the lower and upper bounds, and for the computation of the continuous turbulence loads.

	<b>Norm</b>	<b>Sim.</b>	<b>Total</b>
	(in minutes)		
Discrete gust			135.9
Lower/upper bnd.	7.8	8.0	15.8
Cont. turbulence			13.8

the peak loads can be obtained in 15.8 min, which is more than eight times faster than conventional discrete gust simulations.

Since the continuous turbulence loads correspond in principle to the  $\mathcal{H}_2$  norm, they can be efficiently computed in a similar fashion in 13.8 min. Taking the maximum of the continuous turbulence loads and of the lower bound for the discrete gust loads results consequently in a very close estimation of the overall peak loads.

In summary, the norm provides a guaranteed upper bound for “one-minus-cosine” gust loads which serves as an excellent indicator for critical flight points. In combination with its efficient computation, the energy-to-peak gain can be used to efficiently determine critical flight points. The simulation of selected critical flight points results in a lower bound for the maximum peak loads.

## 6 Robust Analysis and Control of Gust Loads Models

In the preceding chapter, it is shown that the worst case energy-to-peak gain can be used for the efficient analysis of LTI gust loads models. However, the application of the robust performance analysis framework offers a wide range of new possibilities. One example (presented in [Section 6.1](#)) is the analysis of an LPV model, which is valid in the entire flight. Its number of states is numerically reduced and the influence of the parameter rates is examined. In [Section 6.2](#), the influence of an uncertain damping ratio, one of the most uncertain model parameters, is treated. Another possible application for the worst case energy-to-peak gain is the multidisciplinary design optimization. The benefits of the proposed approach are demonstrated in [Section 6.3](#). It is shown how a gust load alleviation system can be efficiently tuned. Finally, the worst case effects of saturation and sensor uncertainties on the resulting controller are studied in [Section 6.4](#).

### 6.1 LPV Analysis regarding the Flight Envelope

This section provides a similar analysis as in [Chapter 5](#) but instead of analyzing an LTI model for a discrete flight point, an LPV analysis for the complete envelope is performed. This allows to include the transition from one flight point to another and to examine the effects of the parameter rates. As explained in [Section 3.4](#), there are several methods to deal with the resulting infinite dimensional LMIs. Since the model is readily given at discrete flight points (see [Section 2.1](#)), the gridding based approach is most convenient here. On the contrary, an LFR based analysis would require an approximation of the parameter dependence by rational functions. In the considered example, the model input is the vertical gust downwash  ${}_Gw_{\text{vert}}$  and the outputs are the wing root torsional and the bending moment, denoted  ${}_cP_{\text{tor}}$  and  ${}_cP_{\text{ben}}$ . However, because the model order of 1036 states is too high for an LPV analysis, an order reduction is performed before.

The presented analysis extends the results from [Knoblach \(2013b\)](#) and [Knoblach \(2013a\)](#). While in these papers LPV analyses of gust loads models w.r.t. one parameter are described, a two-dimensional parameter space representing the complete flight envelope is considered here.

### 6.1.1 LPV Model Order Reduction

The model from Section 2.1 has originally 1036 states. The number of these states is initially reduced by physical considerations: First, the number of the inputs and outputs is reduced: as input, only the vertical gust is considered and as outputs the wing root torsional and the bending loads. Second, because of the symmetric excitation, only the symmetrical modes need be considered. Both steps lead also to a reduction of the lag state number in the aerodynamic model. After all, this results in a model with 241 states.

LPV models of this size can in principle be analyzed by the methods from Chapter 3. Since these approaches scale badly with the number of states, the resulting SDP has many LMI constraints and decision variables. Solving this SDP can be very time consuming or, due to numerical problems, even impossible. As a remedy, the LPV model is additionally reduced by numerical means. To that end, two fundamentally different methods can be found in the literature. The first method is a generalization of the balance and truncation algorithm for LTI systems (see Wood, Goddard, and Glover, 1996). The advantage of this approach is its theoretical foundation. The drawback is that similar LMIs as for the performance analysis have to be solved. Consequently, the corresponding SDP has the same problem size as the analysis so that this approach is not considered here. The idea of the other method is to perform an LTI model reduction at every grid point. Because the reduced models have different states at different grid points, LPV methods cannot be applied. Consequently, the states are transformed in a second step to approximatively maintain their consistency. Several approaches for doing this can be found in the literature, e.g., Poussot-Vassal and Roos (2012), Adegas et al. (2013) and Theis et al. (2015). In the considered example, a combination of the ideas from Poussot-Vassal and Roos (2012) and from Theis et al. (2015) shows best results. The first step consists of the Krylov based multi model order reduction (Poussot-Vassal and Roos, 2012). In a second step, the reduced LTI models are transformed into a consistent mode-wise canonical representation (Theis et al., 2015). Both steps are briefly explained below.

#### Multi Model Krylov Order Reduction

First, the LTI case is considered. Let  $\mathbf{P}(s) = \mathbf{C}(s\mathbf{I} - \mathbf{A})^{-1}\mathbf{B}$  and  $\hat{\mathbf{P}}(s) = \hat{\mathbf{C}}(s\mathbf{I} - \hat{\mathbf{A}})^{-1}\hat{\mathbf{B}}$  denote the transfer functions of the original model and the reduced model, respectively. The order of  $\mathbf{P}$  is denoted  $n_x$  and the order of  $\hat{\mathbf{P}}$  is  $n_{\hat{x}} \ll n_x$ . The idea of the Krylov order reduction is to find a  $\hat{\mathbf{P}}(s)$  such that

$$\mathbf{P}(\sigma_k) = \hat{\mathbf{P}}(\sigma_k) \quad (6.1)$$

for all so-called interpolation points  $\sigma_k \in \mathbb{C}$  with  $k = 1, \dots, n_\sigma$ . All interpolation points are collected in the vector  $\boldsymbol{\sigma}$ . For simplicity, it is assumed that  $n_\sigma = n_{\hat{x}}$ .<sup>1</sup> If

<sup>1</sup>It should be noted that, in general, the first  $N$  derivatives of  $\mathbf{P}(s)$  and  $\hat{\mathbf{P}}(s)$  can also be considered, i.e.,  $d^l \mathbf{P}(s)/ds^l|_{\sigma_k} = d^l \hat{\mathbf{P}}(s)/ds^l|_{\sigma_k}$  for all  $k = 1, \dots, n_\sigma$  and  $l = 0, \dots, N$ . This leads to additional states in the reduced model.

the interpolation points  $\sigma$  are given, two projection matrices  $V, W \in \mathbb{C}^{n_x \times n_{\hat{x}}}$  are computed s.t. (6.1) is satisfied by the reduced state matrices

$$\hat{A} = W^T A V, \quad \hat{B} = W^T B, \quad \text{and} \quad \hat{C} = C V. \quad (6.2)$$

The computation of  $V$  and  $W$  is not treated here but efficient algorithms are described in the literature (see e.g., Gugercin, 2005).

The remaining problem is the selection of suitable interpolation points which crucially affects the approximation quality. In order to find sensible interpolation points, an  $\mathcal{H}_2$  optimality condition is considered. This condition states that the model error in terms of the  $\mathcal{H}_2$  norm is minimal if and only if  $\sigma_k = -\lambda_k$  for all  $k = 1, \dots, n_{\hat{x}}$  where  $\lambda_k$  is the  $k^{\text{th}}$  eigenvalue of  $\hat{A}$  (see Gugercin, 2005, Theorem 2). This leads to a simple iterative procedure – called iterative SVD-Krylov based model reduction method – to determine an  $\mathcal{H}_2$  optimal approximation given in the following algorithm.

---

**Algorithm 6.1** (Gugercin, 2005; Poussot-Vassal and Roos, 2012):

---

- 1: Make an initial selection for the interpolation points  $\sigma$
  - 2: **repeat**
  - 3:   Compute the projection matrices  $V$  and  $W$  using  $\sigma$
  - 4:   Compute the eigenvalues of the reduced system:  $\lambda = \text{eig}(W^T A V)$
  - 5:   Use  $\sigma = -\lambda$  as new interpolation points
  - 6: **until**  $\sigma$  is converged
  - 7: Compute the reduced system
- 

From an initial guess for the interpolation points, a reduced system matrix is computed (Steps 1 and 3). The eigenvalues of the reduced system matrix are then used as new interpolation points (Steps 4 and 5). This procedure is repeated until  $\sigma$  is converged and the reduced system is computed as defined by Equation (6.2).

The previous algorithm is now extended to grid based LPV models, i.e., the LPV system is represented by  $n_P$  LTI models  $P_i$ . In principle, Algorithm 6.1 can be applied to the LTI model at every grid point. The problem of this approach is that state space bases of the reduced models at different grid points are inconsistent, i.e., the reduced state space matrices are no smooth functions w.r.t. the scheduling parameters. Consequently, it is impossible to interpolate between different grid points or to perform an LPV analysis. As a remedy, Poussot-Vassal and Roos (2012) propose to use the same (or similar) interpolation points at all grid points in order to yield similar projection matrices and hence similar states. The determination of this consistent interpolation points is described in Poussot-Vassal and Roos (2012, Algorithm 3). The complete multi model order reduction algorithm is explained in Poussot-Vassal and Roos (2012, Algorithm 2).

### Transformation into a Mode-wise Canonical Representation

The considered model is reduced from 241 to 20 states as explained above. An inspection of the pole migration of the reduced model shows that its eigenvalues

are indeed smooth functions w.r.t. the parameter space. It is worth to mention that the poles obtained by an LTI balance and truncation order reduction are much more scattered. However, despite of using consistent interpolation points, the state space bases at different grid points are inconsistent in the considered example, i.e., an interpolation of the state space matrices or the application of LPV methods is impossible.

In order to recover state consistency, [Theis et al. \(2015\)](#) propose to transform the reduced model into a mode-wise canonical representation. This means that the state matrix is a block diagonal matrix whose blocks  $\bar{A}_i$  each represent one mode:

$$\bar{A}_i = \begin{cases} \lambda_i & \text{for real eigenvalues} \\ \begin{bmatrix} 0 & 1 \\ -|\lambda_i|^2 & 2 \cdot \text{Re}(\lambda_i) \end{bmatrix} & \text{for complex conjugate eigenvalues.} \end{cases} \quad (6.3)$$

In (6.3),  $\lambda_i$  represents one real eigenvalue or a complex conjugate pole pair of the state matrix. For the oscillatory modes, the resulting states represent each a modal velocity and a modal position. The resulting state space representation is unique apart from a permutation of the blocks. Because this makes an interpolation between two grid points or an LPV performance analysis impossible, the blocks are finally sorted. To this end, a mode tracking using a matching function is applied. See [Theis et al. \(2015\)](#) for details.

It must be clearly noted that despite of the second transformation, the states at different grid points are not the same. However, the corresponding states at varying grid points describe a similar dynamic property. Because the individual modes depend continuously on the parameters, the resulting state space matrices are smooth functions, which allows an interpolation and the application of LPV methods.

### Results for the Model Order Reduction

Before the considered model is reduced, the input and outputs are suitably scaled as follows. First, the weighting filter from [Section 5.1](#) is added. This implies that the relevant frequency range is weighted greater and that the expected disturbance energy is one. In a second step, both outputs are individually normalized by the mean LTI energy-to-peak gain w.r.t. the flight envelope. For numerical reasons, the models are balanced using Matlab's `ssbal` command.

A Bode diagram of the normalized and the reduced model is depicted in [Figure 6.1](#) for five flight points. For most flight points, an appropriate agreement up to the relevant frequency range of 10 Hz can be seen. A root locus plot of the reduced model is depicted in [Figure 6.2](#). In order to represent the two-dimensional parameter space, a reference trajectory is chosen. It can be recognized that the poles migrate smoothly w.r.t. this trajectory.

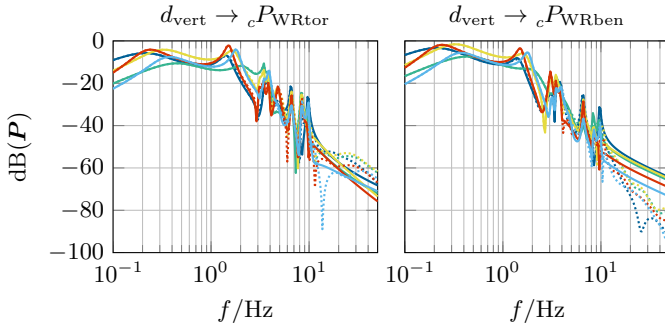


**Figure 6.1:** Bode diagram of the normalized and the reduced model: The normalized model is depicted by the dotted lines (.....) and the reduced by solid ones (—). The different colors correspond to five points of the flight envelope.

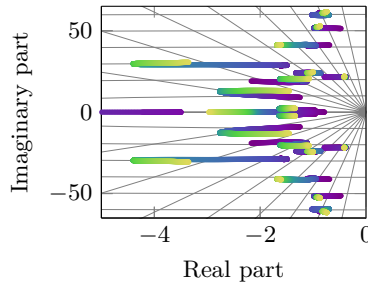


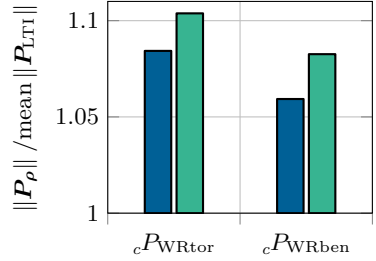
**Figure 6.2:** Root locus plot of the reduced model: The color corresponds to a representative trajectory through the two-dimensional parameter space.

### 6.1.2 LPV Analysis – Results and Conclusions

An LPV performance analysis of the reduced model – in terms of the worst case energy-to-peak gain – is performed using [Algorithm 3.1](#). It must be noted that every output is considered individually, i.e., for every output, an SDP has to be solved. To reduce the numerical sensitivity of the SDPs, every output is scaled with its maximum LTI norm.

The scheduling parameter  $\rho$  consists of the flight speed  $U_\infty$  and the altitude  $h$ :  $\rho = [U_\infty \ h]^T$ . For numerical reasons, both parameters are scaled to the interval  $[-1, 1]$ . Although the variation of these parameters is in general very slowly, their effect is examined using extremely overestimated rate bounds. In case of the flight speed, a rate bound of 1.5 times the gravitational acceleration is used:

**Figure 6.3:** Analysis results of the LPV gust loads model: The ratio of the LPV norm to the average LTI norm is depicted by  $\blacksquare$ . Additionally, the result from the validation points are illustrated by  $\blacksquare$ .



$|\dot{U}_\infty|1.5g = 14.8 \text{ m/s}^2$ . For the altitude  $h$ , the maximum flight speed is considered, i.e.,  $|\dot{h}| \leq 265.56 \text{ m/s}$ . For the Lyapunov matrix function, a second order polynomial is used as basis function:

$$\mathbf{X}_0(\mathbf{p}) = \mathbf{X}_0 + U_\infty \mathbf{X}_{11} + h \mathbf{X}_{12} + U_\infty^2 \mathbf{X}_{21} + h^2 \mathbf{X}_{22} + U_\infty h \mathbf{X}_{23}. \quad (6.4)$$

The analysis results are illustrated in Figure 6.3 where the ratio of the LPV norm to the average LTI norm for both outputs is depicted. The ratio is 1.08 and 1.06 for the torsional and bending moment, respectively. This means that the LPV results are close to the LTI ones.

In order to validate the grid based analysis results, a set of 2500 randomly distributed points inside the flight envelope is created. The corresponding state space matrices are obtained by interpolation. Algorithm 3.2 is then applied to the new grid points. The results of this validation step are additionally depicted in Figure 6.3. They are consistent with the initial analysis. Consequently, there is hardly any risk of missing a critical flight point.

The benefit of the LPV analysis is that by only one analysis an upper bound of the gust loads can be computed for the complete parameter space. Additionally, this analysis includes the transition from one flight point to another. Hence, the risk of missing a critical flight point or transition effects can be almost excluded. However, despite of an enormous overbounding of the parameter rate bounds, the LPV results are very close the maximum LTI norm. Consequently, the transition effects are – at least in the considered example – very small. This implies that the common practice to analyze LTI gust loads models at multiple grid points is valid. Since the LPV analysis requires further an order reduction and is numerical sensitive, the numerically robust and cheap LTI approach from Chapter 5 is the more reasonable option in most practical cases.

However, the successful LPV analysis can also be understood as a validation of the LPV order reduction. Inconsistent states or discontinuities in the state space matrix functions would have probably caused large discrepancies between the LTI and the LPV analysis. This means also that the LPV framework might be an interesting option for the synthesis of self-scheduled gust load alleviation controllers.

## 6.2 Influence of the Damping Ratio

The damping ratio is one of the most uncertain parameters in aeroelastic models. In order to determine reliable information how it affects the gust loads, the damping ratio is considered as uncertainty in the present section and an LFR based robust performance analysis is performed. The uncertain damping matrix is defined as

$${}_{hh}\mathbf{B}_{\text{unc}} = \Delta_{\mathbf{B}} {}_{hh}\mathbf{B}_{\text{nom}} \quad (6.5)$$

and two cases,  $\Delta_{\mathbf{B}} \in [1/2, 2]$  and  $\Delta_{\mathbf{B}} \in [1/4, 4]$ , are considered. The analysis is pursued at the example of the wing torsional and bending moments for several cuts along the wing span. The treated flight point is specified by  $Ma = 0.9$  and  $h = 1.24$  km.

In order to yield a reasonable problem size, the resulting LFR model is numerically reduced by methods available in the Enhanced LFR Toolbox (see [Hecker, Varga, and Magni, 2005](#)). To that end, every output is scaled by the nominal energy-to-peak gain. The order of the reduced model  $\hat{\mathbf{P}}$  is chosen iteratively s.t. the absolute model distance

$$\sup_{s, \Delta_{\mathbf{B}}} \left\| \mathbf{P}(s, \Delta_{\mathbf{B}}) - \hat{\mathbf{P}}(s, \Delta_{\mathbf{B}}) \right\|_2 \quad (6.6)$$

is smaller than 0.2 %. The number of states of the reduced model varies between 41 and 53. The size of the uncertainty matrix is always 18. A comparison of the Bode diagrams and simulation results of the original and the reduced model show an excellent agreement.

Despite of the known conservatism, a constant Lyapunov matrix is chosen for the LFR based analysis. The reason is that a parameter dependent one would increase the overall LFR size from 18 to over 100. For relaxing the infinite dimensional LMIs by the Full Block S-Procedure, diagonal multipliers are used.

The analysis results are illustrated in [Figure 6.4](#), where the ratio of the robust norm to the nominal norm is depicted w.r.t. several cuts along the wing span. It can be seen that for most of the cuts, the ratio of the robust to the nominal norm is smaller than 5 % even for the greater uncertainty. Exceptions are some cuts between the engine and the fuselage where the norm for the torsional moment is increased by over 15 %. In order to estimate the conservatism induced by the robust analysis, the maximum LTI norm w.r.t. five equidistantly spaced values of  $\Delta_{\mathbf{B}}$  is additionally depicted. These results are a bit smaller but agree in general well with the robust performance analysis results. The difference can be explained by the fact that a constant Lyapunov matrix is used.

The analysis results show that the damping ratio affects only a few outputs. The most concerned output is the torsional moment at the cut marked in [Figure 6.4](#). This cut is considered for a more detailed analysis. “One-minus-cosine” gust simulations are performed for  $\Delta_{\mathbf{B}} \in \{1/4, 1, 4\}$  using the unreduced model. The simulation

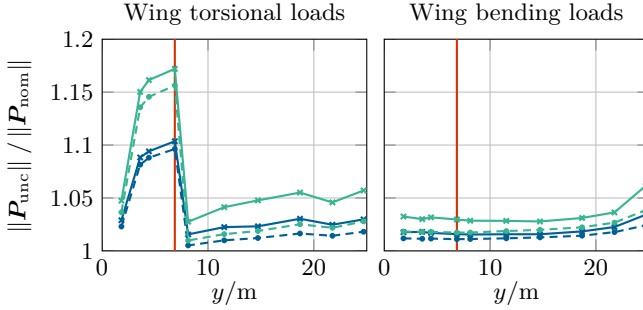


**Figure 6.4:** Analysis results for an uncertain damping ratio: The ratio of the robust to the nominal norm is depicted w.r.t. the wing span. Results for the smaller uncertainty are plotted by  $\text{---}+$  and for the larger one by  $\text{---}+$ . Additionally, results for the maximum LTI norm w.r.t. five equidistantly spaced values for  $\Delta_B$  are depicted in the same fashion. The line  $\text{---}+$  corresponds to the smaller and  $\text{---}+$  to the greater uncertainty. The cut marked by  $\text{---}$  is considered for a detailed study.

results correspond well with the results from the robust performance analysis as it can be seen in Figure 6.5. The actual torsional peak loads are indeed affected by the damping ratio. A reduction of the damping ratio leads to an amplification of the peak by 10%. On the contrary, the bending moment is (as indicated by the norm) hardly affected by different damping ratios. Note that the variation of the simulation peaks w.r.t. the damping ratio corresponds well to the variation of the LTI norms.

In order to emphasize the correlation between the simulation and the performance analysis results, the amplification of the norms and of the simulation peaks due to the uncertainty is depicted in Figure 6.6. It can be seen that for the torsional moment, the robust and the maximum LTI norm are increased by a factor of 1.17 and 1.16. Similarly, the maximum peak from the simulations is increased by a factor of 1.11. In case of the bending moment, on the contrary, all metrics are changed only slightly by less than 4%.

The preceding example demonstrates how a robust performance analysis can be used to examine the effects of uncertainties. An increased robust norm for one output indicates that the considered output is sensitive towards the uncertainty. Performing an LTI analysis of the considered output with different values for the uncertainties allows next to identify critical parameter combinations. If the worst LTI norm is close to the guaranteed upper bound from the robust performance analysis, the risk of missing a critical parameter combination can be almost excluded. The identified critical parameter combinations can finally be analyzed by simulations.

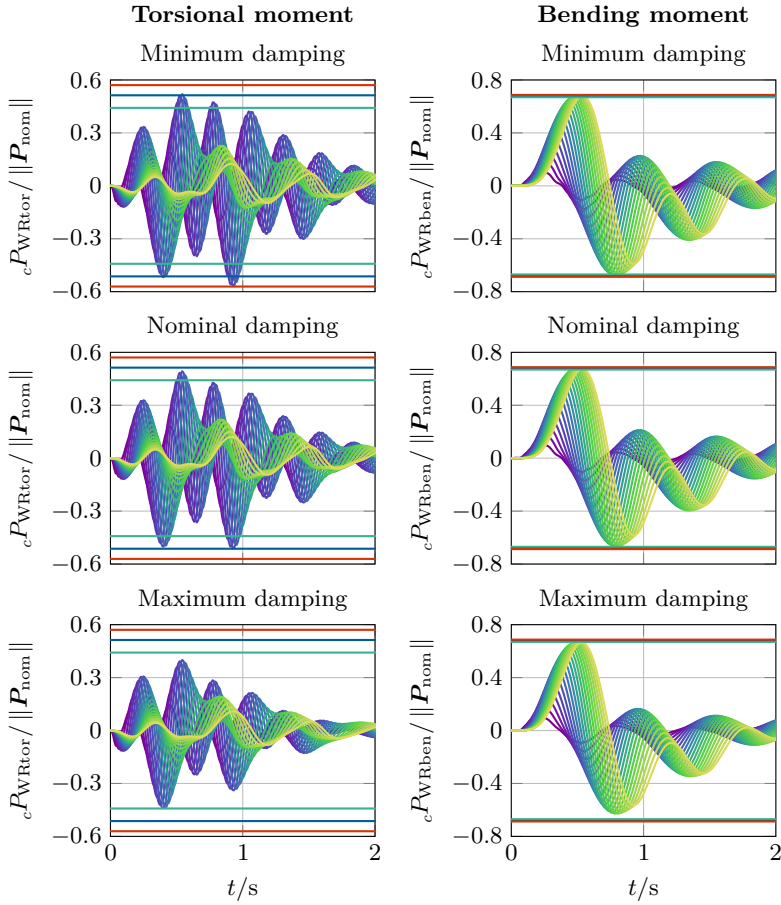
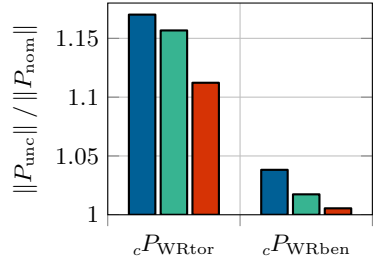


**Figure 6.5:** Simulation results for three damping ratios: One quarter of the nominal damping is used in the first row, the nominal damping in the middle row and four times the nominal damping in the lower row. The torsional moment is depicted in the left column and the bending moment in the right one. In order to compare the different plots, the maximum peak for the minimum damping (—), for the nominal damping (—), and for the maximum damping (—) is shown in all plots.

**Figure 6.6:** Amplification of the norm and the peak caused by the uncertainty: The ratio of the robust performance analysis to the nominal analysis is depicted by  $\blacksquare$ . In the same way, the maximum LTI norm ( $\blacksquare$ ) is illustrated. The ratio between the peak corresponding to the minimal damping and to the nominal damping is  $\blacksquare$ .



The obvious next step is to use independent uncertainties for the damping ratios of all modes. Unfortunately, the corresponding results are extremely conservative. It is supposed that the reason for this is the use of a constant Lyapunov matrix. Experiments with parameter dependent Lyapunov matrix functions turn out to be intractable. However, progress in SDP solvers or recent results on the approximation of SDPs by linear programs (Ahmadi and Parrilo, 2014; Peni and Pfifer, 2015) might solve this limitation in the near future.

## 6.3 Design of a Gust Load Alleviation System

Modern aircraft are often equipped with a gust load alleviation system in order to reduce structural loads. The reasons are that this allows to decrease fatigue loads and to improve passenger comfort. In case of small failure probabilities, it is even possible to reduce the safety factor for the open loop loads. Hence, it is possible to decrease the aircraft weight which results in a reduction of fuel consumption. Clearly, such flight controller systems are safety critical. Consequently, the controller must be carefully designed and analyzed. The benefit of the robust performance analysis as a tool for doing this is demonstrated in the present and following section. However, it is not the aim to find a gust load alleviation system featuring all of its many demands but to demonstrate the usefulness of the proposed analysis methods.

### 6.3.1 Scenario and Aircraft Model

The vertical gusts downwash  $Gw_{vert}$  is considered as disturbance and the elevator  $xu_{ele}$  as well as symmetrically deflected ailerons  $xu_{ail}$  are used as control inputs. The performance outputs  $e$  are the wing root torsional  $cP_{WRtor}$  and bending  $cP_{WRben}$  moments, the vertical acceleration  ${}_b\dot{w}$  and the pitch rate  ${}_b\dot{q}$ . The vertical acceleration and the pitch rate are used as measurement for the feedback path. Additionally, a light detection and ranging (LiDAR) sensor measures the gust wind field at the aircraft nose which is used for a disturbance feedforward control.

The considered aircraft model has hence three inputs and four outputs. In order to accelerate the controller tuning, the resulting model (229 states) is numerically reduced. To that end, a frequency weighted balance and truncation reduction (see Zhou, 1993) is applied which allows to weight the relevant frequency range stronger. The gust input is weighted by  $(s + 9.2)/(s + 1000)$  which is an adaption of the first order weighting filter from Section 5.1: the filter is modified such that it is invertible. For the control inputs, the weighting filter  $5(s + 50)/(s + 1000)$  is used which corresponds to the actuator dynamics. Every output is scaled with its (open loop) worst case energy-to-peak gain of the weighted model. The order reduction is performed using Matlab's `reduce` function (see *Robust Control Toolbox: User's Guide* 2011). The original model and the reduced model with 27 states are depicted in Figure 6.7. A reasonable agreement in the relevant frequency range up to 10 Hz can be recognized.

### 6.3.2 Controller Structure and Tuning

The controller is tuned by minimizing the energy-to-peak gains of the closed loop using the interconnection depicted in Figure 6.8. The weighting filter from Section 5.1 is applied to the vertical gust input  $Gw_{\text{vert}}$ . Additionally, actuator and sensor models are used. The control inputs are connected to the first order low pass filter  $G_{\text{act}}$

$$\begin{bmatrix} x_{\text{ele}} \\ x_{\text{ail}} \end{bmatrix} = \begin{bmatrix} \frac{20}{s+20} & 0 \\ 0 & \frac{20}{s+20} \end{bmatrix} \mathbf{u}, \quad (6.7)$$

which is used as an actuator model. As already mentioned, a LiDAR sensor is used for a disturbance feedforward control. Because LiDAR sensors are notably perturbed, noise  $d_{\text{noise}}$  is added as a second disturbance input. The gain  $N = 0.01$  is used to affect the influence of the disturbance feedforward path. For the feedback path, the measurements are the vertical acceleration and the pitching rate. Finally, a sensor model  $G_{\text{sen}}$

$$\mathbf{y} = \begin{bmatrix} \frac{10}{s+10} & 0 & 0 & \frac{0.1}{s+10} \\ 0 & \frac{100}{s+100} & 0 & 0 \\ 0 & 0 & \frac{100}{s+100} & 0 \end{bmatrix} \begin{bmatrix} Gw_{\text{vert}} \\ {}_b q \\ {}_b \dot{w} \\ d_{\text{noise}} \end{bmatrix} \quad (6.8)$$

is added. Note that the slower time constant for the LiDAR sensor is motivated by a weaker measurement quality.

A simple proportional controller is used. The six gains are tuned by multi objective optimization. The objective is to minimize the ratio loop energy-to-peak gains from the closed loop to the open for all performance outputs. This is shown by

$$O_i = \frac{\|P_{\text{CL}, d \rightarrow e_i}\|_{\mathcal{L}_2 \rightarrow \mathcal{L}_\infty}}{\|P_{\text{OL}, d \rightarrow e_i}\|_{\mathcal{L}_2 \rightarrow \mathcal{L}_\infty}} \quad (6.9)$$

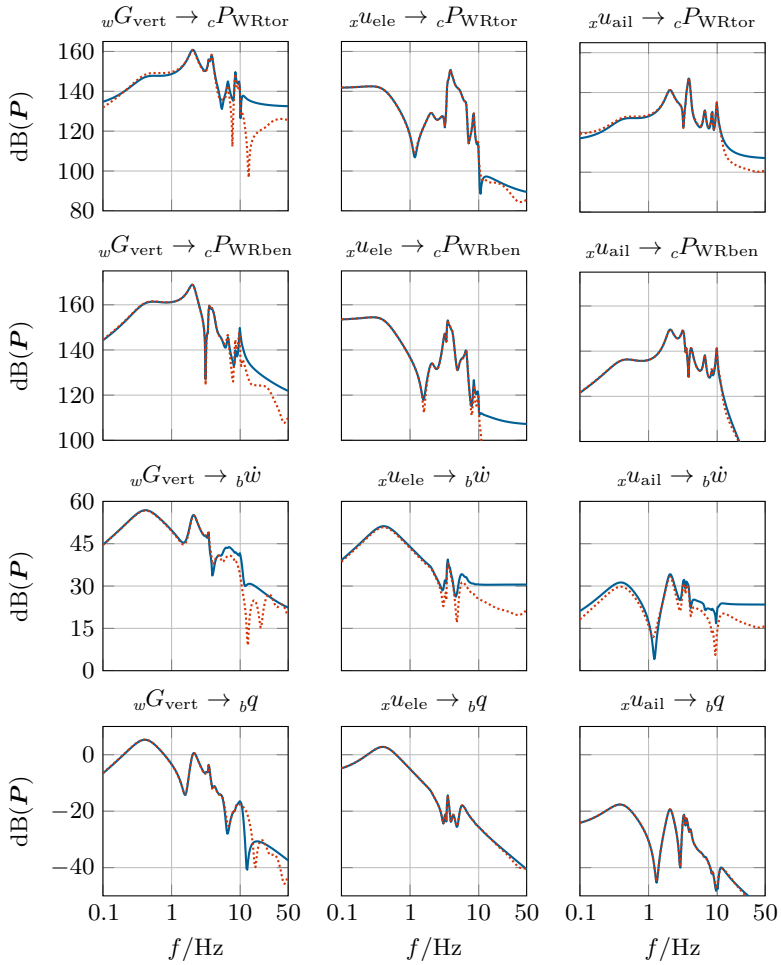


**Figure 6.7:** Bode Diagram of the original model (.....) and the reduced model (—). A reasonable agreement in the relevant frequency range up to 10 Hz can be seen.

where  $i$  represents the four performance outputs respectively. This tuning goal is hence a measure for the load reduction due to the gust load alleviation system. The overall cost function  $V$  is defined as the sum of squares of all  $O_i$ :

$$V = O_{cP_{\text{WRtor}}}^2 + O_{cP_{\text{WRben}}}^2 + O_{b^{\dot{u}_z}}^2 + O_{b^{\dot{u}_\alpha}}^2. \quad (6.10)$$

In order to avoid too excessive control commands, constraints for the elevator and aileron deflections are added:

$$C_i: \frac{\|P_{\text{CL}, d \rightarrow u_i}\|_{\mathcal{L}_2 \rightarrow \mathcal{L}_\infty}}{25^\circ} < 1.7. \quad (6.11)$$

In (6.11), the  $25^\circ$  represents the maximum possible elevator and aileron deflection. The allowed exceedance of the saturation limit by a factor of 1.7 is chosen due to the conservatism of the norm base analysis and to allow for a high performance controller.<sup>2</sup> The overall optimization problem reads as

$$\min_K V \quad \text{s.t. } C_{x^{\dot{u}_{\text{ele}}}} \text{ and } C_{x^{\dot{u}_{\text{ail}}}} \text{ are satisfied.} \quad (6.12)$$

The rationale of this optimization setup is that this criterion can be computed much more efficiently than the performing “one-minus-cosine” gust simulations. Further, as demonstrated in [Chapter 5](#), it serves as an excellent indicator for maximum loads.

The optimization is performed with MOPS (see [Joos et al., 2002](#)) using a gradient free pattern search algorithm. Because this leads to excellent results, no genetic algorithm or gradient based optimization algorithms are applied in addition.

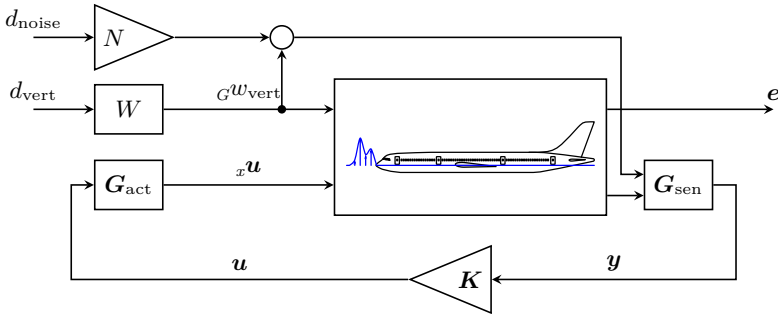


**Figure 6.8:** Analysis interconnection for the controller tuning.

<sup>2</sup>The effects of possible exceedances are discussed in the next section.

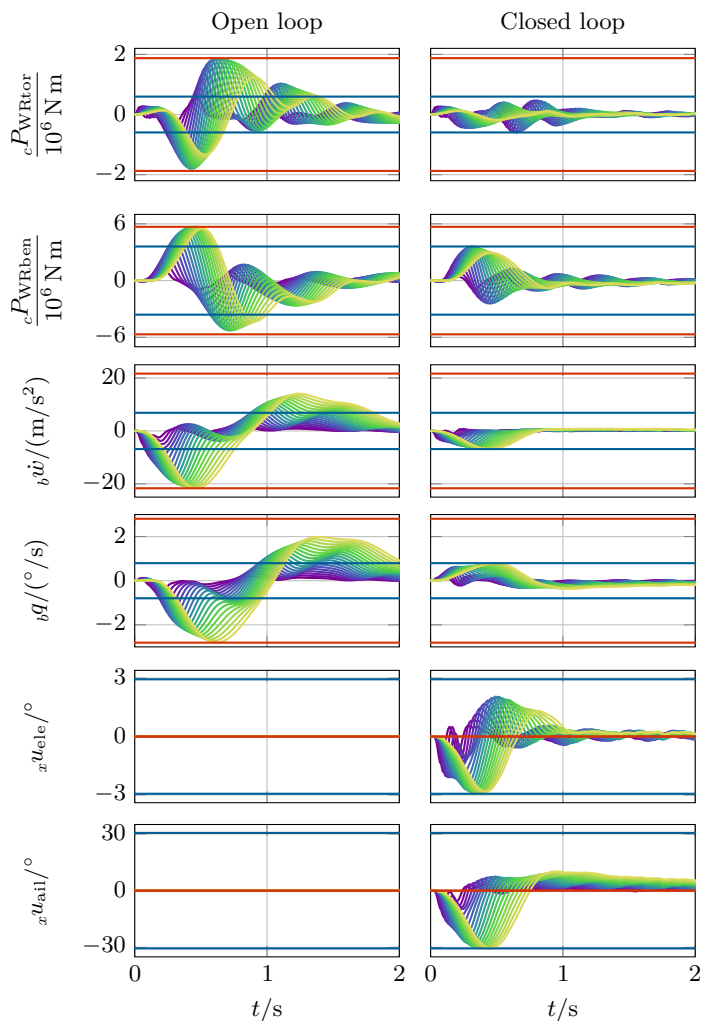
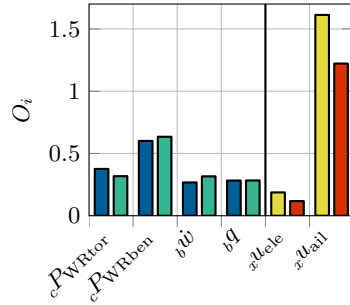


**Figure 6.9:** Simulation results for the open (left column) and the closed loop (right column): In order to compare the different plots, the maximum peak from the open loop (—) and from the closed loop (—) are shown in all plots. A distinct load reduction can be seen.

**Figure 6.10:** Comparison of the tuning and simulation results: The relative reduction of the energy-to-peak gain (■) agrees perfectly with the peak reduction from the “one-minus-cosine” gust simulations (■). Further, the predicted maximum control commands (■) deliver safe estimates for actual command peaks (■) during the simulations. (The command values are normalized with  $25^\circ$ .)



### 6.3.3 Results and Conclusions

“One-minus-cosine” gust simulations of the open and the closed loop are compared in Figure 6.9. It can clearly be seen that the peaks of all performance outputs are distinctly decreased. The relative reduction of the energy-to-peak gain as well as the reduction of the peaks from the simulations are illustrated in Figure 6.10. The predicted improvement by the energy-to-peak gain agrees perfectly with the actual load reduction. The differences vary between  $-5\%$  and  $+6\%$ .

Further, the predicted exceedance of the control commands w.r.t. the saturation limit agrees well with the simulation results and the overestimation corresponds well with the results from Chapter 5. Hence, suitable demand values can be used to specify the acceptable exceedance of the saturation limit. It is finally worth to mention that comparable simulation results are obtained using the full model.

As already mentioned, this controller will probably not feature all demands of a gust load alleviation system. In order to yield a system supporting all requirements, a multi objective optimization scheme as e.g., developed in Saupe (2013) can be set up. For example, the resulting controller may lead to increased loads close to the ailerons or at the HTP. In order to avoid such effects, the objective function can be extended to cover these quantities, too. The desired load alleviation at single cuts can then be achieved by choosing suitable demand values. Similarly, to improve the robustness of the controller, a multi model approach and classical robustness criteria can be included in the optimization. Further, the described procedure can also be used to tune more complex control structures such as an  $\mathcal{H}_\infty$  or an LPV controller instead of a simple proportional controller.

Such an optimization is beyond the scope of this thesis. However, since the energy-to-peak gain can be much more effectively determined than peaks from “one-minus-cosine” gust simulations, the optimization is distinctly accelerated. The excellent results of the presented example demonstrate clearly the usefulness and efficiency of this approach.

## 6.4 Analysis of a Saturated Gust Load Alleviation System

Gust load alleviation systems are commonly subject to saturation and uncertainties. Since these systems are safety critical, the effects of such perturbations on stability and performance must be carefully evaluated. How this can be done using the IQC framework is demonstrated using the example of the above designed controller.

As already mentioned, the considered gust load alleviation system is subject to saturation. Additionally, an uncertainty resulting from the LiDAR sensor is considered. The resulting analysis interconnection is depicted in [Figure 6.11](#). The difference to the tuning interconnection (cf. [Figure 6.8](#)) is the added saturation block and the uncertainty which replaces the noise input.

First, the case without the uncertainty of the LiDAR sensor is considered. The simulation results are depicted in [Figure 6.12](#). Although the aileron position is saturated, the controller performance is only marginally decreased. However, because this allows no general valid conclusions, a robust performance analysis based on the IQC theory from [Chapter 4](#) is performed. The saturation blocks for both commands are described each by a Popov, a Sector and a Zames-Falb IQC. The Zames-Falb IQC is parameterized by the first order low pass filter

$$H(s) = \frac{1}{s+1}. \quad (6.13)$$

In order to reduce conservatism, the iterative local analysis as described in [Algorithm 4.1](#) is performed. Note that two sector constraints for the two saturation blocks are considered during the iteration.

The robust performance analysis results are illustrated in [Figure 6.13](#) and compared to the simulation peaks. In contrast to the simulation results, the saturation leads, especially in case of the two moments, to a notable degeneration

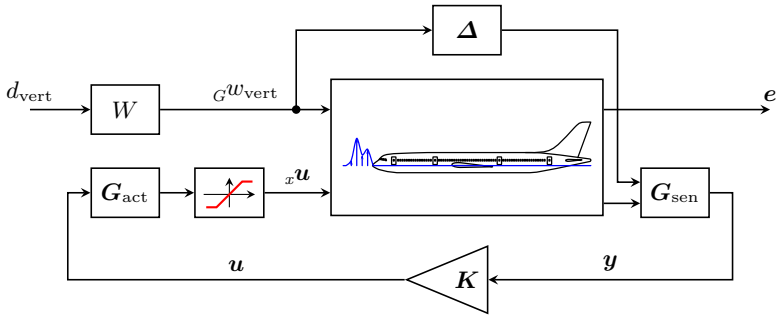


**Figure 6.11:** Interconnection for the robustness analysis.

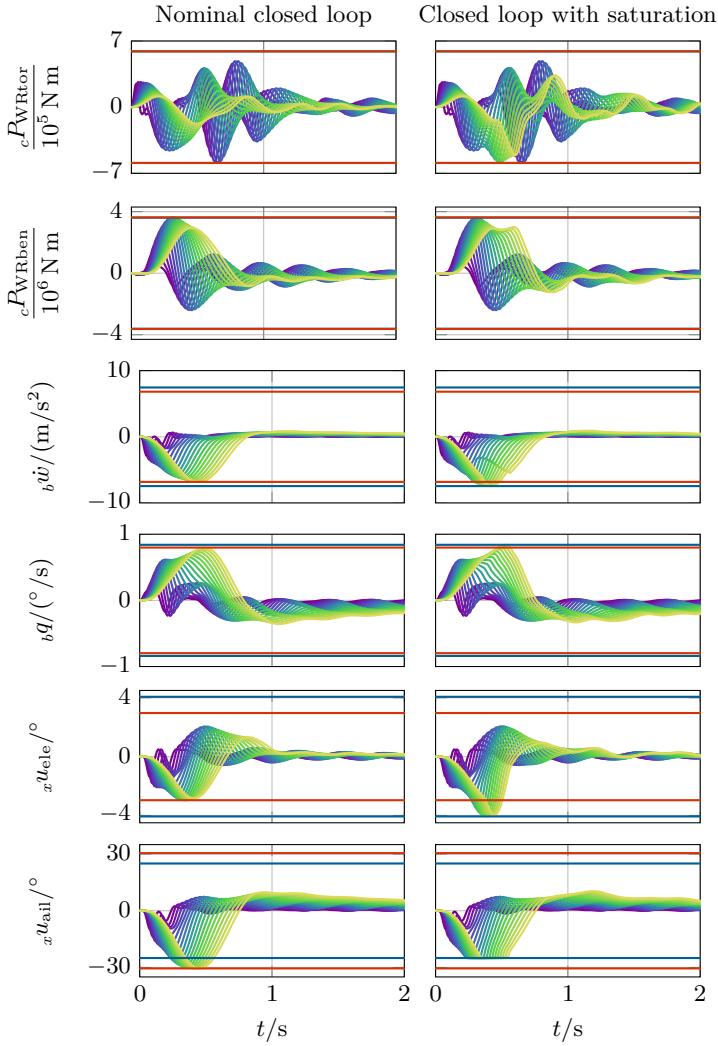


**Figure 6.12:** Simulation results without (left column) and with saturation (right column): In order to compare the different plots, the maximum peaks without (—) and with saturation (—) are shown in all plots.

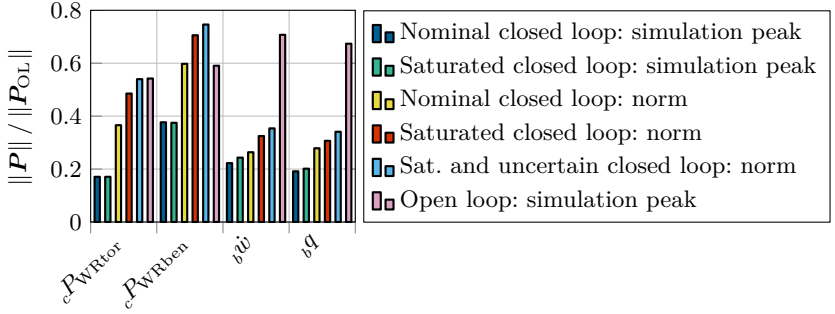


**Figure 6.13:** Robust performance analysis results: The peaks from simulation using the open loop model ( $\square$ ) and the closed loop model without ( $\square$ ) and with ( $\square$ ) saturation are compared to different norm bounds. The norm bounds for the nominal closed loop is depicted by  $\square$ . The robust norm without sensor uncertainty is illustrated by  $\square$  and with sensor uncertainty by  $\square$ . All results are normalized by the open loop norm.

of the worst case energy-to-peak gain. However, except for the wing root bending moment, all robust norms are smaller than the peaks from the open loop simulations. Consequently, the robust performance analysis proves that these loads are declined by the gust load alleviation system. Regarding to the wing root bending moment, the value of the robust norm is 71 % of the nominal open loop. This indicates that the designed gust load alleviation system will robustly decrease the wing root bending loads, too.

In a second example, an uncertainty is added to the LiDAR sensor:

$$\Delta = \bar{\Delta} + 1 \quad \text{with} \quad \|\bar{\Delta}\|_{\mathcal{L}_2 \rightarrow \mathcal{L}_2} < 0.2. \quad (6.14)$$

For the analysis, this uncertainty is described by the IQC from [Example 4.1](#). The results are additionally depicted in [Figure 6.13](#) and are only slightly greater than the results including only the saturation. Consequently, the controller is robust against the inaccurate measurements of the LiDAR sensor.

Summarizing, it can be said that the IQC based analysis proves robust stability and performance of the controller against saturation and measurement uncertainty. This validates the proposed design method from the preceding section.

# 7 Summary and Outlook

## 7.1 Summary

In this thesis, a new approach for the computation of worst case gust loads based on the robust performance analysis framework is proposed. It is shown that the worst case energy-to-peak gain can be used to compute a guaranteed upper bound for loads due to “one-minus-cosine” gust excitations. The computational efficiency of this approach allows an extremely fast identification of critical flight points which is then considered for a more detailed analysis. The effectiveness of the proposed approach is demonstrated at various examples: nonlinear and uncertain models are considered and the design of a gust load alleviation system is presented.

The robust performance analysis requires to solve an SDP with infinite dimensional LMI constraints. A benchmark of three techniques for dealing with such constraints from the literature is presented. The benchmark shows that a gridding of the parameter space and an LFR based analysis leads to consistent results. On the contrary, the polytopic approach is – independent of any overbounding during the modeling – very conservative for the considered examples. Another result is the distinct reduction of conservatism by parameter dependent Lyapunov matrix functions.

The analysis of saturated LPV systems using IQCs is treated. An iterative procedure to refine local IQCs is proposed to reduce the conservatism of the analysis results. The effectiveness of this approach is examined at the example of a two-dimensional thin airfoil in combination with a gust load alleviation system. The results indicate conservatism for low saturation limits. However, for larger saturation limits, the proposed method converges to the nominal case and is hence only slightly conservative.

After elaborating the required theory, the energy-to-peak gain is used to compute upper bounds for “one-minus-cosine” gust loads. To this end, a weighting filter is designed, which is able to create all admissible “one-minus-cosine” gusts with unit energy. Consequently, the energy-to-peak gain represents a guaranteed upper bound for the maximum gust loads. The analysis results are compared to simulation results in a comprehensive case study using an aircraft model of industrial complexity. The outcome is evaluated by considering the ratio of the norm bound to the simulation peaks. Since this ratio varies between 1.19 and 1.67, it must be clearly noted that performance analysis results are conservative. However, beside of the actual bound for the gust loads, the energy-to-peak gain serves as an excellent indicator for critical flight points. Standard “one-minus-cosine” gust simulations at these critical

flight points are carried out to determine a lower bound for the maximum peak loads. The obtained lower bounds are identical to or slightly smaller than the actual peak loads. The benefit of this approach becomes clear if the computational effort is considered: the computation for both the lower and upper bound is eight times faster than the conventional gust loads analysis.

The application of the robust performance analysis framework for gust loads analysis offers a wide range of new possibilities. Examples for such applications are presented in the last chapter of this thesis. First, the analysis of an LPV model, covering the entire flight envelope, allows to compute a bound for gust loads by only one analysis. This analysis covers also the transition from one flight point to another. Next, the structural damping ratio is considered as an uncertainty and an LFR based analysis is performed. This analysis allows to identify outputs which are sensitive to the uncertainty without any risk of missing a critical parameter combination. Finally, the tuning and worst case analysis of a gust load alleviation system is presented. It is shown that the energy-to-peak gain serves as an excellent optimization criterion. Robust stability and performance of the resulting controller against saturation and sensor uncertainties is then proved by an IQC based analysis.

All results show the effectiveness of this new approach. Critical flight points can be reliably identified without any risk of missing a critical parameter combination. Because of the computational efficiency, the proposed approach is especially convenient during a multidisciplinary design optimization.

## 7.2 Outlook

As already mentioned, the robust performance analysis framework offers a wide range of applications for gust loads analysis. These include the LFR based analysis with many uncertainties. However, the resulting SDPs turn out to be numerically intractable or yield extremely conservative results. A reduction of this conservatism and the inclusion of unstructured uncertainties is hence considered as a relevant research field. As already mentioned, interesting approaches for doing this lead to very complex SDPs which are then the major limitation. Such SDPs are approximated by linear or second order cone programs in recent works of [Ahmadi and Parrilo \(2014\)](#) and [Peni and Pfifer \(2015\)](#). Because these problems can be solved much more efficiently, complex problems with more uncertainties might become tractable. Regarding to the IQC based analysis of saturated systems, the conservatism could be reduced by including further IQCs such as the ones described in [Fang, Lin, and Rotea \(2008\)](#) and [Materassi and Salapaka \(2009\)](#). Another interesting idea is to use IQCs in order to enforce further constraints on the disturbance. For example, to use not only an energy bound but also a peak bound on the disturbance might reduce the conservatism of the analysis. Finally, specialized algorithms for the synthesis of optimal energy-to-peak gain controllers are described in e.g., [Rotea \(1993\)](#). These algorithms are an interesting option for the design of a gust load alleviation system.

# A Convex Optimization

Some fundamental facts of convex optimization are presented below in order provide the basis for the results in [Chapter 3](#). The following treatise is adapted from [Boyd et al. \(1994\)](#), [Scherer and Weiland \(2004\)](#) and [Pfifer \(2013\)](#) where further details can be found.

In general, a convex optimization problem is given by

$$\min_{\mathbf{x}} f_0(\mathbf{x}), \quad \text{s.t.} \quad f_i(\mathbf{x}) > 0 \quad \forall i = 1, \dots, n. \quad (\text{A.1})$$

In (A.1), the functions  $f_i: \mathbb{R}^n \rightarrow \mathbb{R}$  with  $i = 0, \dots, n$  are convex. An essential feature of convex optimization problems is that any local optimum is the global optimum. Consequently, such problems can be efficiently solved. A precise definition of convex sets and functions is given in the remainder of this appendix.

## A.1 Convex Sets and Functions

### Convex Sets

A set  $\mathcal{P}$  is convex if any line segment between two points  $\mathbf{p}_1, \mathbf{p}_2 \in \mathcal{P}$  is also contained in  $\mathcal{P}$ . This means that

$$\rho \mathbf{p}_1 + (1 - \rho) \mathbf{p}_2 \in \mathcal{P} \quad (\text{A.2})$$

if  $\mathbf{p}_1, \mathbf{p}_2 \in \mathcal{P}$  and  $0 \leq \rho \leq 1$ .

A point

$$\mathbf{p} = \sum_{i=1}^n \rho_i \mathbf{p}_i \quad (\text{A.3})$$

with  $\sum_{i=1}^n \rho_i = 1$  and  $\rho_i \geq 0 \quad \forall i = 1, \dots, n$  is called a convex combination of the points  $\mathbf{p}_1, \mathbf{p}_2, \dots, \mathbf{p}_n$ . This allows to define the convex hull of a given set  $\mathcal{P}_0$  as

$$\mathcal{P} = \text{conv}(\mathcal{P}_0) = \left\{ \sum_{i=1}^n \rho_i \mathbf{p}_i \left| \sum_{i=1}^n \rho_i = 1 \text{ and } \rho_i \geq 0 \quad \forall i = 1, \dots, n \right. \right\}. \quad (\text{A.4})$$

If the set  $\mathcal{P}_0$  is finite,  $\mathcal{P}$  represent a convex polytope. The notation  $\text{vert}(\mathcal{P})$  is used to refer to the vertices of the convex hull of  $\mathcal{P}$ .

### Convex Functions

A function  $f: \mathcal{P} \rightarrow \mathbb{R}$  is called convex if  $\mathcal{P}$  is convex and if for any  $\mathbf{p}_1, \mathbf{p}_2 \in \mathcal{P}$  and any  $0 \leq \rho \leq 1$

$$f(\rho \mathbf{p}_1 + (1 - \rho) \mathbf{p}_2) \leq \rho f(\mathbf{p}_1) + (1 - \rho) f(\mathbf{p}_2). \quad (\text{A.5})$$

If the function  $-f(\mathbf{p})$  is convex,  $f$  is called concave. Note that an affine function is simultaneously convex and concave.

Convexity of a function  $f$  can be investigated using its Hesse matrix

$$\frac{\partial^2}{\partial \mathbf{p}^2} f(\mathbf{p}) = \begin{bmatrix} \frac{\partial^2}{\partial p_1^2} f & \cdots & \frac{\partial^2}{\partial p_1 \partial p_n} f \\ \vdots & \ddots & \vdots \\ \frac{\partial^2}{\partial p_1 \partial p_n} f & \cdots & \frac{\partial^2}{\partial p_n^2} f \end{bmatrix}. \quad (\text{A.6})$$

If  $\frac{\partial^2}{\partial \mathbf{p}^2} f(\mathbf{p})$  is positive semidefinite for all  $\mathbf{p} \in \mathcal{P}$ , the function  $f$  is convex.

## A.2 Bounds for Convex Functions with Polytopic Parameter Spaces

The following propositions are used for relaxing infinite dimensional LMIs with affine parameter dependences.

**Proposition A.1** (Scherer and Weiland, 2004): *Consider a convex function  $f: \mathcal{P} \rightarrow \mathbb{R}$  with  $\mathcal{P} = \text{conv}(\mathcal{P}_0)$ . Then,  $f(\mathbf{p}) \leq 0$  for all  $\mathbf{p} \in \mathcal{P}$  if and only if  $f(\mathbf{p}) \leq 0$  for all  $\mathbf{p} \in \mathcal{P}_0$ .*

A relaxed version of the above proposition requires only multi convexity of the function  $f$ , i.e.,

$$\frac{\partial^2 f}{\partial p_i^2} \geq 0 \quad \forall i = 1, \dots, n_p. \quad (\text{A.7})$$

This leads to the following proposition.

**Proposition A.2** (Gahinet, Apkarian, and Chilali, 1996; Scherer and Weiland, 2004): *Consider a multi-convex function  $f: \mathcal{P} \rightarrow \mathbb{R}$  with  $\mathcal{P} = \text{conv}(\mathcal{P}_0)$ . Then,  $f(\mathbf{p}) \leq 0$  for all  $\mathbf{p} \in \mathcal{P}$  if and only if  $f(\mathbf{p}) \leq 0$  for all  $\mathbf{p} \in \mathcal{P}_0$ .*

In many cases, Propositions A.1 and A.2 can be analogously used for the definiteness of matrix functions.

**Proposition A.3** (Scherer and Weiland, 2004): *Consider a matrix function  $F: \mathcal{P} \rightarrow \mathbb{S}$  with  $\mathcal{P} = \text{conv}(\mathcal{P}_0)$ . Assume that*

$$F(\mathbf{p}) < 0 \quad \forall \mathbf{p} \in \mathcal{P}_0 \quad (\text{A.8})$$

holds, which implies that

$$\mathbf{f}(\mathbf{p}) = \mathbf{x}^T \mathbf{F}(\mathbf{p}) \mathbf{x} < 0 \quad \forall \mathbf{p} \in \mathcal{P}_0 \text{ and any } \mathbf{x} \neq 0. \quad (\text{A.9})$$

If  $\mathbf{f}(\mathbf{p})$  is a (multi) convex function – which depends on  $\mathbf{F}(\mathbf{p})$  – [Proposition A.1](#) (or [Proposition A.2](#)) can be applied and (A.9) implies that

$$\mathbf{x}^T \mathbf{F}(\mathbf{p}) \mathbf{x} < 0 \quad \forall \mathbf{p} \in \mathcal{P}. \quad (\text{A.10})$$

Since  $\mathbf{x}$  is arbitrary, this implies that

$$\mathbf{F}(\mathbf{p}) < 0 \quad (\text{A.11})$$

holds for all  $\mathbf{p} \in \mathcal{P}$ .

It should be noted that in general, the convexity of  $\mathbf{f}(\mathbf{p})$  can hardly be checked. However, a special case occurs when  $\mathbf{F}(\mathbf{p})$  is an affine function. Then,  $\mathbf{f}(\mathbf{p})$  is affine and hence also convex.

## A.3 Schur Complement

Finally, the following lemma (found e.g., in [Boyd et al., 1994](#)) allows to transform a nonlinear constraint into an LMI. It is required for proofs in this thesis.

**Lemma A.4** (Schur complement): *Using the three matrices  $\mathbf{X} \in \mathbb{H}^n$ ,  $\mathbf{Y} \in \mathbb{H}^m$ , and  $\mathbf{Z} \in \mathbb{C}^{n \times m}$ , the following three conditions are equivalent:*

$$\mathbf{Y} > 0 \text{ and } \mathbf{X} - \mathbf{Z}\mathbf{Y}^{-1}\mathbf{Z}^* > 0, \quad (\text{A.12a})$$

$$\mathbf{X} > 0 \text{ and } \mathbf{Y} - \mathbf{Z}^*\mathbf{X}^{-1}\mathbf{Z} > 0, \quad (\text{A.12b})$$

$$\begin{bmatrix} \mathbf{X} & \mathbf{Z} \\ \mathbf{Z}^* & \mathbf{Y} \end{bmatrix} > 0. \quad (\text{A.12c})$$



## B State Space Matrices of Aeroelastic System for the Benchmarks

### B.1 State Space Matrices for the Benchmark in Section 3.5

The state space matrices regarding the benchmark of techniques for dealing with infinite dimensional LMIs (Section 3.5) are explicitly presented below. Note that only the uncertain parameters of the benchmarks are considered. The other parameters are already evaluated using the values from Table 3.1. Due to limited space, the free stream velocity  $U_\infty$  is shortened by  $U$ .

$$A = \begin{bmatrix} -0.13 U & 0 & 0 & 0 & 0 & 0 & 0 & 0 & 0 \\ 0 & -1.0 U & 0 & 0 & 0 & 0 & 0 & 0 & 0 \\ 0 & 0 & 0 & 0 & 1.0 & 0 & 0 & 0 & 0 \\ 0 & 0 & 0 & 0 & 0 & 1.0 & 0 & 0 & 0 \\ 0.029 U & 0.029 U & -0.97 \frac{k_h}{m} & -0.066 U^2 & 0.21 - 0.35 U^2 & -0.3 U & -0.31 U & 0.048 U^2 & 0.048 U^2 \\ 0.016 U & 0.016 U & 0.83 \frac{k_h}{m} + 0.11 U^2 & 0.6 U^2 - 1.0 & 0.52 U & -0.16 U & -0.082 U^2 & -0.082 U^2 \\ 0 & 0 & 0.0043 U & -0.091 U & 0 & 0 & -0.045 U & 0 & 0 \\ 0 & 0 & 0.38 U & -1.0 U & 0 & 0 & 0 & -0.3 U & 0 \end{bmatrix}$$

$$B = \begin{bmatrix} 0.82 U \\ 6.3 U \\ 0 \\ 0 \\ 0 \\ 0 \\ 0 \\ 0 \\ 0 \end{bmatrix} \quad C = \begin{bmatrix} 0 & 0 & k_h & 0 & 0 & 0 & 0 & 0 \\ 0 & 0 & 0 & 0.25 m & 0 & 0 & 0 & 0 \end{bmatrix} \quad D = \begin{bmatrix} 0 \end{bmatrix}$$

The order of the states is two aerodynamic lag states for the Theodorsen function, four states from the EOM, and two other lag states for the Sears function. The EOM states are  $h$ ,  $\alpha$ ,  $\dot{h}$ , and  $\dot{\alpha}$ . The input is the gust velocity and the outputs are the spring forces.

### B.2 State Space Matrices for the IQC Example in Section 4.3

The state space matrices for the IQC examples in Section 4.3 are explicitly given below. The open loop case without actuator dynamics and without weighting filter is considered. Note that only the uncertain parameters of the benchmarks are

considered and the other parameters are already evaluated using the values from Table 4.1. Due to limited space, the free stream velocity  $U_\infty$  is shortened by  $U$ .

$$A = \begin{bmatrix} -0.13 U & 0 & 0 & 0 & 0 & 0 & 0 & 0 \\ 0 & -1.0 U & 0 & 0 & 0 & 0 & 0 & 0 \\ 0 & 0 & 0 & 0 & 1.0 & 0 & 0 & 0 \\ 0 & 0 & 0 & 0 & 0 & 1.0 & 0 & 0 \\ 0.029 U & 0.029 U & -0.066 U^2 - 0.039 & 0.21 - 0.35 U^2 & -0.3 U & -0.31 U & 0.048 U^2 & 0.048 U^2 \\ 0.016 U & 0.016 U & 0.11 U^2 + 0.033 & 0.6 U^2 - 1.0 & 0.52 U & -0.16 U & -0.082 U^2 & -0.082 U^2 \\ 0 & 0 & 0.0043 U & -0.091 U & 0 & 0 & -0.045 U & 0 \\ 0 & 0 & 0.38 U & -1.0 U & 0 & 0 & 0 & -0.3 U \end{bmatrix}$$

$$B = \begin{bmatrix} 0.82 U & -0.45 U^2 \\ 6.3 U & 0.41 U^2 \\ 0 & 0 \\ 0 & 0 \\ 0 & 0 \\ 0 & 0 \\ 0 & 0 \\ 0 & 0 \end{bmatrix} \quad C = \begin{bmatrix} 0 & 0 & 0.04 & 0 & 0 & 0 & 0 & 0 \\ 0 & 0 & 0 & 0.25 & 0 & 0 & 0 & 0 \end{bmatrix} \quad D = \begin{bmatrix} 0 & 0 \\ 0 & 0 \end{bmatrix}$$

The order of the states is two aerodynamic lag states for the Theodorsen function, four states from the EOM, and two other lag states for the Sears function. The EOM states are  $h$ ,  $\alpha$ ,  $\dot{h}$ , and  $\dot{\alpha}$ . The inputs are the gust velocity and the flap angle. The outputs are the spring forces.

# Bibliography

- Adegas, F. D. et al. (2013). “Reduced-Order LPV Model of Flexible Wind Turbines from High Fidelity Aeroelastic Codes”. In: *Conference on Control Applications*. IEEE (cit. on p. 96).
- Ahmadi, A. A. and P. A. Parrilo (2014). “Towards Scalable Algorithms with Formal Guarantees for Lyapunov Analysis of Control Systems via Algebraic Optimization”. In: *Conference on Control Applications*. IEEE (cit. on pp. 104, 114).
- Albano, E. and W. P. Rodden (1969). “A Doublet-Lattice Method for Calculating Lift Distributions on Oscillating Surfaces in Subsonic Flows”. In: *AIAA Journal* 7.7, pp. 279–285 (cit. on p. 12).
- Apkarian, P. and D. Noll (2006). “Nonsmooth  $\mathcal{H}_\infty$  Synthesis”. In: *IEEE Transactions on Automatic Control* 51.1, pp. 71–86 (cit. on p. 70).
- Bisplinghoff, R., H. Ashley, and R. Halfman (1955). *Aeroelasticity*. Dover Pubns (cit. on pp. 8, 10, 14, 46, 47, 68).
- Borglund, D. (2003). “Robust Aeroelastic Stability Analysis Considering Frequency-Domain Aerodynamic Uncertainty”. In: *Journal of Aircraft* 40.1, pp. 189–193 (cit. on p. 75).
- Borglund, D. (2004). “The  $\mu$ - $k$  Method for Robust Flutter Solutions”. In: *Journal of Aircraft* 41.5, pp. 1209–1216 (cit. on pp. 3, 75).
- Borglund, D. (2005). “Upper-Bound Flutter Speed Estimation Using the  $\mu$ - $k$  Method”. In: *Journal of Aircraft* 42.2, pp. 555–557 (cit. on p. 75).
- Boyd, S. et al. (1994). *Linear Matrix Inequalities in System and Control Theory*. SIAM Studies in Applied Mathematics. Society for Industrial and Applied Mathematics (cit. on pp. 26, 27, 115, 117).
- Control System Toolbox: User’s Guide* (2013). MathWorks. Natick, MA: The MathWorks, Inc (cit. on p. 81).
- Dettori, M. (2001). “LMI techniques for control with application to a Compact Disc player mechanism”. PhD thesis. Technische Universiteit Delft (cit. on pp. 26, 27, 29, 31–33, 35, 37, 39, 43, 44).
- Dettori, M. and C. Scherer (1998). “Robust Stability and Analysis for Parameter and Dependent and Systems using Full Block S-Procedure”. In: *Conference on Decision and Control*. IEEE (cit. on p. 29).

- Dullerud, G. and F. Paganini (2000). *A Course in Robust Control Theory*. Springer-Verlag (cit. on p. 35).
- EASA CS-25. *Certification Specifications and Acceptable Means of Compliance for Large Aeroplanes*, CS-25 (2013). European Aviation Safety Agency. (Cit. on pp. 3, 8, 17, 18, 21).
- FAA FAR-25. *Airworthiness Standards: Transport Category*, FAR Part 25 (2013). Federal Aviation Administration. (Cit. on pp. 3, 8).
- Fang, H., Z. Lin, and M. Rotea (2008). “On IQC approach to the analysis and design of linear systems subject to actuator saturation”. In: *System & Control Letters* 57, pp. 611–619 (cit. on pp. 65, 114).
- Fidkowski, K. J. et al. (2008). “Stochastic Gust Analysis Techniques for Aircraft Conceptual Design”. In: *Multidisciplinary Analysis and Optimization Conference*. AIAA (cit. on p. 24).
- Gahinet, P., P. Apkarian, and M. Chilali (1996). “Affine Parameter-Dependent Lyapunov Functions and Real Parametric Uncertainty”. In: *IEEE Transactions on Automatic Control* 41.3, pp. 436–442 (cit. on pp. 42, 116).
- Gugercin, S. (2005). “An iterative SVD-Krylov based method for model reduction of large-scale dynamical systems”. In: *Conference on Decision and Control and European Control Conference*. IEEE (cit. on p. 97).
- Guyan, R. J. (1965). “Reduction of stiffness and mass matrices”. In: *AIAA Journal* 3.2, pp. 380–380 (cit. on p. 8).
- Hecker, S. (2006). “Generation of low order LFT-Representations for Robust Control Applications”. PhD thesis. Fakultät für Elektrotechnik und Informationstechnik der Technischen Universität München (cit. on pp. 29, 30).
- Hecker, S., A. Varga, and J.-F. Magni (2005). “Enhanced LFR-Toolbox for MATLAB”. In: *Aerospace Science and Technology* 9, pp. 173–180 (cit. on pp. 30, 101).
- Hedman, S. G. (1966). *Vortex lattice method for calculation of quasi steady state loadings on thin elastic wings in subsonic flow*. Tech. rep. DTIC Document (cit. on p. 11).
- Hindi, H. and S. Boyd (1998). “Analysis of Linear Systems with Saturation using Convex Optimization”. In: *Conference on Decision and Control*. IEEE, pp. 903–908 (cit. on p. 65).
- Hoblitz, F. M. (1988). *Gust loads on aircraft: concepts and applications*. AIAA (cit. on p. 8).
- Hu, T. and Z. Lin (2002). “Exact Characterization of Invariant Ellipsoids for Single Input Linear Systems Subject to Actuator Saturation”. In: *IEEE Transactions on Automatic Control* 47.1, pp. 164–169 (cit. on p. 65).

- Hu, T., Z. Lin, and B. M. Chen (2002). “An analysis and design method for linear systems subject to actuator saturation and disturbance”. In: *Automatica* 38, pp. 351–359 (cit. on p. 65).
- IEA 2009. *Transport, Energy and CO<sub>2</sub>*. International Energy Agency. (Cit. on p. 1).
- Joos, H. et al. (2002). “A multi-objective optimisation-based software environment for control systems design”. In: *Conference on Computer-Aided Control Systems Design*. IEEE (cit. on pp. 78, 107).
- Karpel, M., B. Moulin, and P. Chen (2003). “Dynamic Response of Aero-servoelastic Systems to Gust Excitation”. In: *International Forum on Aeroelasticity and Structural Dynamics* (cit. on p. 16).
- Khodaparast, H. H. and J. E. Cooper (2013). “Worst Case Gust Loads Prediction Using Surrogate Models and System Identification Methods”. In: *Structures, Structural Dynamics, and Materials Conference*. AIAA (cit. on p. 24).
- Khodaparast, H. et al. (2011). “Rapid Prediction of Worst Case Gust Loads”. In: *Structures, Structural Dynamics and Materials Conference*. AIAA (cit. on p. 24).
- Khodaparast, H. et al. (2012). “Efficient Worst Case “1-Cosine” Gust Loads Prediction”. In: *Journal of Aeroelasticity and Structural Dynamics* 2.2, pp. 33–54 (cit. on p. 24).
- Kier, T. (2011). “An Integrated Loads Analysis Model Including Unsteady Aerodynamic Effects for Position and Attitude Dependent Gust Fields”. In: *International Forum on Aeroelasticity and Structural Dynamics* (cit. on pp. 8, 10, 13, 16, 85).
- Kier, T. (2013). “An Integrated Loads Analysis Model for Wake Vortex Encounters”. In: *International Forum on Aeroelasticity and Structural Dynamics* (cit. on p. 85).
- Knoblauch, A. (2013a). “Robust Performance Analysis Applied to Gust Loads Computation”. In: *Journal of Aeroelasticity and Structural Dynamics* 3.1, pp. 39–50 (cit. on pp. 5, 75, 95).
- Knoblauch, A. (2013b). “Robust Performance Analysis Applied to Loads Computation of Flexible Aircraft”. In: *International Forum on Aeroelasticity and Structural Dynamics* (cit. on pp. 5, 75, 95).
- Knoblauch, A., H. Pfifer, and P. Seiler (2015). “Worst Case Analysis of a Saturated Gust Loads Alleviation System”. In: *Guidance, Navigation, and Control Conference*. AIAA (cit. on pp. 4, 67).
- Knoblauch, A. et al. (2013). “Robust Performance Analysis: a Review of Techniques for Dealing with Infinite Dimensional LMIs”. In: *International Conference on Control Applications Part of the Multi-Conference on Systems and Control*. IEEE (cit. on pp. 4, 25).

- Kroll, N. and C.-C. Rossow (2012). “Digital-X: DLR’s Way Towards the Virtual Aircraft”. In: *NIA CFD Conference* (cit. on p. 8).
- Lind, R. and M. Brenner (1999). *Robust aeroservoelastic stability analysis*. Springer Verlag (cit. on pp. 3, 75).
- Löfberg, J. (2004). “YALMIP: A Toolbox for Modeling and Optimization in MATLAB”. In: *Conference on Computer Aided Control System Design*, pp. 284–289 (cit. on pp. 27, 48).
- Marcos, A. and G. Balas (2004). “Development of Linear-Parameter-Varying Models for Aircraft”. In: *AIAA Journal of Guidance, Control, and Dynamics* 27.2, pp. 218–228 (cit. on p. 28).
- Materassi, D. and M. V. Salapaka (2009). “Less conservative absolute stability criteria using Integral Quadratic Constraints”. In: *American Control Conference*. IEEE, pp. 113–118 (cit. on p. 114).
- Megretski, A. (2010). “KYP Lemma for Non-Strict Inequalities and the Associated Minimax Theorem”. In: *arXiv* (cit. on p. 56).
- Megretski, A. and A. Rantzer (1997). “System Analysis via Integral Quadratic Constraints”. In: *IEEE Transactions on Automatic Control* 42.6, pp. 819–830 (cit. on pp. 26, 55–59, 61, 62, 65).
- Peni, T. and H. Pfifer (2015). “Analysis of Large Scale Parameter-Varying Systems by using Scaled Diagonal Dominance”. submitted to the European Control Conference (cit. on pp. 104, 114).
- Pfifer, H. and S. Hecker (2010). “Generation of Optimal Linear Parametric Models for LFT-Based Robust Stability Analysis and Control Design”. In: *IEEE Transactions on Control Systems Technology* 19, pp. 118–131 (cit. on pp. 28, 30).
- Pfifer, H. (2013). “LPV/LFT Modeling and its Application in Aerospace”. PhD thesis. Technische Universität München (cit. on pp. 28, 30, 32, 39, 40, 43, 44, 115).
- Pfifer, H. and P. Seiler (2014a). “Robustness Analysis of Linear Parameter Varying Systems Using Integral Quadratic Constraints”. In: *American Control Conference*. IEEE, pp. 4476–4481 (cit. on pp. 4, 56, 60, 61).
- Pfifer, H. and P. Seiler (2014b). “Robustness Analysis of Linear Parameter Varying Systems Using Integral Quadratic Constraints”. In: *Accepted to the International Journal of Robust and Nonlinear Control*. DOI: [10.1002/rnc.3240](https://doi.org/10.1002/rnc.3240) (cit. on pp. 56, 61, 62).
- Pototzky, A. S., T. A. Zeiler, and B. Perry III (1991). “Calculating Time-Related Gust Loads Using Matched Filter and Random Process Theories”. In: *Journal of Aircraft* 28.5, pp. 346–352 (cit. on p. 24).

- Poussot-Vassal, C. and C. Roos (2012). “Generation of a reduced-order LPV/LFT model from a set of large-scale MIMO LTI flexible aircraft models”. In: *Control Engineering Practice* 20, pp. 919–930 (cit. on pp. 96, 97).
- Robust Control Toolbox: User’s Guide* (2011). MathWorks. Natick, MA: The MathWorks, Inc (cit. on pp. 48, 51, 105).
- Rodden, W. P. and E. H. Johnson (2004). *Aeroelastic Analysis User’s Guide*. MSC.Nastran (cit. on pp. 8, 10–14).
- Roger, K. (1977). “Airplane math modeling methods for active control design”. In: *Structures and Materials Panel* (cit. on p. 14).
- Rotea, M. A. (1993). “The Generalized  $\mathcal{H}_2$  Control Problem”. In: *Automatica* 29.2, pp. 373–385 (cit. on pp. 26, 32, 37, 114).
- Saupe, F. (2013). “Linear Parameter Varying Control Design for Industrial Manipulators”. PhD thesis. Technischen Universität Hamburg-Harburg (cit. on pp. 32, 48, 109).
- Scherer, C. (2001). “LPV control and full block multipliers”. In: *Automatica* 37, pp. 361–375 (cit. on pp. 42, 43).
- Scherer, C. and S. Weiland (2004). *Linear Matrix Inequalities in Control*. Delft Center for Systems and Control; Delft University of Technology (cit. on pp. 27, 115, 116).
- Scherer, C. (1997). “A full block S-procedure with applications”. In: *Conference on Decision and Control*. Vol. 3. IEEE, pp. 2602–2607 (cit. on p. 42).
- Seiler, P. (2015). “Stability Analysis with Dissipation Inequalities and Integral Quadratic Constraints”. In: *IEEE Transactions on Automatic Control* 60.6, pp. 1704–1709 (cit. on pp. 56, 57, 61, 62).
- Skogestad, S. and I. Postlethwaite (1996). *Multivariable Feedback Control: Analysis and Design*. John Wiley & Sons (cit. on pp. 25, 26, 48).
- Sturm, J. F. (1999). “Using SeDuMi 1.02, a MATLAB toolbox for optimization over symmetric cones”. In: *Optimization Methods and Software* 11, pp. 625–653 (cit. on p. 27).
- Summers, E. and A. Packard (2010). “ $\mathcal{L}_2$  Gain Verification for Interconnections of Locally Stable Systems Using Integral Quadratic Constraints”. In: *Conference on Decision and Control*. IEEE (cit. on pp. 4, 65, 67).
- Theis, J. et al. (2015). “Modal Matching for Model Reduction of Aeroservoelastic Vehicles”. In: *Atmospheric Flight Mechanics Conference*. AIAA (cit. on pp. 96, 98).
- Toh, K.-C., M. J. Todd, and R. H. Tütüncü (1999). “SDPT3 – a MATLAB software package for semidefinite programming”. In: *Optimization Methods and Software* 11, pp. 545–581 (cit. on pp. 27, 48).

- Waszak, M. and D. Schmidt (1988). “Flight Dynamics of Aeroelastic Vehicles”. In: *Journal of Aircraft* 25, pp. 563–571 (cit. on p. 10).
- Wood, G., P. Goddard, and K. Glover (1996). “Approximation of Linear Parameter-Varying Systems”. In: *Conference on Decision and Control*. IEEE, pp. 406–411 (cit. on p. 96).
- Wu, F. (1995). “Control of Linear Parameter Varying Systems”. PhD thesis. University of California at Berkeley (cit. on pp. 28, 32, 38, 39, 42).
- Wu, F. (2001). “A generalized LPV system analysis and control synthesis framework”. In: *International Journal of Control* 74.7, pp. 745–759 (cit. on p. 26).
- Wu, F. et al. (1996). “Induced  $\mathcal{L}_2$ -Norm Control for LPV Systems with Bounded Parameter Variation Rates”. In: *International Journal of Robust and Nonlinear Control* 6, pp. 983–998 (cit. on pp. 28, 31, 32, 38, 39).
- Zames, G. and P. Falb (1968). “Stability Conditions for Systems with Monotone and Slope-Restricted Nonlinearities”. In: *SIAM Journal on Control* 6.1, pp. 89–108 (cit. on pp. 60, 65).
- Zeiler, T. A. (1997). “Matched Filter Concept and Maximum Gust Loads”. In: *Journal of Aircraft* 34.1, pp. 101–108 (cit. on p. 24).
- Zhou, K. and J. Doyle (1998). *Essentials of Robust Control*. Prentice-Hall, Inc. (cit. on p. 77).
- Zhou, K. (1993). “Frequency-weighted model reduction with  $\mathcal{L}_\infty$  error bounds”. In: *Systems & Control Letters* 21.2, pp. 115–125. ISSN: 0167-6911 (cit. on p. 105).

# Index

- aerodynamics, 10
- bending, 18
- continuous turbulence, 17
- control surface, 13
- convex function, 116
- convex optimization, 115
- convex set, 115
- cut loads, 10
- delta block, 29
- discrete gust, 17
- downwash, 10
- energy-to-energy gain, 32, 61
- energy-to-peak gain, 32, 63
- equations of motion, 8
- flight envelope, 20
- flight point, 20
- flight speed, 10
- flutter, 7
- Full Block S-Procedure, 42
- gridding approach, 39
- gust input, 13
- gust length, 18
- gust loads, 7, 17
- $\mathcal{H}_2$  norm, 37
- induced  $\mathcal{L}_2 \rightarrow \mathcal{L}_\infty$  norm, 32, 63
- induced  $\mathcal{L}_2 \rightarrow \mathcal{L}_2$  norm, 32, 61
- IQC, 55
- LFR model, 28–30
- LFT, 29
- limit loads, 20
- LMI, 27
- load case, 20
- LPV system, 28
- LTI system, 26
- Lyapunov matrix, 31
  - basis function, 38
- Lyapunov stability, 31
- $\mathcal{L}_2$  norm/space, 25
- $\mathcal{L}_\infty$  norm/space, 26
- maneuver loads, 7
- modal damping, 9
- multiplier
  - Full Block S-Procedure, 43
  - IQC, 56
- nodal loads, 10
- “one-minus-cosine” gust, 17
- parameter vector, 28
- peak loads, 18
- Popov IQC, 59
- Schur complement, 117
- SDP, 27
- sector IQC, 58
- shear, 18
- signal, 25
- signal norm, 25
- standard atmosphere, 12
- structural dynamics, 8
- torsional, 18
- uncertain LPV system, 60
- uncertainty, 28
- weighting filter, 75
- well-posedness, 61
- worst case excitation, 36
- Zames-Falb IQC, 59



# List of Publications

## Journal Papers

- Saupe, F. and A. Knoblach (2015). “Experimental determination of frequency response function estimates for flexible joint industrial manipulators with serial kinematics”. In: *Mechanical Systems and Signal Processing* 52–53, pp. 60–72. DOI: [10.1016/j.ymssp.2014.08.011](https://doi.org/10.1016/j.ymssp.2014.08.011).
- Knoblach, A. (2013a). “Robust Performance Analysis Applied to Gust Loads Computation”. In: *Journal of Aeroelasticity and Structural Dynamics* 3.1, pp. 39–50. DOI: [10.3293/asdj.2013.21](https://doi.org/10.3293/asdj.2013.21).

## Conference Papers

- Knoblach, A., H. Pfifer, and P. Seiler (2015). “Worst Case Analysis of a Saturated Gust Loads Alleviation System”. In: *Guidance, Navigation, and Control Conference*. AIAA. DOI: [10.2514/6.2015-0858](https://doi.org/10.2514/6.2015-0858).
- Leitner, M., A. Knoblach, T. Kier, C. Moreno, A. Kotikalpudi, H. Pfifer, and G. Balas (2015). “Flight Dynamics Modeling of a Body Freedom Flutter Vehicle for Multidisciplinary Analyses”. In: *Modeling and Simulation Technologies Conference*. AIAA. DOI: [10.2514/6.2015-0905](https://doi.org/10.2514/6.2015-0905).
- Pusch, M., A. Knoblach, and T. Kier (2015). “Integrated Optimization of Ailerons for Active Gust Load Alleviation”. In: *International Forum on Aeroelasticity and Structural Dynamics*.
- Theis, J., H. Pfifer, A. Knoblach, F. Saupe, and H. Werner (2015). “Linear Parameter-Varying Feedforward Control: A Missile Autopilot Design”. In: *Guidance, Navigation, and Control Conference*, AIAA. DOI: [10.2514/6.2015-2001](https://doi.org/10.2514/6.2015-2001).
- Knoblach, A. (2013b). “Robust Performance Analysis Applied to Loads Computation of Flexible Aircraft”. In: *International Forum on Aeroelasticity and Structural Dynamics*.
- Knoblach, A., M. Assanimoghaddam, H. Pfifer, and F. Saupe (2013). “Robust Performance Analysis: a Review of Techniques for Dealing with Infinite Dimensional LMIs”. In: *International Conference on Control Applications Part of the Multi-Conference on Systems and Control*. IEEE. DOI: [10.1109/CCA.2013.6662877](https://doi.org/10.1109/CCA.2013.6662877).

- Knoblauch, A. and F. Saupe (2012). “LPV Gray Box Identification of Industrial Robots for Control”. In: *International Conference on Control Applications Part of the Multi-Conference on Systems and Control*. IEEE. DOI: [10.1109/CCA.2012.6402440](https://doi.org/10.1109/CCA.2012.6402440).
- Saupe, F. and A. Knoblauch (2012). “Design of Excitation Signals for the Closed Loop Identification of Industrial Robots”. In: *International Conference on Control Applications Part of the Multi-Conference on Systems and Control*. IEEE. DOI: [10.1109/CCA.2012.6402405](https://doi.org/10.1109/CCA.2012.6402405).

# Curriculum Vitae

Surname	Knoblach
Given names	Andreas Joachim
Date of birth	June 5, 1984
Place of birth	Augsburg Germany

	Employment history
since 08.2010	<b>German Aerospace Center (DLR), Institute for System Dynamics and Control, Oberpfaffenhofen Germany,</b> Research associate.
	10.2013 Research visit, <b>University of Minnesota, Department of Aerospace Engineering &amp; Mechanics, Minneapolis USA.</b>

	Education
10.2004 – 03.2010	<b>Technical University of Munich, Germany,</b> Mechanical engineering (Diplom-Ingenieur Univ.).
04.2007 – 08.2007	<b>South Russia State Technical University, Novocherkassk Russia,</b> Term abroad.
09.1995 – 06.2004	<b>Maria-Theresia-Gymnasium, Augsburg Germany,</b> University entrance qualification (Abitur).

	Internships and secondary employments
08.2009 – 03.2010	<b>German Aerospace Center (DLR), Institute for System Dynamics and Control, Oberpfaffenhofen Germany,</b> Diploma candidate.
02.2008 – 04.2008	<b>KUKA Systems GmbH, Augsburg Germany,</b> Internship.
09.2005 – 05.2007	<b>Technical University of Munich, Institute of Information Technology, Munich Germany,</b> Student employee.